Novel Techniques for Measuring Cardiac Shape and Mechanics with Magnetic Resonance Imaging

by

Wei Zha

A dissertation submitted to the Graduate Faculty of
Auburn University
in partial fulfillment of the
requirements for the Degree of
Doctor of Philosophy

Auburn, Alabama
August 4, 2012

Keywords: magnetic resonance imaging, right ventricular volumetric analysis, left ventricular geometric remodeling, accelerated dynamic imaging

Approved by

Thomas S. Denney, Jr., Chair, Professor of Electrical and Computer Engineering
Stanley J. Reeves, Professor of Electrical and Computer Engineering
Gopikrishna Deshpande, Assistant Professor of Electrical and Computer Engineering

Abstract

Magnetic resonance imaging (MRI) is recognized as a non-invasive cardiac imaging test that provides the most complete, detailed and precise images. The rapid technical development of MRI makes it possible to evaluate cardiac function and morphology reliably in a good spatial and temporal resolution for clinical daily use.

In this dissertation, three aspects of cardiac MRI are investigated: 1) the measurement of right ventricular (RV) functional parameters such as volumes, mass and ejection fraction (EF) from cardiac MRI sequences, 2) a geometric explanation for an observed preservation of left ventricular (LV) EF in the presence of reduced circumferential strain in patients with hypertension, and 3) a novel technique for accelerating the acquisition of cardiac image sequences by exploiting the redundancies in static regions in an image sequence.

While the measurement of LV functional parameters has been extensively studied, the measurement of RV functional parameters has received relatively little attention. A novel protocol for RV volumetric analysis from routine clinical cardiac MRI is proposed and validated.

Hypertension is a disease where arterial pressure is elevated and the heart compensates by increasing LV wall thickness. Previous clinical studies have observed that in hypertensive patients, circumferential strain is reduced while LVEF is normal. We derive a simple, analytical framework to predict LVEF with wall thickness, radius-to-wall thickness ratio, longitudinal shortening quantified from cine MRI and circumferential strain measured by tagged MRI over a wide range of heart conditions. Our work suggests that the preserved LVEF in hypertension despite the presence of reduced circumferential strain is primarily due to the geometric effects of concentric remodeling – relative wall thickness increases without greater LV mass.

The heart takes approximately 10% of the cardiac MR image. Its surrounding tissues are imaged to avoid aliasing. We propose a new imaging method, Noquist with arbitrary dynamic region (NADR), to accelerate the acquisition by reconstructing the pixels in those surrounding tissues once for the entire image sequence. The experimental results demonstrate that NADR is capable of a 56% reduction in *k*-*t* space data with negligible reconstruction error.

Acknowledgments

It is a great pleasure to recall my memories and express my gratitude to all those people that I am indebted to through the last few years.

I could not have hoped for a better advisor than Professor Thomas Denney Jr. He is one of the most considerate, kindest people I met. He has always had the patience to answer all my questions, sometimes too many, no matter how busy he was. He has provided me the tools, the means, the guidance and the freedom for pursuing my research, and impressed me as a dedicated, conscientious researcher. It is his keen intuition, sophisticated research experience, tremendous encouragement and incredible optimism that made me climb up from the bottom of the valleys several times.

It has been a great fortune for being able to work with Professor Stanley Reeves closely. In fact, the crucial component of the accelerated dynamic imaging project is based on Dr. Reeves's own work. It amazes me to see his enthusiasm in teaching, his mathematician soul with a sharp engineer vision, and his remarkable insights about the problems I encountered. Dr. Reeves has always been willing to squeeze time for me in no time whenever needed.

I would always remember Dr. Scotte Hodel for his passion in linear algebra and life. He has been a phenomenal teacher with an engaging teaching style and a warm welcome for students with questions. It was from Dr. Hodel that I learned most of what I know about practical system equation solver.

I thank Dr. Gopi Despande for his invaluable suggestion and profound insights in my research, and for taking time to serve as my committee member.

I thank Dr. Peng Zeng for making his experimental statistics I so abundant in content, and for being the outside reader for my dissertation. Without his enlightenment, I would not gain the ability to understand and perform the statistical analysis for my research.

I thank Dr. Steve Lloyd, Dr. Himanshu Gupta, and Dr. Louis Dell'Italia from University of Alabama at Birmingham for their clinical insights on RV physiology and pathology, RV contouring and volume computation, clinical use of RV volume-time-curves, LV hypertrophy, concentric remodeling, and the ramifications of decreased circumferential strain.

I am in debt to Nouha Salibi whom I became friends with in my last year at Auburn. I was lucky to sit by her on the scan console to observe many spectroscopy scans and bug her with so many elementary questions. It was through those observed scans that I confirmed my enthusiasm about science. She is one of the most sincere people I met. I thank her for her advice on life and career, sharing her wisdoms, and being a hospitable host.

Chun G. Shiros, Wei Feng, Weidong Tang, Tao Ma, Wenting Deng, Bharath Ambale Venkatesh, Nikhil Jha, and Ming Li have been wonderful friends and lab-mates. As friends, I enjoy our talks about life, and share the significant moments. As lab-mates, I cherish the joy from those solid collaborations and the inspiring scientific discussions. In particular, I thank Chun for her invaluable discussions on the statistic issues for hours and hours in those weekends. I thank Nikhil for touring my family around the gorgeous Storybook Farm.

My special thanks go to my family. My lovely toddler girl, Fiona, truly makes me a better, happier person. My dear husband, Feng Wu, has showered me with his love, caring, and support in every possible way. Without his endless encouragement and patience, I would not be who I am now. My beloved parents, Yuanming Zha and Rong Chen, have constantly offered me the fondest, unconditional love and many years of enormous sacrifice to let me go thus far. I dedicate this dissertation to them.

Table of Contents

List of Figures

List of Tables

Chapter 1 Introduction

The American Heart Association's 2006 statistical data estimates that 81,100,000 people in the United States have one or more forms of cardiovascular diseases (CVD). In clinical practice, magnetic resonance imaging (MRI) has progressed towards a fast and reliable technique for assessing ventricular morphology, volumes and function [1-3]. Comparing to other prevalent imaging modalities such as echocardiogram and diagnostic cardiac catheterization, MRI is recognized as a non-invasive cardiac imaging test that provides the most complete, detailed and precise images. The clinical cardiac MRI routines can quantize the volumes and dimensions of the ventricles and measure the functional indices such as volumes and ejection fraction (EF).

The heart, however, is a complex organ, and volumes and EF do not fully characterize the complex and sometimes subtle changes in cardiac shape and function that occur when the heart is diseased. New, practical, and clinically relevant parameters are needed to improve the ability of physicians to diagnose and treat patients with cardiac disease.

In this dissertation, three issues relevant to the development of new cardiac parameters are addressed. First, a previously developed dual contour propagation is validated using a fully segmented RV dataset. A novel protocol for RV volumetric analysis from routine clinical cardiac MRI is proposed [4]. Second, a simply analytic model is proposed to predict LVEF with only a few assumptions. With this model, we provide an explanation for how the altered geometry seen in HTN, with greater wall thickness, leads to preserved EF even in the presence of reduced LV strain [5, 6]. Third, an improved reduced field-of-view

(FOV) technique, Noquist with arbitrary dynamic region (NADR), is proposed for a fast image acquisition with direct two-dimensional (2D) Fourier inversion [7].

The rest of the dissertation is organized as follows. First, background information about cardiac anatomy and physiology, the principles of MRI, and the basics of cardiac MRI are presented in Chapters 2 and 3. The three issues related to the development of new cardiac parameters described above are addressed in chapters 4-6. The summary and ideas for future work are presented in Chapter 7.

Chapter 2 Fundamentals of Human Heart Anatomy and Physiology

The human heart is located at the left-center of the chest, between the lungs and the ribcage. It is a muscular cone-shaped organ about the size of a clenched fist of the same person. As part of the circulatory system, the purpose of the heart is to pump the blood throughout the body. In this chapter, the heart anatomy and physiology are summarized. Two terminologies, heart failure and ventricular remodeling, are discussed briefly.

2.1 Heart Anatomy

The cardiac muscle tissue in between is called myocardium. Primarily composed of the myocardium, the heart is covered by a lubricated sac called pericardium. The base surface of the heart is formed mainly by the left atrium and lies between the lung hila. The anterior surface is shaped by the right atrium and ventricle, while the inferior surface is formed primarily by the left ventricle. The interior surface of the heart valves and chambers is termed endocardium. And the outer layer of the heart wall is called epicardium. The tip of a ventricle is called apex. The heart consists of four chambers: two sets of ventricles and atria as shown in Figure 2.1.

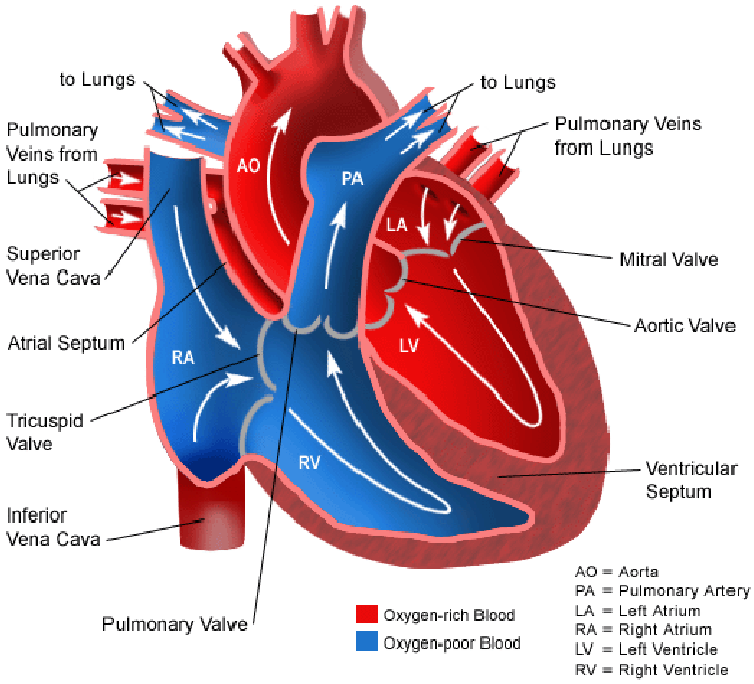

Figure 2.1 Diagram of a normal human heart[1]

The two sets of ventricles and atria are separated by a thick wall called septum. The ventricles are the main pumping chambers. RV is triangular in shape, and its superior portion forms a cone-shaped outflow tract, which leads to the pulmonary artery; whereas LV is approximately cone shaped and longer than that of the RV. The less muscular right and left atrium deliver blood to their respective ventricles [8]. Each set of ventricles and atria is separated by atrioventricular valves to keep the blood flowing in the right direction. The tricuspid valve is located in the floor of the atrium and opens into the RV. The mitral valve guards the opening of the left atrium to the left ventricle. Besides, the aortic valve, normally tricuspid, allows blood to exit LV into aorta. The tricuspid pulmonary valve guides the blood into the lungs via the pulmonary artery when the pressure in RV exceeds the pressure in the pulmonary artery. These two valves are known as semilunar valves.

2.2 Heart Physiology

A complete contraction and relaxation of the heart is a single heartbeat, also called a cardiac cycle [9]. An average adult has a heart rate of about 70 beats per minute. At this rate, a complete cardiac cycle

---

[1] image source: http://www.childrenshospital.org/az/Site509/mainpageS509P0.html

takes roughly .8 s that can be split into three stages sequentially: .1 s in atrial systole, .3 s in ventricular systole, and .4 s in atrial and ventricular diastole[2]. Systole refers to ventricular contraction, and diastole to ventricular relaxation and filling.

In atrial systole, atria contract to push blood into ventricles. Ventricular systole involves simultaneous relaxation of atria and contraction of ventricles. The contraction of ventricular walls ejects blood into the aorta and pulmonary arteries. Deoxygenated blood from the body is pumped through the right atrium and the right ventricle into the lungs, while oxygenated blood out from the lungs is pumped through the left atrium and left ventricle to the body. The closing of atrioventricular valves at the start of this stage produces the first heart sound. In the complete cardiac diastole, atria are already in diastole, ventricles relax, blood from the great veins flows into atria, the pressure in ventricles gradually falls below the atrial pressure so that atrioventricular valves open and blood starts to fill the relaxing ventricles. The rapid closure of semilunar valves at the beginning of this stage produces the second heart sound. The most relaxed and contracted phases of the ventricles are identified end-diastolic (ED) and end-systolic (ES) phases respectively.

2.3 Heart Failure

According to WHO estimates, 16.7 million people around the globe die of cardiovascular diseases each year [10]. Cardiovascular disease is a general term for heart and blood vessel disease. It includes numerous problems and heart failure is one of them. Heart failure remains one of the most common, disabling, and deadly medical conditions encountered by a wide range of physicians and surgeons [11].

Heart failure, sometimes called congestive heart failure, means the heart is not pumping enough oxygen-rich blood out to the rest of the body. The heart muscles either cannot eject the blood out of the heart very well or are too stiff to fill up the blood easily. The condition may affect only one side or even both sides of the heart. Heart failure symptoms often begin slowly and possibly occur when the person is very active. Gradually, breathing problems and other symptoms may be noticed at rest. The common

---

[2] Information source: http://163.16.28.248/bio/activelearner/42/ch42c5.html

causes of heart failure include myocardial infarction (MI), coronary artery disease, hypertension (HTN), heart attack, and valve disease etc. Hypertensive left ventricular disease is the most common condition causing heart failure [12-14].

Hypertension, or high blood pressure, barely has obvious symptoms. About 90% to 95% of cases are categorized as essential hypertension, which refers to high blood pressure with no obvious medical cause. Adults are diagnosed as hypertensive patients if their blood pressure regularly remains at least 140 mmHg systolic or 90 mmHg diastolic [15].

2.4 Left Ventricular Remodeling

In general, the alteration in ventricular architecture from normal, with changes in volume, wall thickness, or shape of the chambers is termed ventricular remodeling. Ventricular remodeling occurs in response to a variety of cardiovascular diseases including increased wall stress [16]. Ventricular remodeling may result in diminished contractile function and reduced stroke volume.

In hypertensive patients, high blood pressure increases the pressure in arterial system. As a result, the heart must work harder to pump against this pressure. The heart remodels by thicker heart muscles. The wall stress increases with LV diameter. Subsequently, the left ventricle dilates and its ejection fraction declines. LV mass can increase from either wall thickening, which is often in response to pressure overload (afterload), or chamber dilation, which is more commonly due to volume overload (preload). When the relative wall thickness is increase, left ventricular hypertension (LVH) is classified as concentric; while LVH is defined as eccentric if there is no increase in the relative wall thickness [17]. When the relative wall thickness increases without greater LV mass, it is termed concentric remodeling. These three patterns of remodeling are depicted against the normal LV geometry in Figure 2.2.

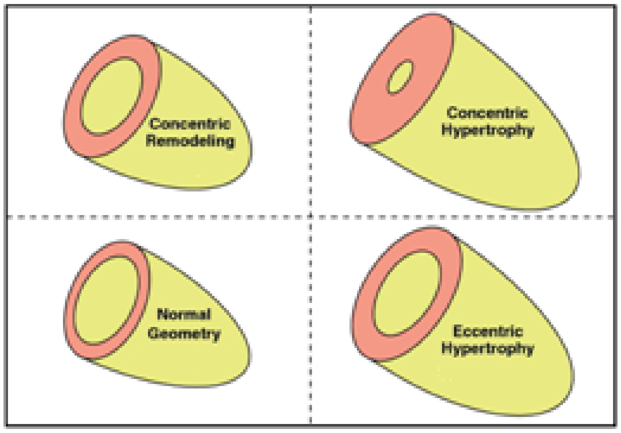

Figure 2.2 Pattern of LV remodeling[3]

2.5 Pulmonary Hypertension

Pulmonary hypertension (PH) is an increase in blood pressure that affects the arteries in the lungs and the right side of your heart. It begins when pulmonary arteries and capillaries become narrowed or blocked. Consequently, the blood is harder to flow through your lungs, and the pressure inside the pulmonary arteries rises so that your right ventricle must work harder to pump the blood through your lungs. As a result, your right ventricle becomes strained and weak. When your heart becomes too weak to pump sufficient blood into your lungs, it leads to heart failure.

Common symptoms are shortness of breath, fatigue, and angina pectoris etc. Because these symptoms become progressively worse, patients may delay seeing a physician for years. Currently, PH has no cure. However, treatments such as medicines and therapies can relieve the symptoms and slow the progress of PH. The earlier PH is treated, the easier it is to control.

In the long-term follow-up in primary PH [18, 19], it is important to assess RV functional indices such a RV volumes, RV ejection fraction, and RV peak ejection and filling rates etc.

---

[3] Image source: Konstam, M.A., et al., *Left Ventricular Remodeling in Heart Failure: Current Concepts in Clinical Significance and Assessment.* JACC: Cardiovascular Imaging. 4(1): p. 98-108.

Chapter 3 Cardiovascular Magnetic Resonance Imaging

Imaging plays a fundamental role in the assessment of cardiac function and pathology. The diagnostic imaging modalities include chest radiography, echocardiography (echo), cardiac catheterization, nuclear imaging, computed tomography (CT), and magnetic resonance imaging. Magnetic resonance imaging utilizes the property of nuclear magnetic resonance to image nuclei of atoms inside the body [20]. It provides good contrast between different soft tissues of the body. In clinical practice, MRI is mainly used to produce high-contrast cross-sectional images through the whole body. Being a highly accurate and reproducible non-invasive technique, MRI is gradually becoming a gold standard for the assessment of regional and global systolic function, myocardial infarction and viability, and congenital heart disease.

3.1 Principles of MRI

Compared to other medical imaging modalities, MRI has more control over the data acquisition and how these data can be manipulated to influence the reconstructed images. The technician can modify parameters affecting the temporal and spatial resolution, the size of field of view (FOV), image contrast, acquisition speed and artifacts.

Magnetic resonance imaging is made possible by the physical phenomenon called nuclear magnetic resonance (NMR). The human body is primarily molecules of fat and water which contain many hydrogen atoms. MRI primarily images the NMR signal from the hydrogen nuclei. Nuclei are comprised of protons and neutrons.

Magnetization

When an external, large static magnetic field of strength B_0 is applied, the spin system becomes magnetized and the spins tend to align with this magnetic field. It precesses around B_0 with the Larmor frequency given by $\omega = \gamma B_0$, where γ is the gyromagnetic ratio.

This process can be modeled using a magnetization vector $M(t)$, which is the sum of a large number of individual nuclear magnetic moments. It can be decomposed into longitudinal magnetization $M_z(t)$ and the transverse component $M_{xy}(t)$, which is oriented in a plane orthogonal to the direction of B_0. The transverse component captures the two orthogonal components $M_x(t)$ and $M_y(t)$ as one complex quantity. At equilibrium, the net magnetization vector lies along the direction of B_0 and $M_z(t)$ equals the equilibrium magnetization M_0.

RF excitation

When a radio frequency (RF) pulse is applied by adding a transverse magnetic field B_1 that is perpendicular to B_0, the rapidly rotating transverse magnetization will be excited. This RF excitation will in turn induce a measurable signal. This signal can be acquired from MR scanner if a RF coil is placed close to the voxel. RF excitation pulse changes the final tip angle α so that such a pulse is referred as an α-pulse.

Relaxation

After applying an α-pulse, transverse relaxation characterized by the time constant T_2 and the longitudinal relaxation with a material property T_1 leads to a decay of the NMR signal. A spin echo is generated by the transverse spins recovering their coherence after loss of coherence followed by a 180-degree RF pulse. The interval from the initial 90-degree RF pulse to the formation of the spin echo is termed as the echo time T_E.

The interval between successive α-pulses is called pulse repetition interval T_R. The tissue contrast can be generated depending on intrinsic tissue properties such as proton density T_2 and T_1 as well as the externally applied excitations.

Spatial Localization

For spatial localization, the gradient coils are designed to produce changes in field strength as a linear function of spatial position. This includes the Larmor frequency to vary as a function of spatial position. This frequency is used for both slice selection and Fourier data readout in the horizontal direction. Here, slice selection, phase encoding, and frequency encoding are assumed to be in z, y, and x direction.

If an oscillating magnetic field is applied at the resonant frequency of a nucleus, then it will become excited. Otherwise, no excitation will occur. If a gradient is applied in the z direction and the resonant frequency is a function of position along z, then only the slice at a particular location that matches the picked resonant frequency will be excited.

The second mechanism to encode spatial information is phase encoding that reads out the vertical direction in Fourier space. When a phase encoding gradient is applied along y direction and then switched off at the beginning of the pulse sequence, the magnetization of the voxels will be dephased. This results in all the protons precessing in the same frequency but different phases. All protons in the same row, perpendicular to the gradient direction, have the same phase. This phase difference lasts until the signal is recorded.

The final step is to apply a frequency encoding gradient G_x. It encodes signals into different frequencies depending on their positions toward the applied gradient. This reads out the horizontal direction in Fourier space. Frequency encoding occurs during signal measurement. The phase encoding step must be finished before the frequency encoding gradient is applied. Therefore, the frequency encoding direction is often referred to the readout direction.

The size of the 2D spatial encoding area which is covered by frequency and phase encodings is defined as the field of view. Sometimes, FOV refers to the three-dimensional spatial encoding area including the slice selection along z direction.

k-space and FOV in Image Space

The data acquired from 2D MRI pulse sequences can be interpreted as scans of Fourier space, also known as *k*-space. The image reconstruction is then the inverse Fourier transform. The *k*-space is defined by the space covered by the phase and frequency encoding data as shown in Figure 3.1. The data acquisition matrix contains raw data. The position in k-space is directly related to the gradient across the object. If the k-space is spanned from $-k_x^{max}$ to $+k_x^{max}$ along x-direction as indicated in Figure 3.1, then the image resolution along x-direction is $1/2k_x^{max}$, while Δk_x equals $1/\mathrm{FOV}_x$.The red dotted arrows in the k-space denotes the Cartesian 2D acquisition direction. The k-space is filled up from bottom left corner to the top right corner by acquiring data from left to right along the frequency encoding direction.

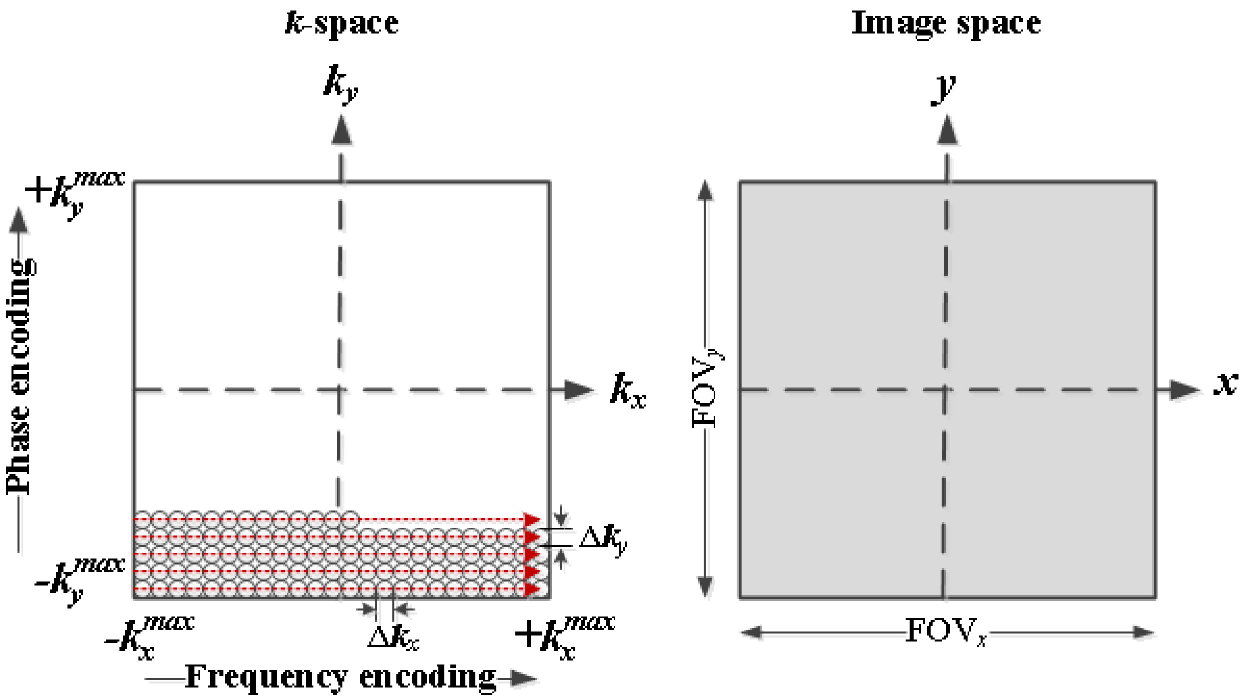

Figure 3.1 k-space and FOV in image space

The FOV, typically measured in mm, determines the dimension of the image. It is directly related to the spacing or density of sampling of data points in k-space Δk_x and Δk_y.

3.2 Cardiac MRI

Cardiovascular magnetic resonance imaging is not an easy task. The constant beating motion and the associated artifacts make the heart difficult to image. The cardiac scan planes can be difficult to prescribe and requires a good understanding of the cardiac anatomy. Cardiac MRI functional measurements are usually based on multiple breath-hold 2D sequences to acquire images covering the entire heart. Although retrospective gating technique does not require breath holding, breath holding during data acquisition can avoid respiratory artifacts. Therefore, breath-hold imaging has been the most widely used approach. This assumes that the patients are able to hold their breath for roughly 20 seconds. The breath holding prolongs the study. It normally takes 30 to 40 minutes for a trained, experienced operator to run the cine protocol on a cooperative subject to measure global cardiac function.

The clinical cardiac MRI is often done in a commercially available 1.5T system using electrocardiogram (ECG) gated steady state free precession (SSFP) technique. Triggered by ECG, standard multi-slice cardiac views are acquired at different phases throughout a cardiac cycle. Typically, three perpendicular imaging planes are prescribed: short-axis (SA), two-chamber (2CH), and four-chamber (4CH) planes. The images of the heart are acquired at different phases throughout a cardiac cycle. The number of phases imaged is usually ranged from 20 to 32.

For the human studies in our database, a complete cine study with approximately 340 images covers the whole heart in four series: 2CH, 4CH, long-axis (LA), and SA series. The imaging planes and resulted prototype images are illustrated in Figure 3.2. Each slice contains 20 timeframes. In the SA series, there are typically 10 to 14 slices covering from the base to the apex of the heart. All other series usually contains one slice. The LA series is often a three-chamber view that exhibits left ventricle, right ventricle and left atrium. The 2CH series, also known as a vertical LA view, views the cross-section of the left ventricle and left atrium. The 4CH series displays the cross-section of all four chambers of the heart, also known as a horizontal long-axis view.

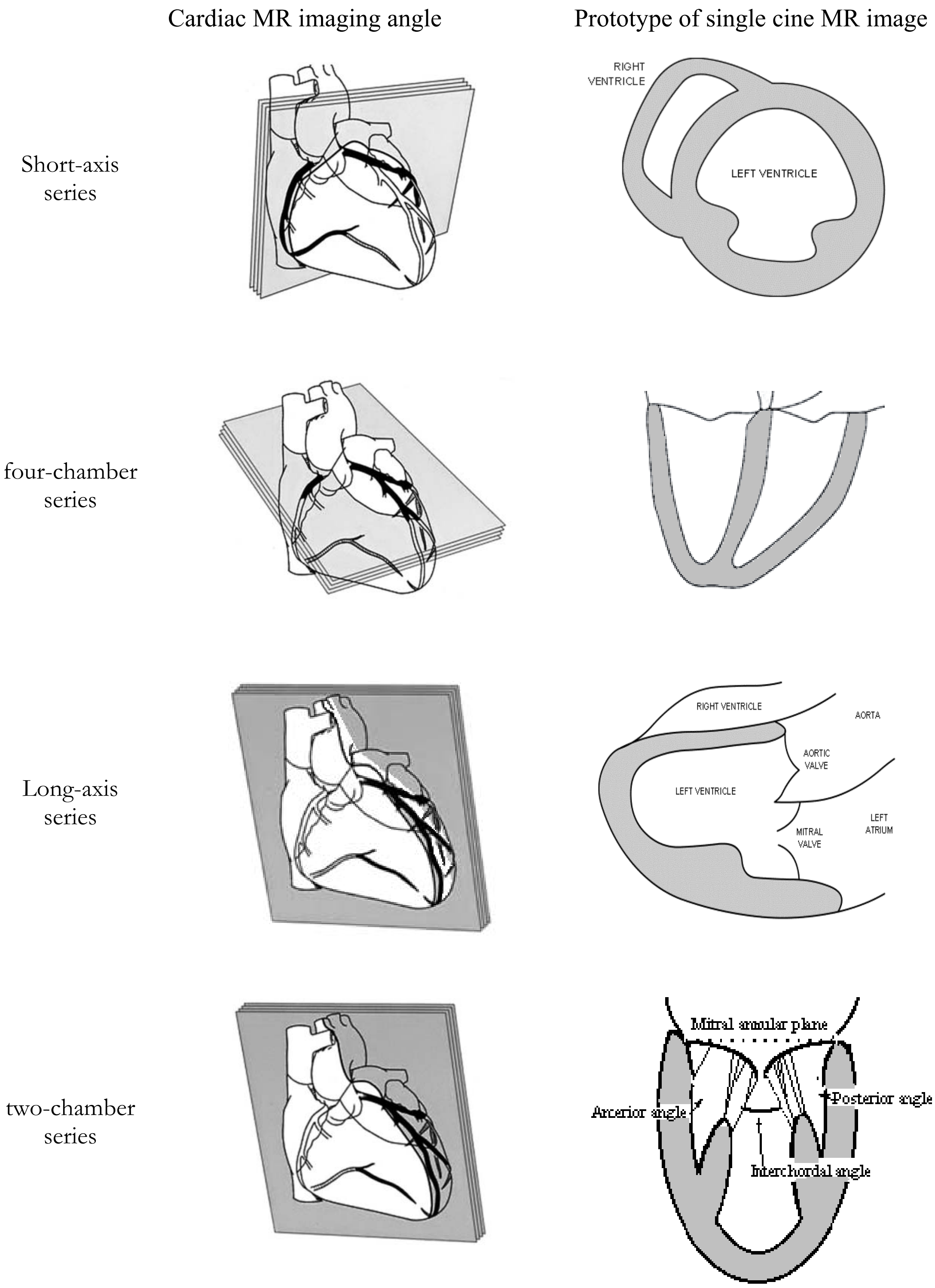

Figure 3.2 Cardiac MR Imaging Angles versus resulted image prototypes[4]

---

[4] Reference: Lott, C.W., *Dynamic Cardiovascular MRI: Principles and Practical Examples.* Australasian Radiology, 2005. 49(4): p. 350-350.

Another commonly used protocol is tagged MRI. Different from cine, tagged MRI has much lower soft-tissue contrast, but it provides contrast with the myocardium. This contrast is utilized for a more accurate evaluation of myocardial deformation. The tagged MRI generates a set of tag patterns within the myocardium as temporary markers at ED by spatial modulation of the magnetization before image acquisition. The resultant periodic tag pattern deforms with the underlying tissue in vivo as the heart contracts and dilates. Tracking of the deformation of the tagged patterns at different phases of a cardiac cycle estimates the detailed myocardial motion. Figure 3.3 illustrates the differences between cine and tagged MR images of SA, 2CH, and 4CH at different phases.

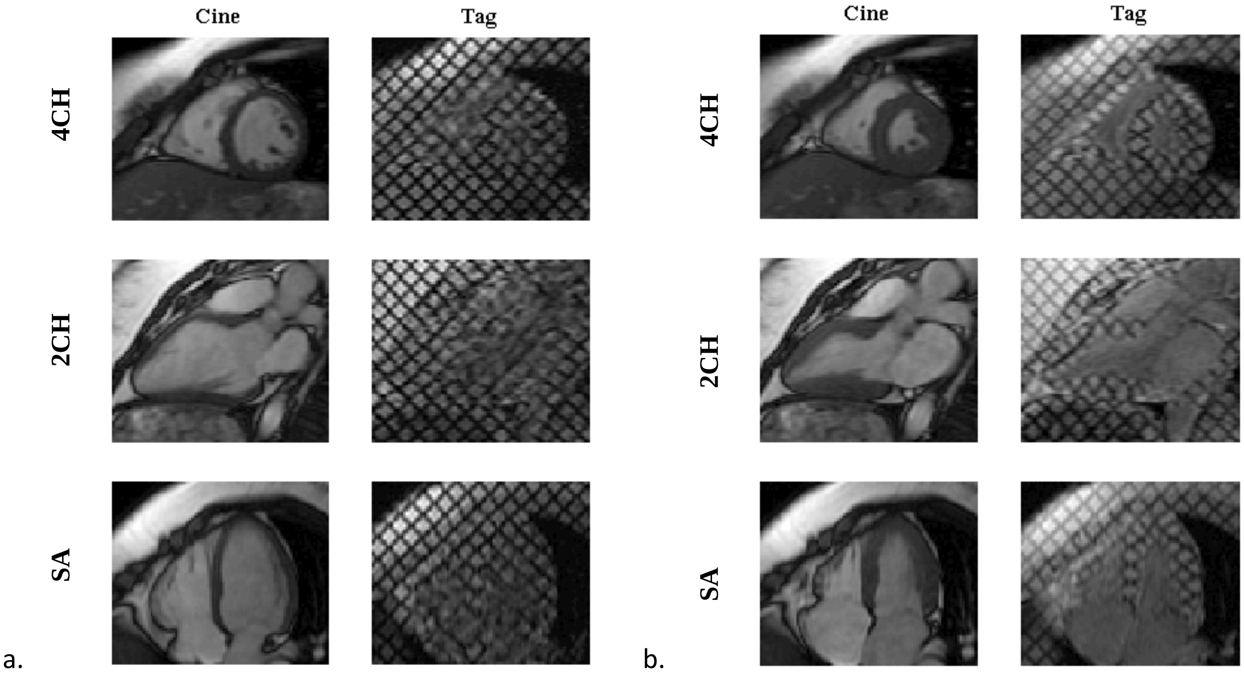

Figure 3.3 Cine and tagged MR images at a. ED and b. ES of a normal volunteer

3.3 Cardiac Functional Parameters

The cardiac function parameters mainly include the radius, thickness and curvature of cardiac chambers, ventricular volumes and mass, myocardial deformation measurements, torsion and twist angle. The majority of these parameters are measured at both ED and ES phases.

Ventricular radius, wall thickness and curvature measurements can reflect the degree of ventricular hypertrophy. Higher LV curvature implies eccentric hypertrophy such that the normal conical shape is enlarged in the circumferential direction towards a basketball. These measurements can be extended into the parameters that reflect how well the heart works. The wall thickening is the difference of wall thickness between ED and ES divided by the wall thickness at ED. Similarly, fractional shortening (FS) is the radius difference between ED and ES divided by the radius at ED. The radius-to-wall thickness (RT) ratio has a constant relation with LV systolic pressure. Greatly increased RT ratio values, suggesting inadequate hypertrophy, indicate a poor prognosis in patients with chronic aortic regurgitation and in those with congestive cardiomyopathy [21].

Ventricular volumes and mass are the essential measurements of the heart. The difference of the LV volume is called LV stroke volume. The ejection fraction is the ratio of stroke volume and volume at ED. For a normal volunteer, LV EF is about 60%, which means 60 percent of blood volume at end diastole is pumped out of LV. This is a cardiac function indicator that is always reported in cardiac echo too. With MRI, the peak ejection and filling rate can also be calculated by measuring ventricular volumes at all the phases.

The myocardial deformation measurements lead to the computation of myocardial strain and strain rate. Strain is the relative deformation of tissue from an applied force, whereas strain rate is the rate of this deformation. For instance, the circumferential strain is a measurement for contraction of myocardium in the circumferential strain. A positive strain value implies expansion or lengthening and a negative value indicates compression or shortening. The circumferential and longitudinal strains are negative. Strain and strain rates represent myocardial contractile ability [22].

Chapter 4 Experimental Validation of RV Contour Propagation

Cardiovascular magnetic resonance (CMR) is the gold standard for measurements of ventricular volumes and function [3, 18, 23, 24]. Many techniques have been developed for automated segmentation of the left ventricle [25-28], but the RV has received less attention. Compared to ejection fraction alone, RV volume-time curve (VTC) derived ejection rates along with RVEF better characterize systolic function. Moreover, RV VTC-derived filling rates provide important information about RV diastolic function, which is not routinely obtained during routine RV clinical analysis based on end-diastole (ED) and end-systole (ES) frames. In patients with paradoxical septal motion and/or RV dyssynchrony, the timeframe with minimum or maximum endocardial contour area can be different in different slices, which can result in variability in the choice of ED or ES timeframes [29]. In these patients, RVEF and RV stroke volume (RVSV) calculations may be more accurate when computed from a RV VTC.

In Feng, et al [30], a dual-contour propagation technique was introduced for computing LV VTCs based on automatic propagation of LV contours drawn at ED and ES. This technique made no geometric assumptions on the shape of the myocardial contours and leveraged the contours that are routinely drawn at ED and ES for computation of LV volumes and LV EF.

In this chapter, a novel RV volumetric analysis protocol was proposed and validated. The dual-propagation method was used to propagate the manual-drawn contours at ED and ES to all other timeframes in a cardiac cycle. A partial volume summation technique based on automated tracking of the tricuspid annulus (TA) was used to determine the percentage of volume from basal slices to include in the RV volume computation in each time frame.

4.1 Overview of RV Myocardial Segmentation

Although segmentation is one of the most difficult tasks in image processing, it is the foundation of the success of image analysis. The goodness of a segmentation method is assessed based on three factors: precision, accuracy, and efficiency [31]. Precision refers to the repeatability of the method. According to this criterion, there is no completely satisfactory segmentation technique yet, although numerous researchers have given attention to this area and made remarkable improvements in many specific image segmentation problems.

Medical image segmentation has been a prevalent research issue over the last three decades. These methods are classified into five categories: deformable models, statistical approaches, graph-based methods, hybrid techniques, and other approaches. Computer-based deformable modeling techniques such as gradient vector flow (GVF) [32, 33], initialization via Poisson inverse gradient (PIG) [34], and Finsler active contour [35]etc., have gained great attention since their debut. Statistical approaches such as active appearance models (AAMs) [36] and Minimal shape and intensity cost path (MSICP) [37] etc., have gained a reputation for their success in face recognition, alignment and tracking. Graph based algorithms such as graph cuts [38, 39], random walks [40], and fuzzy connectedness [41] etc., have emerged as an increasingly useful tool for problems in vision for its geometric representation and pixelwise classification ability. The general purpose of hybrid techniques such as live-wire-on-the-fly [42] and stochastic active contour scheme (STACS) [43] is to merge the advantages of separate techniques while avoiding or at least lessening the shortcomings of using those techniques alone. Some other approaches such as Bayesian network [44, 45] and motion cues [46, 47] may assist the real-time applications in future.

The segmentation of RV is complicated by two main factors. First, the RV is a thin-walled structure with complex shape compared to the more symmetric, thick-walled LV. Therefore automated segmentation algorithms, most of which were originally developed for the LV [25, 28, 48], often perform poorly on the RV. Second, the relatively large cross-sectional area of the RV base and the greater excursion of the TA during systole, make RV volumes highly sensitive to the choice of basal slices [49]. In basal slices of standard short-axis views, the coexistence of pulmonary artery, aorta, and right atrium (Figure 4.1) makes the manual delineation of RV contours a challenging task, not to mention the automatic segmentation.

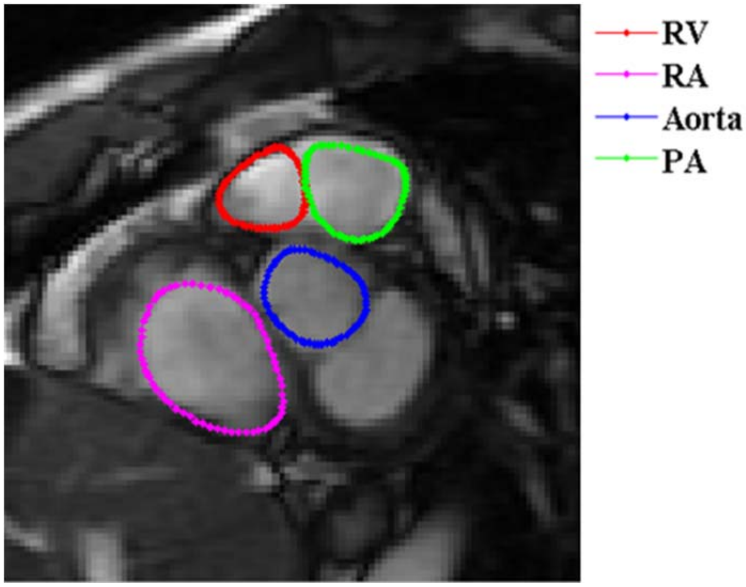

Figure 4.1 Illustration of RV in a basal slice of a short-axis view
(In the basal slices of standard short-axis views, RV (red) is adjacent to the right atrium (RA) in magenta, aorta in blue and pulmonary artery (PA) in green.)

The task of myocardium segmentation is currently handled in most clinical settings by having an operator sit at a computer console and interactively annotate myocardium boundaries slice by slice. It is not only time-consuming, tedious, and subjective; it is also irreproducible due to the variation from person to person or even from time to time. Despite the fact that there are several automated or semi-automated cardiac segmentation software packages in the market, to develop a practical, intelligent, and reliable fully automated segmentation technique is still an open issue.

4.2 Contour Propagation Method

The measurements of the ventricular volume over time in a cardiac cycle allow a sensitive assessment of cardiac systolic and diastolic function. However, manual annotation of the myocardium per timeframe per slice is laborious, time-consuming and error-prone.

Segmentation of the myocardium at only ED and ES alleviates the burden of the whole heart segmentation. Intuitively, it yields better accuracy. Contour propagation is a fairly new supplement for the independent per frame segmentation techniques summarized earlier. It utilizes the segmented contours at a certain phase as the template and then propagates them intelligently to other phases. This segmentation through propagation method has been used in commercially available software packages such as MASS by Medis medical quantification software and CAAS MRV for Windows Version 3.3.1 (Pie Medical Imaging, Maastricht, The Netherlands).

A semi-automated dual contour propagation method was proposed in [30] to measure temporal changes in LV volume over a cardiac cycle. It leverages the user interaction in drawing LV ED and ES contours by automatically propagating them to all other timeframes of a cardiac scan via the non-rigid registration method.

In this section, the ideas of non-rigid registration and dual contour propagation are reviewed.

4.2.1 Non-rigid Registration

The traditional non-rigid image registration (NRR) [50] is formulated in a single direction from the template image to the source image. The sum of squared differences is treated as the cost function or similarity measure. A multi-resolution approach is used to improve convergence speed and avoid local minimal.

A NRR based contour propagation method [51] is proposed for myocardial delineation. The template is the first phase, often the end diastole, of the cardiac cycle. First of all, the template is manually contoured and re-sampled in the polar coordinates with the origin being the center of initially contoured LV blood pool. In the same manner, the initial contours and the source image are re-sampled. Then, NRR is performed on the re-sampled images, and deformation is acquired in the polar coordinates. With this deformation, the initial contours are mapped to the source image and converted to Cartesian coordinates. This procedure is repeated for all the source images that need propagation. The template could always be the initial annotated contours, which is known as all-to-one approach. Or, the template could be the latest propagated contours along the way. For instance, ED is the original template and is propagated to (ED+1) phase towards end systole. Then the (ED+1) phase becomes the template for (ED+2) phase and so on.

4.2.2 Dual Contour Propagation

In all scans, LV endocardial contours at ED and ES are manually drawn on consecutive short axis slices between the mitral annulus (MA) and LV apex. Similarly, RV endocardial contours are manually drawn as closed contours between the tricuspid annulus and RV apex [48, 52].

The contour propagation procedure propagated contours in all slices that are contoured at ED, and, near the RV base, the RV atrio-ventricular margin may have moved through the image plane during the cycle. An exponential of 2 is used for the downsampling ratio of both the images and the deformations for each multi-resolution layer. The propagation scheme is depicted in Figure 4.2. First, the above mentioned NRR algorithm is used to propagate ED contours forward through end systole and backward through the 20th timeframe to the (ES+1) frame, which immediately follow the timeframe of ES. Second, ES contours are propagated forward through the 20th frame and backward towards ED. These two sets of propagated contours are then combined via a weighted least-square fit into a single B-spline contour. The ED-propagated contour weight for a given time is computed using cubic-spline interpolation from the empirically-determined control points [53]. The ES-propagated contour weight is one minus the ED-propagated contour weight. In such a manner, if the distance of a frame to ED increases, its ED-propagated weight decreases.

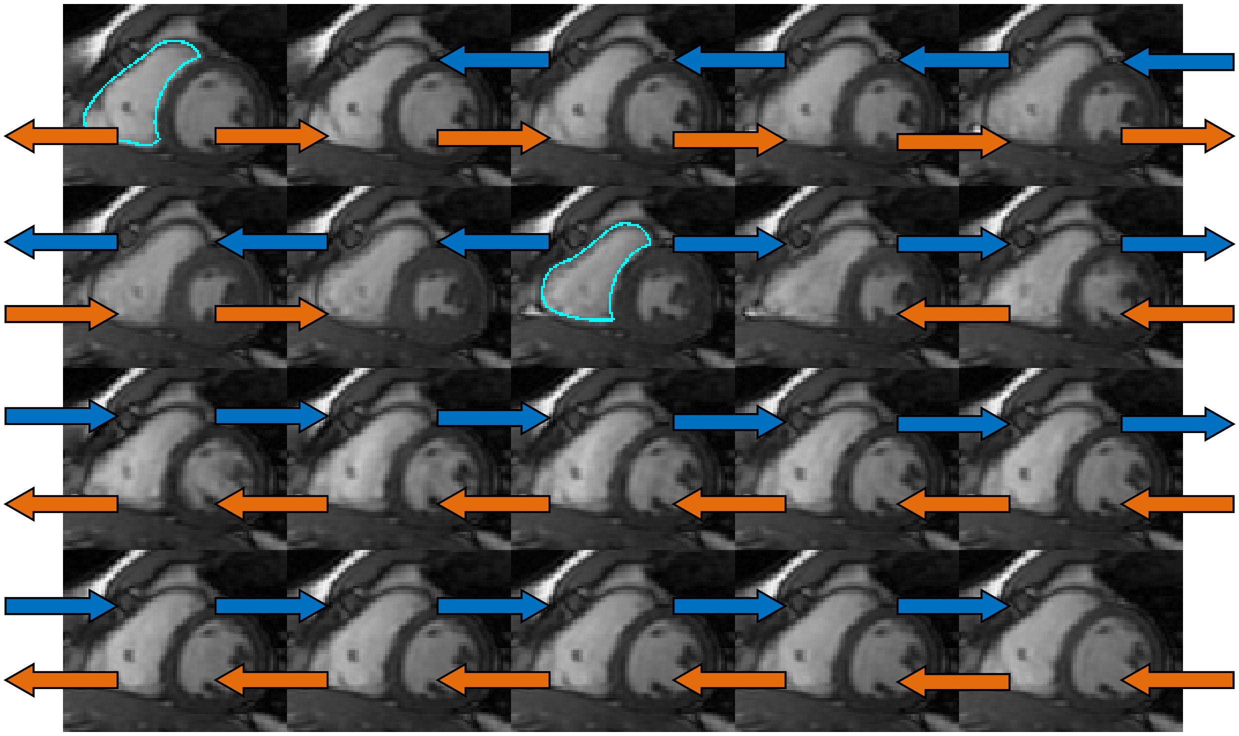

Figure 4.2 Dual contour propagation diagram
(Orange arrows denote propagation using ED contour templates; navy arrows denote propagation using ES contour templates)

4.3 Methodology

In this validation, nine normal volunteers underwent cardiovascular magnetic resonance imaging. RV contours were manually drawn on all timeframes. The geometry-independent dual-contour propagation technique, which makes use of contours drawn at ED and ES, was used to compute RV VTC and measure RV ejection and filling rates. A partial volume summation technique based on tricuspid annulus displacement was used to determine the percentage of volume from basal slices to include in the volume computation. The resulting RV VTCs were compared to those obtained from manually-drawn contours, and existing propagation techniques. Volumes, RVEF, and ejection and filling rates computed using dual-contour propagation were compared to those computed from manually drawn contours.

4.3.1 Cine CMR

In this study, a total of nine normal volunteers (mean age, 38±9 years; range, 26-53 years; 3 female) with no history of cardiovascular disease underwent cine CMR assessment in 2005.The study protocol was approved by the Institutional Review Board at both the University of Alabama at Birmingham and Auburn University and all participants gave written informed content.

Cine CMR was performed on a 1.5-Tesla scanner (CV/i, GE Healthcare, Milwaukee, WI) optimized for cardiac application. ECG-gated, breath-hold steady-state free precession (SSFP) sequence was used to obtain standard (2, 3, and 4 Chamber, Short Axis) views with the following parameters: slice thickness 8 mm with no gap between short-axis slices, flip angle 45 deg, typical TR/TE = 3.8/1.6 ms, field-of-view 44 x 44 cm, 10 views per segment, scan matrix 256 x 128; typical acquired temporal resolution approximately 40 ms; data reconstructed to 20 cardiac phases.

4.3.2 Image Analysis and Contour Propagation

In all scans, LV endocardial contours at ED and ES were manually drawn on consecutive short axis slices between MA and LV apex. Similarly, RV endocardial contours were manually drawn as closed contours between the TA and RV apex [49, 52]. The papillary muscles and trabeculae were included in the LV and RV endocaridal contours. The endocardial borders were traced by viewing images from different slice prescriptions simultaneously and playing all short-axis images of a slice in a movie mode. These manual contours are treated as gold standards for performance evaluation and validation of the dual-contour propagation. Typical manually-drawn RV endocardial contours for all slices at ED of a short-axis scan are shown in Figure 4.3.

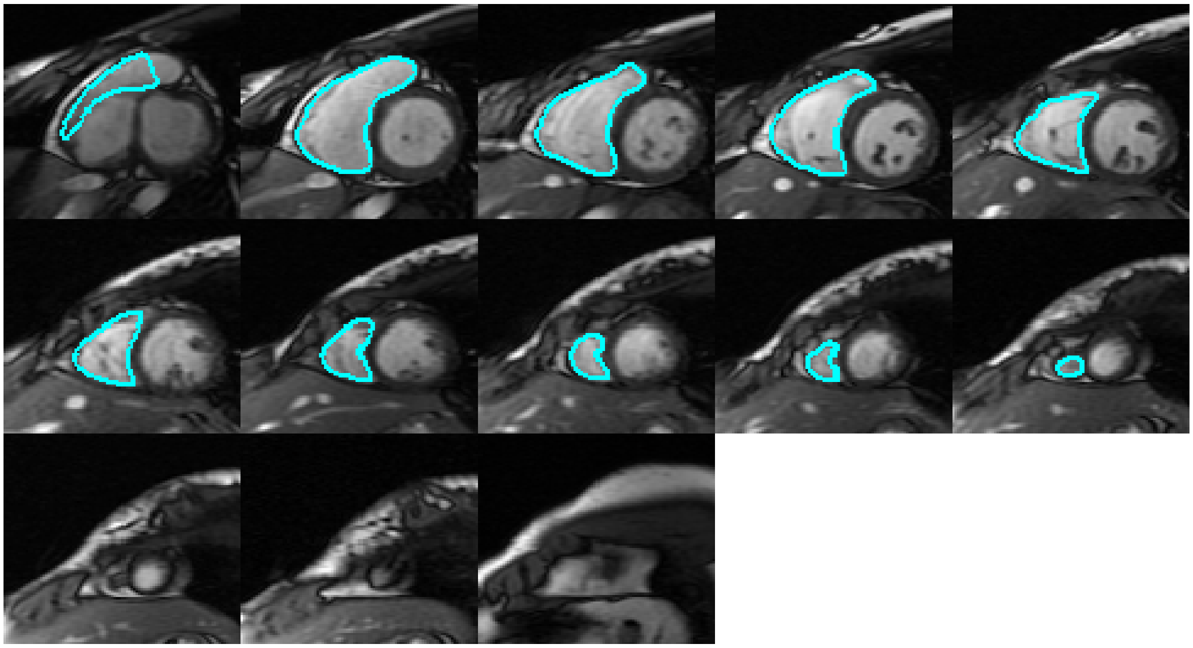

Figure 4.3 Manually contoured RV endo of all the slices at ED in a short-axis view
(RV endocardial contours were shown in cyan; slice orientation: basal to mid ventricular and then apical slices were arranged from left to right and from the top to the bottom row)

The contours described above were then automatically propagated to all the other frames in the acquisition using the dual-contour propagation algorithm described in Section 4.2.2.

4.3.3 RV Volumetric Analysis

After propagation, volume at each timeframe was computed by summing the volumes defined by the RV endo contour in each slice. Typically, rules based on the percentage of TA within the basal slice are used to either totally include or totally exclude a slice from the volume summation [18, 49].

The contour propagation procedure, however, propagated contours in all slices that were contoured at ED, and, near the RV base, the RV atrio-ventricular margin may have moved through the image plane during the cycle. Consequently, a partial volume summation technique based on automated tracking of the TA was used to determine the percentage of volume from basal slices to include in the RV volume computation in each time frame. A user-selected point was marked at TA on the RV lateral wall in both ED and ES frames of a four-chamber slice, and then the NRR algorithm was used to track this point through the cardiac cycle. The displacement of this point perpendicular to the short-axis image plane was used to determine the range of short-axis slices that should be used in the volume computation. For instance, if the tricuspid annulus displaced 12 mm between ED and the current time frame and the slice thickness was 8 mm, the most basal slice would not be used in the volume computation and half of the volume from the second-most-basal slice would be counted in the total volume at the time frame. Unless specified otherwise, this TA tracking procedure was used to compute volumes for all the contouring techniques presented in this paper, including manual contouring and automatic contour propagation algorithms.

Once the volumes were computed in each time frame, a RV VTC curve was constructed and differentiated with respect to time. ED was defined as the RV maximum-volume time frame, and ES was defined as the RV minimum-volume time frame. RV ED and ES are not necessarily the same as LV ED and ES. Early diastole and late diastole were defined as the first and second halves respectively of the diastolic interval. RVPER was defined as the maximum negative time derivative during the systolic interval. RVePFR and RVaPFR were defined as the maximum derivative during the early and late diastole.

The volumes computed from the dual-propagation, one-way propagation from ED (EDNRR) or ES (ESNRR) separately using the NRR, and propagation from ED or ES in the commericially available software, CAAS MRV for Windows Version 3.3.1 (PIE Medical Imaging, Maastricht, The Netherlands) were compared to volumes computed from manually-drawn contours on each of the nine normal human imaging studies. To compare VTCs computed from different types of contours, differences were computed at each time point by subtracting the manual volume from the propagated volumes.

4.3.4 Validation Analysis

The validation contains three aspects: comparing the volumes resulting from different propagation methods, comparing the RV volumes and ejection and filling rates between two basal slice selection methods, and evaluating inter-user variablity.

4.3.4.1 Comparison between Contour Propagation methods

Volumes computed from dual-contour propagation, single-propagated contours from ED and ES using NRR, and single-propagated contours from ED and ES using CAAS MRV by Pie Medical Imaging are compared to volumes computed from manually-drawn contours on each of the nine normul human imaging studies. RV VTCs are computed for EDNRR, ESNRR, dual-propagated, CAAS MRV ED and CAAS MRV ES contours respectively for each study. To compare VTCs computed from different types of contours, differences are computed at each time point by subtracting the manual volume from the propagated volumes.

4.3.4.2 Comparison of RV basal slice selection methods

The decision of which basal slices to include in the volume computation at each time frame can have a significant effect on the volume at that time frame - particularly in the RV, where the cross-sectional area is relatively large. To assess differences in basal slice selection, RV VTCs computed from manually-drawn contours using the TA-tracking method described above are compared with volumes computed using slices selected by a Level 3 trained cardiac CMR specialist in each time frame. RVESV, RVEF, RVPER, RVePFR, and RVaPFR are computed from each pair of VTCs and compared. RVEDV is not compared since the TA-tracking method uses ED as a reference, which makes RVEDV the same in both methods.

4.3.4.3 Inter-user variability

To assess inter-user variability in volumes computed from propagated contours, two sets of RV endocardial contours are manually drawn in each study at ED and ES by different users. Each user is a Level 3 trained CMR specialist or equivalent. Each set of ED and ES contours is propagated using the dual contour technique, and VTCs and RV ejection/filling rates are computed.

4.3.5 Statistical Analysis

Comparisons of RV volumes computed from different propagation schemes were performed using mixed modeling via PROC MIXED (SAS version 9.2). To account for the repeated measures within a subject, a compound symmetry correlation structure was assumed. In the RV volume study, confidence intervals on the differences based on the fitted mixed model were constructed each at 99% level to achieve a joint confidence level of at least 95% for this set of confidence intervals using Bonferroni adjustment [54].

Comparisons of RVESV, RVSV, RVEF, RVPER, RVePFR and RVaPFR values computed from dual-propagated and manually-drawn contours, comparisons of contours propagated by two different users, comparisons of RV peak ejection and filling rates on VTCs computed from various slice ranges of dual-propagated contours, comparisons of volumes computed using TA tracking and manual slice selection, and comparisons of RV and LV stroke volumes were performed using two-tailed paired t-tests, correlation analysis, and Bland-Altman analysis. In all these statistical tests, a p-value less than 5% was considered statistically significant.

4.4 Validation Results

The validation results are organized in five aspects as follows. First, RV VTCs from different methods were compared via statistical analysis. Second, the RV volumetric measurements and ejection and filling rates resulted from two basal slice selection methods were compared. Third, the LV and RV stroke volumes were compared between different contouring and slice selection methods. Fouth, the RV ejection and filling rates between manual contouring and dual propagation were compared. Fifth, the inter-user variability were evaluated by comparing the RV volumetric measurements and the ejection and filling rates.

4.4.1 Comparison of RV Volume Time Curves

One RV VTCs from a normal volunteer are shown in Figure 4.4. The NRR propagated volumes from ED (green) contour templates overestimates the volumes by manually-drawn (red) contours. CAAS MRV ED (black) overestimates the volumnes in early diastole and underestimates in systole and late diastole. On the contrary, the NRR propagated volumes from ES (cyan) contours and CAAS MRV ES (magenta) severely underestimates the volumes by manual contouring. The dual-contour propagation technique yields volumes close to the manually-contoured volumes.

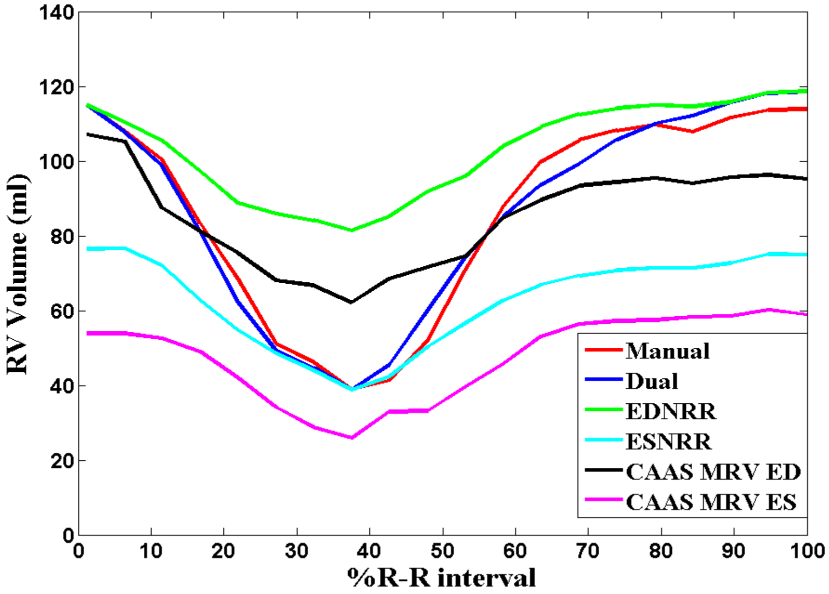

Figure 4.4 RV volume-time curves for a normal human volunteer
(End systole is the 8th timeframe located around 38% R-R interval. Dual: dual propagation method; Manual: manual contouring; EDNRR: one-way propagation using ED contours; ESNRR: one-way propagation using ES contours; CAAS MRV ED: embedded propagation method using ED contours in CAAS MRV 3.2; CAAS MRV ES: embedded propagation method using ES contours in CAAS MRV)

The confidence intervals and p-values of the RV volume differences among dual-propagation, EDNRR, ESNRR, CAAS ED and CAAS ES are listed in Table 4.1. The volume difference between each propagation method and the manual contouring are computed for the statistic testing. No significant differences were found from the dual-propagation. In comparison, NRR from ED overestimates RV volumes; NRR from ES underestimates RV volumes; CAAS MRV ED and CAAS MRV ES underestimates RV volumes.

Table 4.1 RV Volume Difference

	RV Volume Difference (RVEDV)			
	Mean ± SE	99% Confidence Interval		P
Dual - Manual	-.0085 ± .010	-.037	.020	.42
EDNRR - Manual	.071 ± .010	.044	.11	<.0001
ESNRR - Manual	-.14 ± .010	-.24	-.17	<.0001
CAAS MRV ED - Manual	-.079 ± .010	-.11	-.051	<.0001
CAAS MRV ES - Manual	-.37 ± .010	-.39	-.34	<.0001

Dual: dual propagation method; Manual: manual contouring; EDNRR: one-way propagation using ED contours; ESNRR: one-way propagation using ES contours; CAAS MRV ED: embedded propagation method using ED contours in CAAS MRV 3.2; CAAS MRV ES: embedded propagation method using ES contours in CAAS MRV 3.2.

The VTCs in 9 normal human volunteers computed from the dual-propagated and manually annotated RV contours with TA tracking are depicted in Figure 4.5. Dual propagated VTCs show good agreement with the manual VTCs, suggesting that contours manually drawn at ED and ES are consistently propagated to the other time frames in the cine sequence.

The average computation time for the dual-contour propagation alone (excluding the time for the manual contouring at ED and ES) is 4.3 minutes for a single study on a 2.61 GHz quad-core computer with 8 GB of RAM whereas manual contouring of all timeframes all applicable slices requires approximately 4 hours per study.

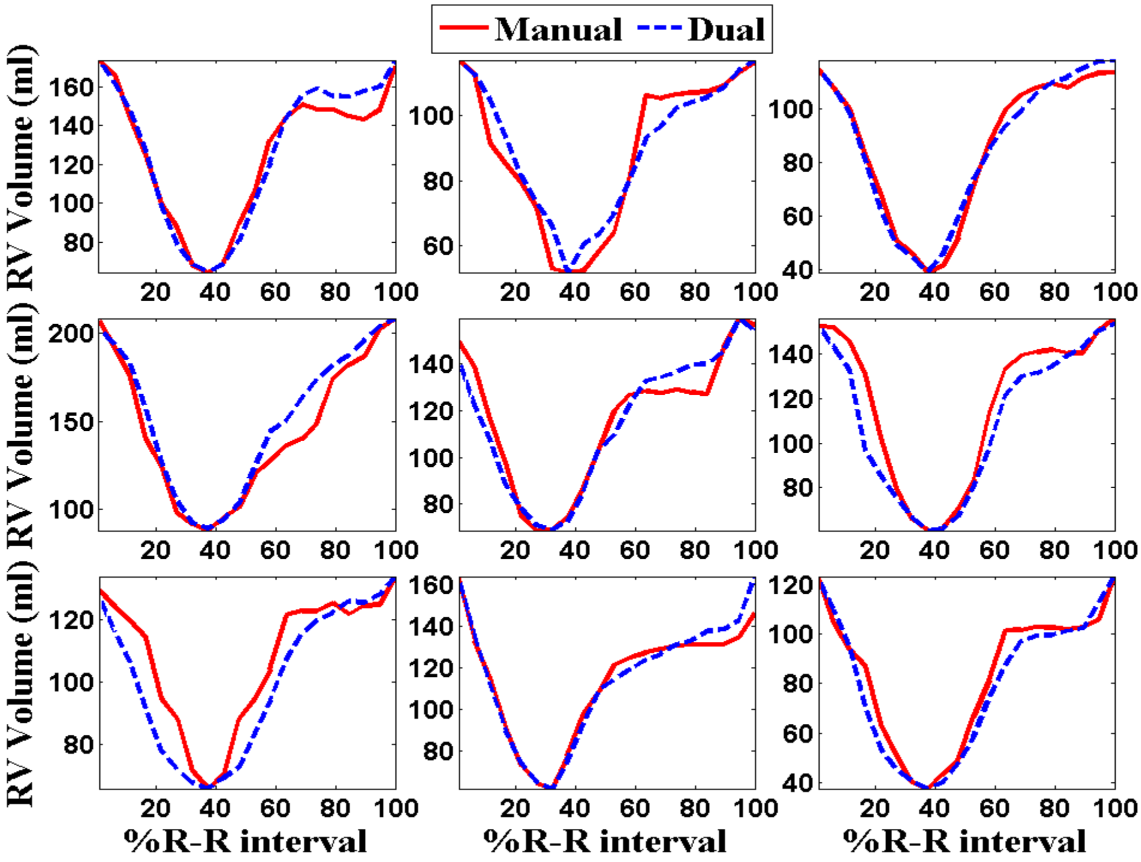

Figure 4.5 RV volume-time curves for nine normal human volunteers

4.4.2 Comparison of RV Basal Slice Selection Methods

TA-tracking measures a lower RVESV and a higher RVEF than manually-selected basal slices as shown in Table 4.2. The differences are calculated as TA tracking minus manual.

Table 4.2 Comparison of parameters computed using TA tracking and manual slice selection

	Difference (Mean ± SE)	P (Difference)	ρ	P(ρ)
RVESV (ml)	-4.10 ± 1.66	0.039	0.95	<.0001
RVEF (%)	2.65± 1.06	0.037	0.83	.0053
RVPER (RVEDV/sec)	0.12 ± 0.08	0.17	0.89	0.0013
RVePFR (RVEDV/sec)	0.06 ± 0.07	0.44	0.97	<.0001
RVaPFR (RVEDV/sec)	0.14 ± 0.06	0.058	0.96	<.0001

No significant differences are found between the two techniques in RVPER, RVePFR, and RVaPFR. TA-tracking and manual basal slice selection show strong correlation in RVESV, RVEF, and RV peak ejection and filling rates.

4.4.3 Comparison of LV and RV Stroke Volumes

In this study, LVSV is used as a reference standard to validate measurements of RVSV. In normal volunteers, LVSV and RVSV should be similar. Figure 4.6 shows box plots of SV differences from VTC computed from manual contours and manual slice selection, manual contours with TA/MA tracking, and dual-propagated contours with TA/MA tracking. Manual contouring and slice selection result in a significant difference between RV and LV stroke volumes (6.62±2.85, P=.049). No significant differences are found between RVSV and LVSV if TA/MA tracking was used (manual contours: - 3.88±2.98, P=.23; dual-propagation: - 2.47±3.51, P=.50).

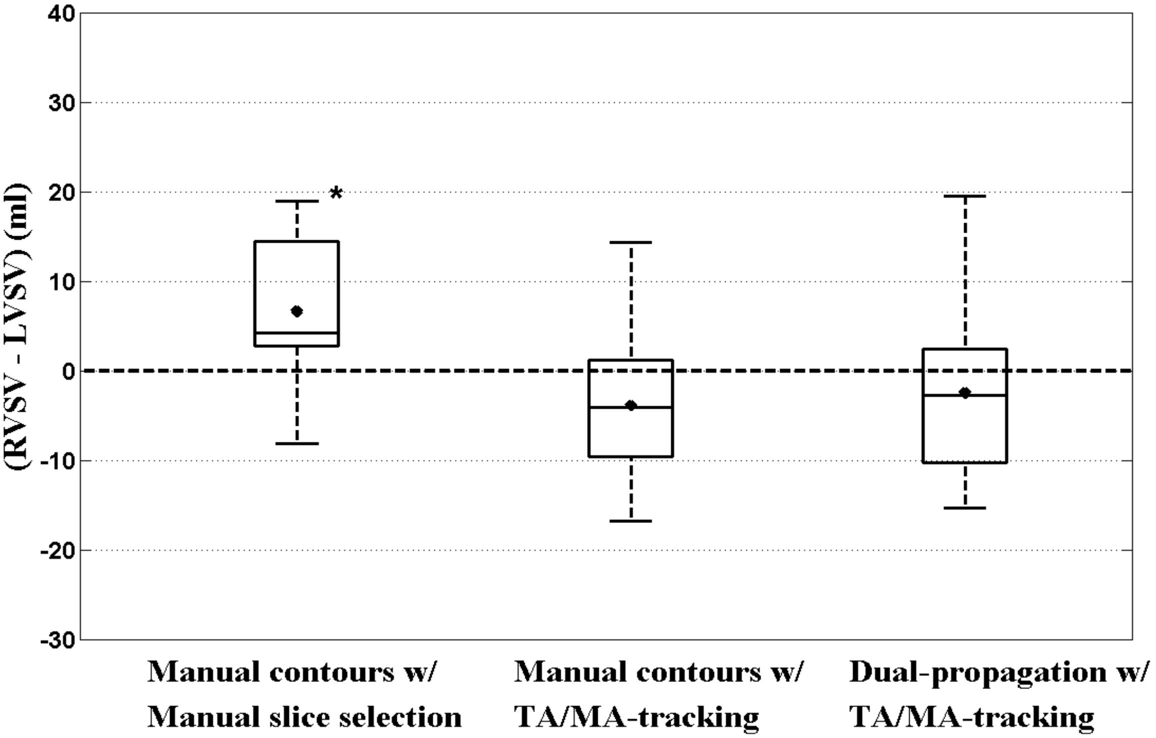

Figure 4.6 Comparison on RV-LV stroke volume differences
(The dot indicates the mean stroke volume difference. The line in the box indicates the median stroke volume difference. * indicates significant difference from zero with P<.05)

4.4.4 Comparison of RV Peak Ejection and Filling Rates

The peak ejection and filling rates are computed from both manual and dual-propagated contours. Table 4.3 illustrates the comparison of the rate differences between these two. No statistical significances are found in RVPER, RVePFR and RVaPFR. However, only RVPER shows a strong correlation between the two methods (ρ=0.86, P=0.0027). The scatter and Bland-Altman plots in Figure 4.7 show that at higher filling rates, manual contouring tends to measure larger RVePFR and RVaPFR values than dual-contour propagation.

Table 4.3 Differences in RV rates computed from dual-propagated and manually-drawn contours

	Rate Difference (RVEDV/sec)					
	Mean ± SE	P (Difference)	95% Confidence Interval		ρ	P(ρ)
RVPER	.06± .10	.56	-.28	.17	.86	.0027
RVePFR	-.36 ± .22	.14	-.15	.88	.61	.082
RVaPFR	-.23 ± .16	.19	-.15	.61	.41	.13

data: Mean ± Standard Error; ρ: correlation coefficient;
Differences are dual-propagated - manual.
RVPER: RV peak ejection rate; RVePFR: RV early diastolic filling rate; RVaPFR: RV late diastolic filling rate.

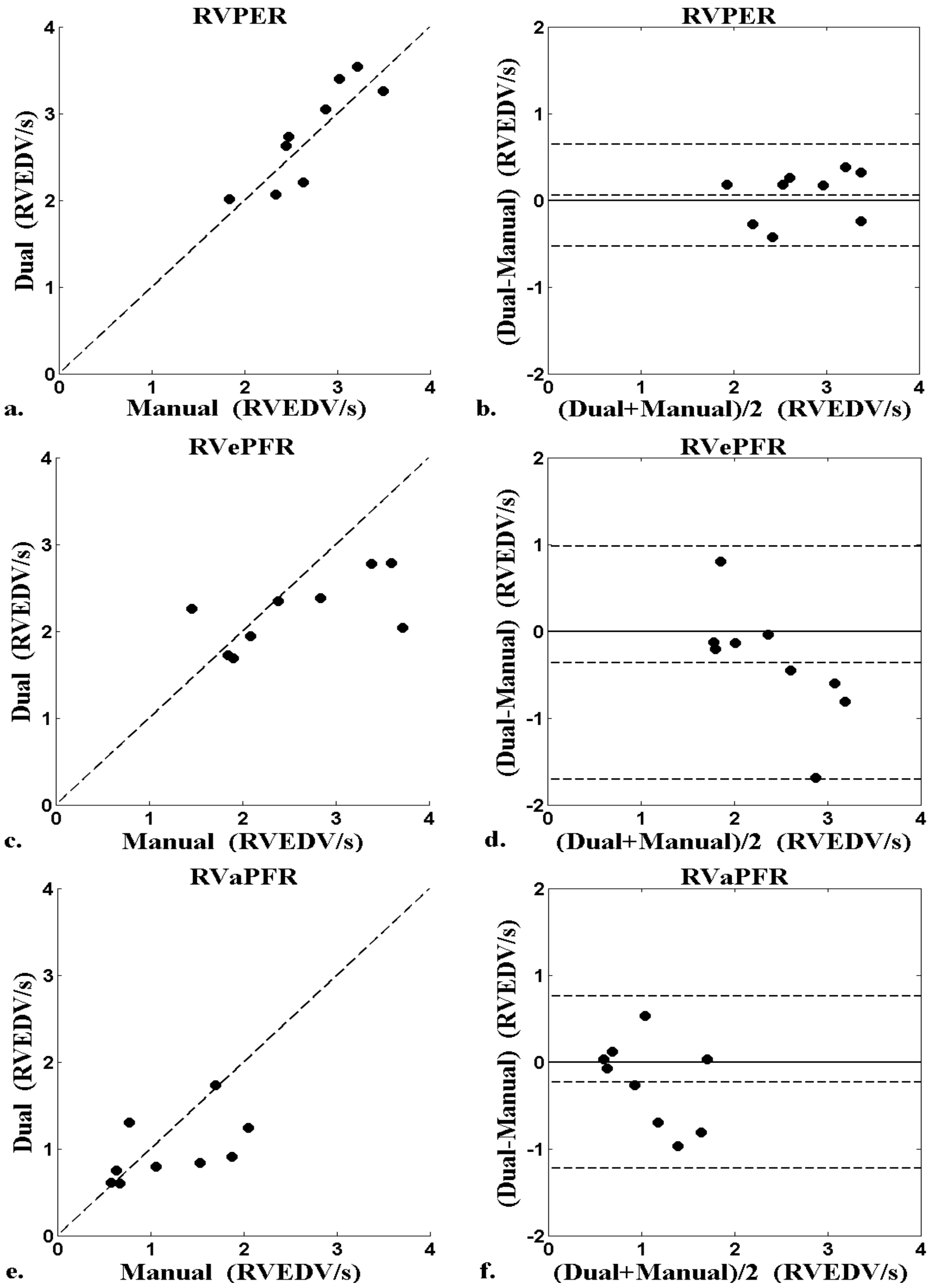

Figure 4.7 Comparison of RV ejection and filling rates computed from manual and dual contours (RVPER (a, b), RVePFR (c, d) and RVaPFR (e, f) resulted from manual-drawn (Manual) and dual-propagated (Dual) contours are compared via scatter plots and Bland-Altman plots. The black dashed line in scatter plots represents perfect correlation. The dashed lines in Bland-Altman plots represent the mean and mean ± two standard deviations of the difference between Dual and Manual rates)

4.4.5 Inter-user Variability

No significant differences are observed between RVEDV, RVESV, RVEF, RVPER, RVePFR, and RVaPFR values computed from contours propagated with ED and ES contours drawn by two different users (Table 4.4). RVEDV, RVESV, RVEF, and RVPER are highly correlated between the two users. Figures 4.8 and 4.9 show scatter and Bland-Altman plots comparing measurements of RVEDV, RVESV, RVEF, RVPER, RVePFR, and RVaPFR between the two users.

Table 4.4 Inter-user variability in RV volume related measurements

	Mean ± SE	P (Difference)	ρ	P(ρ)
RVEDV (ml)	2.38 ± 1.55	.16	.99	<.0001
RVESV (ml)	-1.33 ± 1.77	.47	.96	<.0001
RVEF (%)	.14 ± .89	.88	.94	.00021
RVPER (RVEDV/sec)	-.06 ± .09	.56	.88	.0017
RVePFR (RVEDV/sec)	-.06 ± .13	.66	.65	.056
RVaPFR (RVEDV/sec)	.20 ± .11	.12	.47	.20

Differences are User2 - User1. ρ: correlation coefficient.

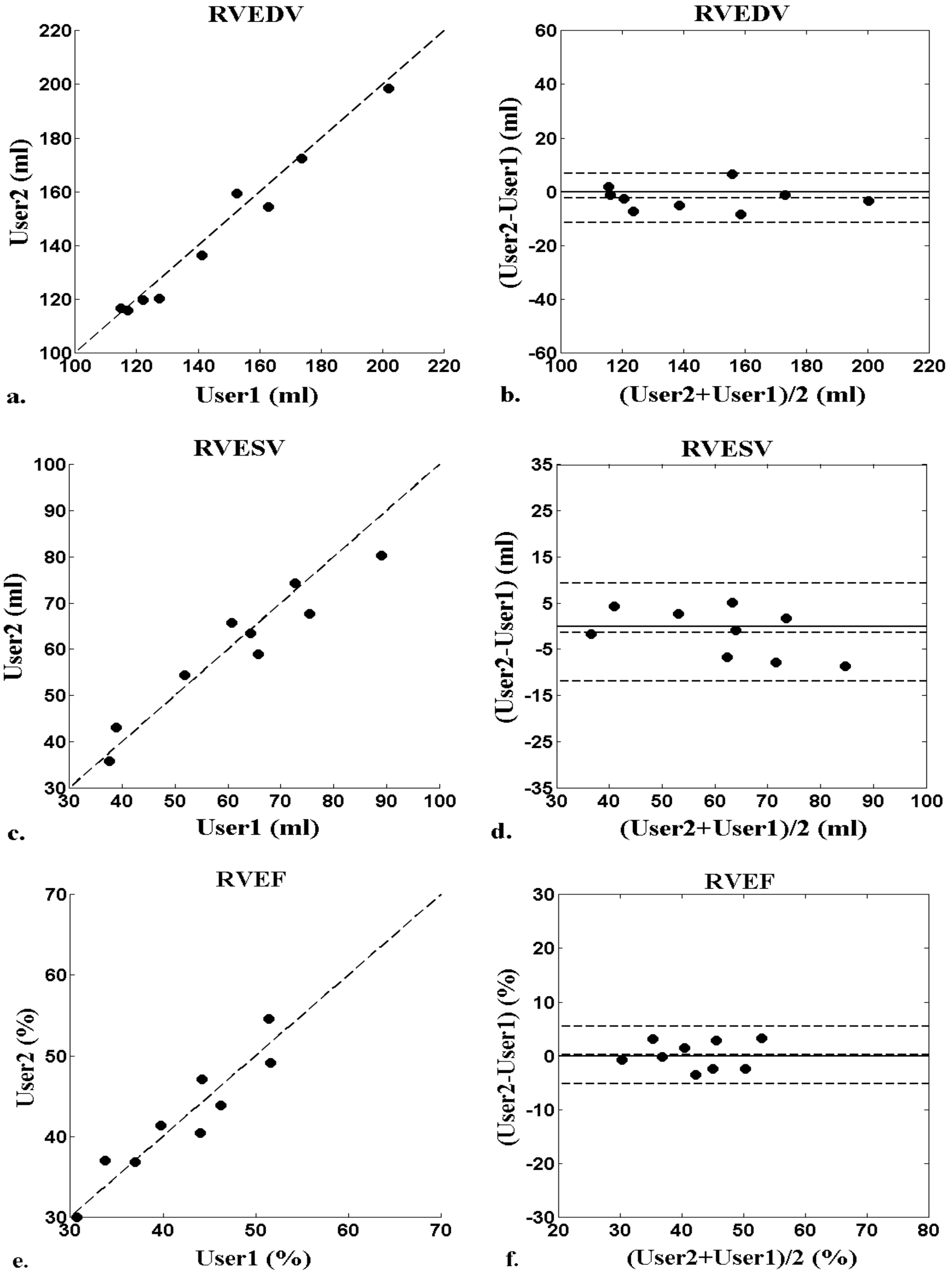

Figure 4.8 Inter-user comparison of RV volumetric measurements
(RVEDV (a, b), RVESV (c, d), and RVEF(e, f) values computed from contours manually drawn at ED and ES by two different users are compared via scatter plots and Bland-Altman plots. The black dashed line in scatter plots represents perfect correlation. The dashed lines in Bland-Altman plots represent the mean and mean ± two standard deviations of the difference between User1 and User2)

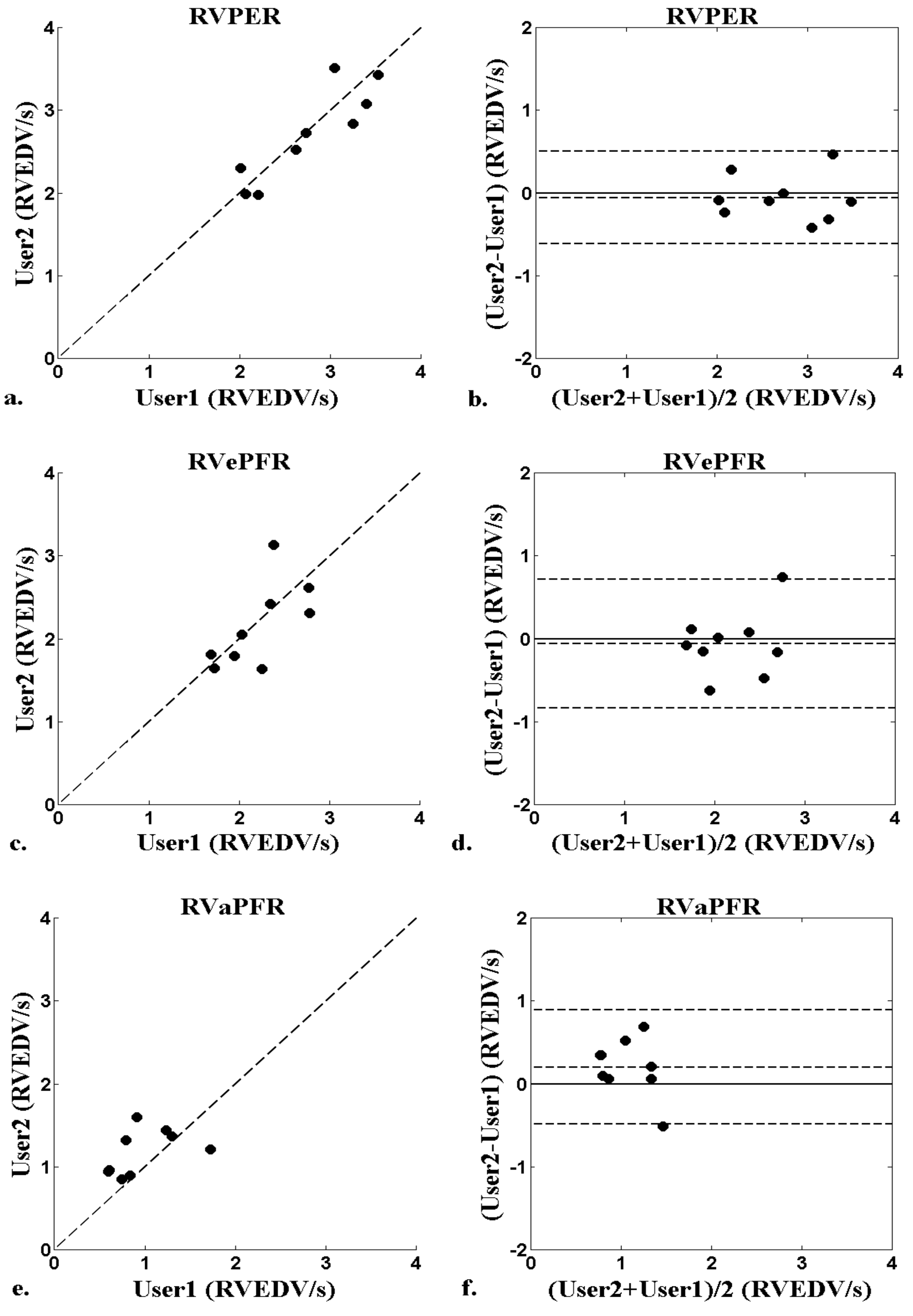

Figure 4.9 Inter-user comparison of RV ejection and filling rates
(RVPER (a, b), RVePFR (c, d), and RVaPFR(e, f) values computed from contours manually drawn at ED and ES by two different users are compared via scatter plots and Bland-Altman plots. The black dashed line in scatter plots represents perfect correlation. The dashed lines in Bland-Altman plots represent the mean and mean ± two standard deviations of the difference between User1 and User2.)

4.5 Discussion

In this chapter, we describe a novel dual-contour propagation technique for measuring RV VTCs. This method requires only standard short-axis and long-axis CMR acquisitions and routinely drawn ED and ES contours. We show that the dual-propagated contours can be used to accurately measure peak ejection and filling rates compared to the reference standard of manually-drawn contours. The dual-contour propagation technique provides a fast, practical means of measuring volume-based indices of RV systolic and diastolic ventricular function from routine clinical CMR.

A strength of our study lies in the internal validation of propagated RV contours by comparing RVSV to LVSV from the same study as a reference standard. We have previously shown [55, 56] measurements of ventricular volumes can be validated in animal models. Use of animals may be useful for validation, but there are significant differences in the RV shape between animals and humans. Nuclear medicine measurement of RV VTCs using multi gated acquisition scan (MUGA) or first pass radionuclide angiography [57] are limited by overlap of arterial counts at the base. People have also measured RV VTCs using echocardiography [24, 58], but the geometric assumptions used in 2D echocardiography are not valid in the RV, and 3D echocardiography underestimates RV volumes relative to CMR [24, 59]. Doppler derived measurements of flow are not directly related to RV VTCs because flow can only be measured in a specific direction.

We and other investigators have demonstrated the role of TA motion to RV function [30, 60-62]. The results in Figure 4.6 further emphasize the importance of taking tricuspid annular excursion into account for calculation of RV stroke volumes. RV and LV stroke volumes were not significantly different only when TA/MA motion was incorporated into the volume computations.

Compared to manually drawn contours and manually-selected slices, the RVSV and LVSV by dual propagation with TA/MA tracking were significantly larger due to significantly lower LVESV and RVESV. However, dual propagation with TA/MA tracking resulted in no significant differences between RV and LV stroke volumes. RV and LV stroke volumes from manual contouring and manually selected slices were significantly different. This difference was because basal slices were either included or excluded as a whole, which, in this small group, produced an 18ml mean difference in SV. However, this difference can be attributed to manual slice selection since manually drawn contours with TA/MA tracking produced no significant differences in stroke volumes.

Techniques have been developed for automatically segmenting the RV and generating RV contours [63-66], and these techniques continue to improve. However, user correction of the contours is almost always required. The dual-contour propagation technique presented in this paper can be utilized equally well with either manually drawn contours or automatic contours with manual correction. The propagation algorithm simply propagates the contour information specified by the user at the ED and ES phase to the other imaged time frames.

RV ED and ES contours are routinely drawn to compute RV volumes and EF. With the contour propagation technique described in this paper, an entire VTC can be generated in approximately 5 min. In addition to potential improvements in accuracy and reproducibility, functional parameters such as RV filling and ejection rates can also be computed. One of the potential benefits of increased accuracy and reproducibility in RV functional parameters is a reduction in the number of patients needed in clinical trials to achieve a certain level of statistical power [23, 29, 67].

A limitation of contour propagation algorithms in general is that any errors in the seed contours get propagated to all other time frames. Consequently, it is especially important to ensure accurate seed contours before propagation. Also, we did not prospectively apply the contour propagation techniques in this paper to a clinical population, although such a study is currently in progress.

4.6 Conclusion

In conclusion, a novel protocol for RV volumetric analysis from routine clinical CMR is proposed and validated. The dual-contour propagation technique provides a fast, accurate and practical means of measuring RV volume-based indices such as RVEDV, RVESV, RVSV, and RVEF.

Chapter 5 Geometrical LV Remodeling

Nearly half of all patients with heart failure have a preserved ejection fraction (HFPEF) [68-70]. Hypertensive left ventricular disease is the most common condition causing heart failure [12-14]. Recent studies [71, 72] have reported that in hypertensive patients with preserved or supranormal LVEF relative to non-hypertensive normal patients, the circumferential shortening strain is depressed. The reasoning behind this apparent paradox has not been systematically evaluated. It has been reported that reduced long-axis shortening is compensated for by increased short-axis shortening in HFPEF [73, 74]. However, more recent investigations argued that in HFPEF in the setting of reduced circumferential and longitudinal strain this phenomenon is explained by relatively normal wall thickening due to an increased end-diastolic wall thickness [75, 76].

LV is often modeled by a simplified incompressible cylindrical model or an ellipsoidal model and EF is calculated as a function of geometry and shortening. Cine MRI has been widely used to assess quantitative cardiac function for clinical practice. Tagged MRI allows non-invasive assessment of 3D LV remodeling and particularly myocardial strain.

In this chapter, we adopt the prolate spheroidal B-spline model and develop an analytic framework relating EF to a few relatively easily measured parameters: LV wall thickness, radius-to-wall thickness ratio, longitudinal shortening quantified from cine MRI and circumferential strain measured by tagged MRI. Then we test the hypothesis that preserved EF in the presence of reduced circumferential shortening strain in HTN is due to geometric effects of concentric remodeling.

5.1 Left Ventricular Concentric Remodeling

Concentric remodeling is commonly conceptualized as an adaptation to increased pressure overload caused by conditions such as hypertension. The transition from compensatory adaptation to myocardial dysfunction is not completely understood in humans. In concentric remodeling, the wall thickness is relatively normal but LV mass is increased. Left ventricular hypertrophy refers to an absolute increase in LV mass height ratio. Concentric LVH is a combination of increased mass height ratio and higher RT ratio. Concentric LVH has depressed midwall and long-axis shortening despite normal EF.

In [77], the LV chamber and myocardial function is assessed by a linear regression fitting of circumferential ES wall stress to endocardial and midwall FS. Chamber function was assessed as percent FS. Myocardial function was assessed by percent circumferential FS at midwall and was calculated using a two-shell cylindrical model. Higher RT ratio rather than hypertrophy is related to lower values for indexes of systolic function. Concentric-remodeling patients may appear to have reduced endocardial shortening relative to hypertensive patients with normal LV mass and RT ratio.

Another recent study used measurements from MRI rather than echocardiographic measurements on concentric remodeling. This study [78] documented a gradual reduction in global and regional myocardial function with increasing magnitudes of LV concentric remodeling. Peak global systolic strain was defined as the peak midwall E_{cc} averaged across all segments; and peak regional systolic function was the peak midwall E_{cc} averaged over the corresponding coronary region. LV concentric remodeling was associated with decreased global and regional systolic function.

5.2 Mathematical Derivation of a Simple, Analytic Concentric Remodeling

In cine images, ED and ES are defined as the phase with the largest and smallest LV areas respectively. Both phases are identified by visual inspection of the image data of a cardiac cycle. In all slices, LV endocardial and epicardial contours were manually drawn at ED and ES.

Based on the consideration that the endocardial portion of the LV wall thickens more than the epicardial portion [79], LV wall is separated into three shells: subendocardial shell (endo), middle shell (mid-wall), and subepicardial shell (epi). The LV wall is divided into 17 segments for assessment of the myocardium and sectioned perpendicular to the LV long axis into three levels: base, mid-cavity (mid) and apex [80] by averaging the segmental values in each level. Parameters were not computed at the apex (segment 17). The strain and geometric parameters mentioned in the following sections are computed at each of the above-mentioned locations.

Tag lines at ES are tracked with the combined tag tracking and strain reconstruction method [81] and then adjusted by expert users if necessary. 3D myocardial displacement and Lagrangian strain are computed by fitting a B-spline deformation model defined in prolate spheroidal coordinates to tag line data [82]. 3D radial thickening (E_{rr}), circumferential shortening (E_{cc}), and longitudinal shortening (E_{ll}) were reconstructed and measured.

5.2.1 Simplified Strain Computation in Prolate Spheroidal Coordinates

The prolate spheroidal coordinate system as shown in Figure 5.1 is used to compute 3D strain. The relationship between a point in Cartesian coordinates (x, y, z) and its corresponding prolate spheroidal coordinates (λ, ϕ, θ) is

$$x = f sinh\lambda\ sin\phi\ cos\theta \tag{5.1}$$

$$y = f sinh\lambda\ sin\phi\ sin\theta \tag{5.2}$$

$$z = f cosh\lambda\ cos\phi \tag{5.3}$$

where $\lambda \in [0, \infty), \phi \in [0, \pi], \theta \in [0,2\pi)$ and f is the focal radius.

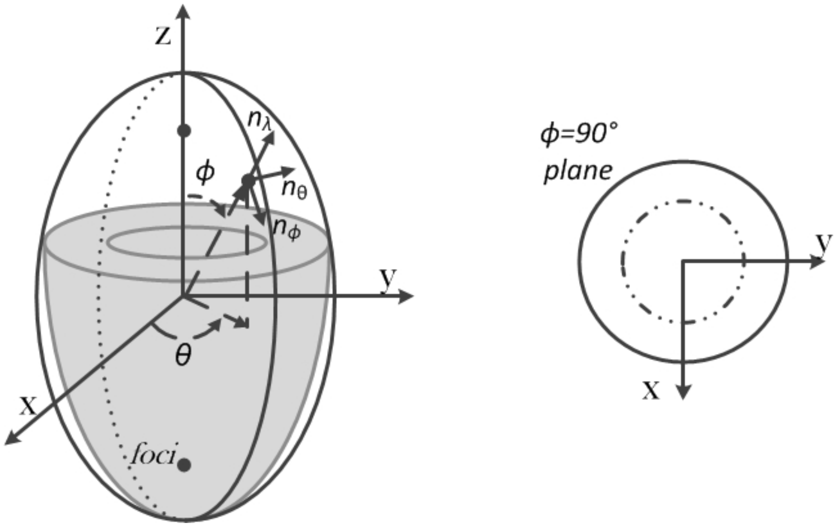

Figure 5.1 Prolate spheroidal coordinate system
(LV prototype shown in dark grey on the left; a circumferential cross section shown on the right)

A point $\vec{u}$ on the surface is therefore represented as,

$$\vec{u} = u_\lambda \vec{e}_\lambda + u_\phi \vec{e}_\phi + u_\theta \vec{e}_\theta$$

$$= f \sinh\lambda \, \sin\phi \, \cos\theta \vec{\imath} + f \sinh\lambda \, \sin\phi \, \sin\theta \vec{\jmath} + f \cosh\lambda \, \cos\phi \vec{k} \tag{5.4}$$

where ($\vec{e}_\lambda,\ \vec{e}_\phi,\ \vec{e}_\theta$) and ($\vec{\imath}, \vec{\jmath}, \vec{k}$) are the unit vectors in prolate spheroidal and Cartesian coordinates respectively.

The two sets of unit vectors can be related as,

$$\vec{e}_\lambda = \frac{\sinh\lambda \cos\phi (\cos\theta \vec{\imath} + \sin\theta \vec{\jmath}) + \sinh\lambda \cos\phi \vec{k}}{\left(\cosh^2\lambda \sin^2\phi + \sinh^2\lambda \cos^2\phi\right)^{.5}} \tag{5.5}$$

$$\vec{e}_\phi = \frac{\sinh\lambda \cos\phi (\cos\theta \vec{\imath} + \sin\theta \vec{\jmath}) - \cosh\lambda \sin\phi \vec{k}}{\left(\sinh^2\lambda \cos^2\phi + \cosh^2\lambda \sin^2\phi\right)^{.5}} \tag{5.6}$$

$$\vec{e}_\theta = -\sin\theta \vec{\imath} + \cos\theta \vec{\jmath} \tag{5.7}$$

The partial derivatives with respect to each unit vector can be calculated and then related to the above three unit vectors as follows.

$$\begin{cases} \dfrac{\partial \vec{\mathrm{e}}_\lambda}{\partial \lambda} = A\vec{\mathrm{e}}_\lambda + B\vec{\mathrm{e}}_\phi; \\ \dfrac{\partial \vec{\mathrm{e}}_\lambda}{\partial \phi} = E\vec{\mathrm{e}}_\lambda + F\vec{\mathrm{e}}_\phi; \\ \dfrac{\partial \vec{\mathrm{e}}_\lambda}{\partial \theta} = M \cosh\lambda \sin\phi \vec{\mathrm{e}}_\theta; \end{cases} \tag{5.8}$$

$$\begin{cases} \dfrac{\partial \vec{\mathrm{e}}_\phi}{\partial \lambda} = G\vec{\mathrm{e}}_\lambda + H\vec{\mathrm{e}}_\phi; \\ \dfrac{\partial \vec{\mathrm{e}}_\phi}{\partial \phi} = C\vec{\mathrm{e}}_\lambda + D\vec{\mathrm{e}}_\phi; \\ \dfrac{\partial \vec{\mathrm{e}}_\phi}{\partial \theta} = M \sinh\lambda \cos\phi \vec{\mathrm{e}}_\theta; \end{cases} \tag{5.9}$$

$$\begin{cases} \dfrac{\partial \vec{\mathrm{e}}_\theta}{\partial \lambda} = 0; \\ \dfrac{\partial \vec{\mathrm{e}}_\theta}{\partial \phi} = 0; \\ \dfrac{\partial \vec{\mathrm{e}}_\theta}{\partial \theta} = -M(\cosh\lambda \sin\phi \vec{\mathrm{e}}_\lambda + \sinh\lambda \cos\phi \vec{\mathrm{e}}_\phi); \end{cases} \tag{5.10}$$

where

$$\begin{cases} A = C - M^2 \sinh\lambda \cosh\lambda; \\ B = M^2 \sinh\lambda \cos\phi(\sinh\lambda \sin\phi - \coth\lambda \cosh\lambda \sin\phi); \\ C = \coth\lambda + M^2 \cosh\lambda \sin\phi(\sinh\lambda \sin\phi - \coth\lambda \cosh\lambda \sin\phi); \\ D = B - M^2 \sin\phi \cos\phi; \\ E = G - M^2 \sin\phi \cos\phi; \\ F = M^2 \sinh\lambda \cos\phi(\cosh\lambda \cos\phi - \tanh\lambda \sinh\lambda \cos\phi) + \tanh\lambda; \\ G = M^2 \cosh\lambda \sin\phi(\cosh\lambda \cos\phi - \tanh\lambda \sinh\lambda \cos\phi); \\ H = F - M^2 \sin\phi \cos\phi; \\ M = \cosh^2\lambda - \cos^2\phi; \end{cases} \tag{5.11}$$

Let $P(\lambda, \phi, \theta)$ denote a scalar function of position in prolate spheroidal coordinates. The gradient of P is denoted by

$$\nabla P = P\left(\frac{M}{f}\frac{\partial}{\partial \lambda}\vec{e}_\lambda + \frac{M}{f}\frac{\partial}{\partial \phi}\vec{e}_\phi + \frac{1}{f sin\hbar\lambda sin\phi}\frac{\partial}{\partial \theta}\vec{e}_\theta\right) \tag{5.12}$$

$$= \vec{e}_\lambda \frac{M}{f}\frac{\partial P}{\partial \lambda} + \vec{e}_\phi \frac{M}{f}\frac{\partial P}{\partial \phi} + \vec{e}_\theta \frac{1}{fsinh\lambda sin\phi}\frac{\partial P}{\partial \theta}$$

Let $\vec{u}$ be the displacement vector, the gradient of $\vec{u}$ is a second order tensor *G* which can be presented as a dyadic product [83, 84] of the vector with the gradient operator ∇ as

$$\begin{aligned}
G &= \vec{u} \otimes \nabla \\
&= (u_\lambda \vec{e}_\lambda + u_\phi \vec{e}_\phi + u_\theta \vec{e}_\theta) \otimes (\vec{e}_\lambda \frac{M}{f}\frac{\partial}{\partial \lambda} + \vec{e}_\phi \frac{M}{f}\frac{\partial}{\partial \phi} + \vec{e}_\theta I \frac{\partial}{\partial \theta}) \\
&= \frac{M}{f}\frac{\partial}{\partial \lambda}(u_\lambda \vec{e}_\lambda) \otimes \vec{e}_\lambda + \frac{M}{f}\frac{\partial}{\partial \phi}(u_\lambda \vec{e}_\lambda) \otimes \vec{e}_\phi + I\frac{\partial}{\partial \theta}(u_\lambda \vec{e}_\lambda) \otimes \vec{e}_\theta \\
&\quad + \frac{M}{f}\frac{\partial}{\partial \lambda}(u_\lambda \vec{e}_\phi) \otimes \vec{e}_\lambda + \frac{M}{f}\frac{\partial}{\partial \phi}(u_\lambda \vec{e}_\phi) \otimes \vec{e}_\phi + I\frac{\partial}{\partial \theta}(u_\lambda \vec{e}_\phi) \otimes \vec{e}_\theta \\
&\quad + \frac{M}{f}\frac{\partial}{\partial \lambda}(u_\lambda \vec{e}_\theta) \otimes \vec{e}_\lambda + \frac{M}{f}\frac{\partial}{\partial \phi}(u_\lambda \vec{e}_\theta) \otimes \vec{e}_\phi + I\frac{\partial}{\partial \theta}(u_\lambda \vec{e}_\theta) \otimes \vec{e}_\theta
\end{aligned} \tag{5.13}$$

where $I = 1/fsin\hbar\lambda sin\phi$. Expanding the dyadic product and substituting the partial derivatives derived above, the deformation gradient tensor can be organized in a matrix representation as

$$\begin{aligned}
G &= \begin{bmatrix} G_{\lambda\lambda} & G_{\lambda\phi} & G_{\lambda\theta} \\ G_{\phi\lambda} & G_{\phi\phi} & G_{\phi\theta} \\ G_{\theta\lambda} & G_{\theta\phi} & G_{\theta\theta} \end{bmatrix} \\
&= \begin{bmatrix} \frac{M}{f}(\frac{\partial u_\lambda}{\partial \lambda} + Au_\lambda + Gu_\phi) & \frac{M}{f}(\frac{\partial u_\lambda}{\partial \phi} + Eu_\lambda + Cu_\phi) & I(\frac{\partial u_\lambda}{\partial \theta} - u_\theta M \cosh\lambda \sin\phi) \\ \frac{M}{f}(\frac{\partial u_\phi}{\partial \lambda} + Bu_\lambda + Hu_\phi) & \frac{M}{f}(\frac{\partial u_\phi}{\partial \phi} + Fu_\lambda + Du_\phi) & I(\frac{\partial u_\phi}{\partial \theta} - u_\theta M \sinh\lambda \cos\phi) \\ \frac{M}{f}\frac{\partial u_\theta}{\partial \lambda} & \frac{M}{f}\frac{\partial u_\theta}{\partial \phi} & \begin{array}{l} I(\frac{\partial u_\theta}{\partial \theta} + u_\phi M \sinh\lambda \cos\phi \\ + u_\lambda M \cosh\lambda \sin\phi) \end{array} \end{bmatrix}
\end{aligned} \tag{5.14}$$

With the assumptions that the displacement occurs only along λ direction and strain is evaluated at base with $\Phi = 90°$, we have $u_\phi(\lambda, \phi, \theta) = 0$; $u_\theta(\lambda, \phi, \theta) = 0$; $\partial u_\lambda/\partial \phi = 0$; and $\partial u_\lambda/\partial \theta = 0$. *G* is therefore simplified as

$$G = \begin{bmatrix} \dfrac{M}{f}\dfrac{\partial u_\lambda}{\partial \lambda} & 0 & 0 \\ 0 & \dfrac{M}{f} u_\lambda \tanh \lambda & 0 \\ 0 & 0 & I u_\lambda \end{bmatrix}. \tag{5.15}$$

5.2.2 Relating Strain Tensor to Fractional Shortening

With ejection in the absence of torsion, myofibers would shorten more in the endo than in the epi due to the incompressibility of the LV wall as illustrated in Figure 5.2.

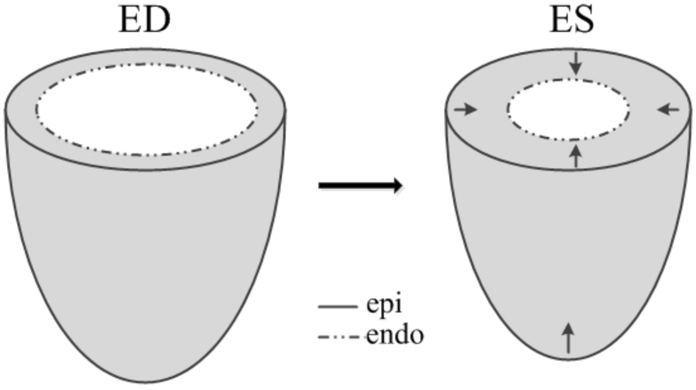

Figure 5.2 Illustration of LV wall deformation from ED to ES along radial direction

The Lagrangian strain tensor, $E = (G + G^T + G^T G)/2$, becomes

$$E = \begin{bmatrix} \dfrac{M}{f}\dfrac{\partial u_\lambda}{\partial \lambda}\left(\dfrac{M}{2f}\dfrac{\partial u_\lambda}{\partial \lambda}+1\right) & 0 & 0 \\ 0 & \dfrac{M}{f} u_\lambda \tanh \lambda \left(\dfrac{M}{2f} u_\lambda \tanh \lambda + 1\right) & 0 \\ 0 & 0 & I u_\lambda \left(I u_\lambda / 2 + 1 \right) \end{bmatrix} \tag{5.16}$$

The terms along the diagonal of the strain tensor are E_{rr}, E_{ll}, and E_{cc} respectively.

The heart contraction from ED to ES results in a displacement of $u_\lambda$in the $\phi = 90°$ plane. Hence, the fractional shortening can be represented as

$$FS = -\frac{u_{\lambda}}{(x^2+y^2)^{.5}\,|_{\phi=90^\circ}} = -\frac{u_{\lambda}}{f\sinh\lambda} = -I\,|_{\phi=90^\circ}\, u_{\lambda}; \tag{5.17}$$

Substituting in the above relation into the E_{cc} expression, FS can be related to 3D E_{cc} as

$$FS = 1-\sqrt{1+2E_{cc}} \tag{5.18}$$

where E_{cc} is restricted in the range (-.5, 0) to ensure that FS falls in (0,1).

To evaluate the derived relationship, the measurements of E_{cc} at mid were collected and used to calculate the FS at the mid shell. This model accounted for radial thickening and circumferential shortening but not torsion.

5.2.3 Converting FS at Endocardium to Mid-wall

All geometric parameters were measured from cine images by annotating myocardium at ED and ES. The papillary muscles were excluded from endocardial contours. An incompressible and homogeneous myocardium with constant specific gravity is assumed.

The wall thickness at ED (WT^{ED}) was computed by averaging all the segmental measurements at base. The radius of curvature to wall thickness ratio (RT) was computed as the reciprocal of the product of the endocardial circumferential curvature and wall thickness.

Let R_{endo}, and R_{mid} be the radii of the inner shell and mid wall of the myocardium. Assume wall thickness, T, is a constant in the ventricle along the circumferential direction at a timeframe. The relation between the radii can consequently be represented as $R_{endo} = R_{mid} - T/2$. The formula,

$$FS_{endo} = (R_{endo}^{ED} - R_{endo}^{ED}) / R_{endo}^{ED} \tag{5.19}$$

can be reformulated as

$$FS_{endo} = \frac{(R_{mid}^{ED} - \frac{T^{ED}}{2}) - (R_{mid}^{ES} - \frac{T^{ES}}{2})}{R_{mid}^{ED}} \cdot \frac{R_{mid}^{ED}}{R_{mid}^{ED} - T^{ED}/2} \tag{5.20}$$

Substituting in the wall thickening, $WT = (T^{ED} - T^{ES})/T^{ED}$, the above equation yields

$$FS_{endo}=\left(FS_{mid}+WT\cdot\frac{T^{ED}/2}{R_{mid}^{ED}}\right)\cdot\frac{R_{mid}^{ED}}{R_{endo}^{ED}} \tag{5.21}$$

Let $RT_{endo}^{ED}=R_{endo}^{ED}/T^{ED}$ denote the radius thickness ratio at endocardium at ED. The above equation can be further simplified as

$$FS_{endo}=\left(1+\frac{.5}{RT_{endo}^{ED}}\right)\cdot FS_{mid}+.\frac{.5}{RT_{endo}^{ED}}\cdot WT \tag{5.22}$$

The predicted FS_{mid} from Equation (5.18) can be converted to FS_{endo} as follows.

$$FS_{endo}=\left(1+\frac{.5}{RT_{endo}^{ED}}\right)\cdot(1-\sqrt{1+2E_{cc}})+\frac{.5}{RT_{endo}^{ED}}\cdot WT^{ED} \tag{5.23}$$

5.2.4 Relating Fractional Shortening to Ejection Fraction

In the prolate spheroidal coordinates, LV endocardial volume can be represented by $V=2\pi d^2 l/3$, where d is circumferential radius, l is longitudinal length that is computed as the distance between apex and base from the LV endocardial contours drawn on a four-chamber view. Thus, the ejection fraction can be computed by

$$EF=\frac{\text{Stroke Volume}}{\text{EDV}}=\frac{V_{ED}-V_{ES}}{V_{ED}}=\frac{d_{ED}^2 l_{ED}-d_{ES}^2 l_{ES}}{d_{ED}^2 l_{ED}} \tag{5.24}$$

FS can be denoted as $(d_{ED}-d_{ES})/d_{ED}$. Similarly, 2D longitudinal shortening (LS) was calculated as the longitudinal length difference between ED and ES divided by the longitudinal length at ED, which is $(l_{ED}-l_{ES})/l_{ED}$. Thus, d_{ES} and l_{ES} can be substituted by $d_{ES}=d_{ED}(1-FS)$ and $l_{ES}=l_{ED}(1-FS)$ respectively. With these substitutions, EF can be written as

$$EF=1-(1-FS)^2(1-LS). \tag{5.25}$$

Substituting *FS* by Equation (5.23) leads to:

$$EF_{pred}=1-\left(1-\left[\left(1+\frac{.5}{RT_{endo}^{ED}}\right)\cdot(1-\sqrt{1+2E_{cc}})+\frac{.5}{RT_{endo}^{ED}}\cdot WT^{ED}\right]\right)^2(1-LS) \tag{5.26}$$

EF_{pred} was calculated in each subject using Equation (5.26) with measured Ecc_{mid}, WT^{ED}, LS, and RT^{ED} values and compared to measured ejection fraction values $EF_{measured}$.

5.3 Experimental Design

A total of 356 human subjects underwent the cine and tagged MRI from 2005 to 2010. The study protocol was approved by the Institutional Review Board at both the University of Alabama at Birmingham and Auburn University, and all participants gave written informed content. The subjects represented a variety of conditions: 74 normal volunteers (mean ± SD age 43±14 years, range 20 to 70), 73 resistant hypertension (> 140/90 mmHg) determined at two or more clinic visits (mean ± SD age 55±10 years, range 27 to 79), 64 patients with volume overload (mean ± SD age 53±11 years, range 21 to 69), 55 mitral valve regurgitation (mean ± SD age 54±12 years, range 25 to 79) and 117 myocardial infarction (mean ± SD age 58±11 years, range 36 to 81).

Cine images were acquired in standard two- and four-chamber, short-axis and long-axis views on a 1.5T GE MRI system using Electrocardiographically gated (ECG) breath-hold steady-state free precision technique with the following parameters: slice thickness 8 mm, zero interslice gap, field-of-view 40 × 40 cm, scan matrix 256 ×128, flip angle = 45 degrees, TR/TE=3.8/1.6 ms, typical acquired temporal resolution < 50 ms. The short-axis stack was prescribed from an end-diastolic four-chamber image, centered parallel to mitral annulus and perpendicular to septum, starting at 1 cm proximal to mitral valve and ending at 1 cm beyond the apex.

Tagged images were acquired with a fast gradient-echo cine sequence with the same slice prescription as above using spatial modulation of magnetization (SPAMM) method with the following parameters: prospective ECG gating, FOV = 40 × 40 cm, scan matrix = 256 × 128, flip angle = 10 degrees, TR/TE = 8.0/4.2 ms, number of reconstructed cardiac phases = 20, slice thickness = 8 mm, tag spacing 7 mm, views per segment = 10.

All the subjects were included in the comparison between the EF_{pred} and $EF_{measured}$ regardless of the subject's group. A paired t-test, scatter plot, and Bland-Altman plot were used for comparison. The level of significance was defined as p-value < .05. A linear regression model is adopted to investigate the influence of torsion, twist, principle strains and myocardium mass on EF which was not included in the analytic EF_{pred} statistically.

Functional parameters such as wall thickness, EF, FS, and E_{cc} etc were compared between hypertensive patients and normals using unpaired t-tests. Values are expressed as the mean ± standard error.

5.4 Results

5.4.1 Validation on the Prediction of Ejection Fraction

The paired t-test suggested that EF_{pred} is significantly different from $EF_{measured}$ with a p-value <.0001. Their correlation coefficient is .80 (P<.0001). The scatter plot in Figure 5.3 shows a strong positive correlation between EF_{pred} and $EF_{measured}$ with a correlation coefficient of .80 (P<.0001). The regression procedure finds $EF_{measured} = 1.15EF_{pred}$ with P<.0001. The R^2 is .52. EF_{pred} tends to be lower than $EF_{measured}$.

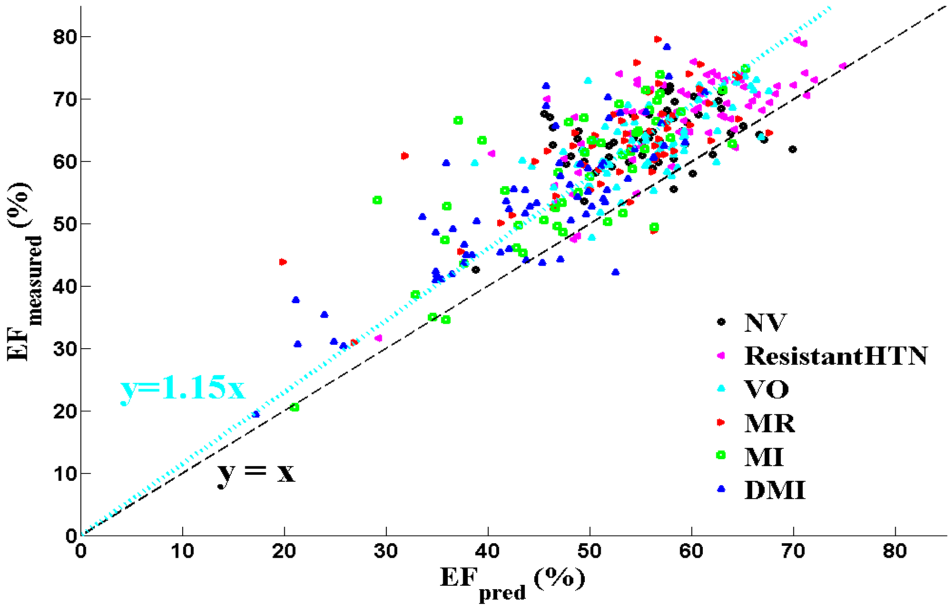

Figure 5.3 Scatter plot of the predicted and measured EF
(The black line indicates perfect correlation. NRM: normal volunteers; HTN: hypertension; VO: volume overload; MR: mitral regurgitation; MI: myocardial infarction; DMI: diabetic myocardial infarction.)

5.4.2 Significance of Preserved Ejection Fraction despite Depressed E_{cc}

Hypertension group (n=73) is compared to the normal volunteers (n=74). From the results in Table 5.1, in hypertension, wall thickness at ED is significantly increased; 3D midwall E_{cc} and RT ratio at ED is significantly reduced; and FS and EF are increased; LS is similar to normal volunteers. Referring to the equations (5.23) and (5.26), these observed changes in HTN lead to an expected increase in FS and EF, consistent with the observed EF (i.e., similar EF between NRM and HTN even in the setting of lower E_{cc}).

Table 5.1 Statistic comparison between normal volunteers (NRM) and hypertension (HTN)

Functional Parameters	NRM (n=74)	HTN (n=73)
Wall thickness ED (cm)	0.68 ± 0.02	0.88 ± 0.02*
Wall thickness ES (cm)	1.11 ± 0.03	1.51 ± 0.03*
LS (%)	22.62 ± 0.81	21.91 ± 0.75
Wall thickening (%)	65.99 ± 2.47	75.52 ± 2.63*
RT ratio ED (-)	3.94 ± .09	3.07 ± 0.08*
FS (%)	29.42 ± 0.83	32.23 ± 0.88*
EF (%)	64.45 ± 0.73	67.27 ± 0.88*
E_{cc} (%)	15.61 ± 0.25	14.23 ± 0.37*
E_{ll} (%)	12.26 ± 0.32	10.30 ± 0.42*

LS: longitudinal shortening; RT ratio ED: radius-to-wall thickness ratio at end diastole; FS: fractional shortening; EF: ejection fraction; E_{cc}: circumferential strain; E_{ll}: longitudinal strain; $Emax$: Principle strain; Values are mean ± SE; *P<.05 vs. normal volunteers.

5.5 Discussion

A geometric concentric remodeling of the left ventricle with lower R:T ratio in HTN compared to normals is proposed to explain the preserved or even supranormal ejection fraction seen in hypertension. By comparing various LV functional parameters between hypertension and normals, we demonstrate that the well-known changes seen in hypertension (with increased LV mass, thicker walls, smaller RT ratio, greater wall thickening), are still able to support a normal or high EF even with the observed decreased longitudinal (E_{ll}) and circumferential (E_{cc}) strains. Our analytic model provides the mechanistic basis for the observed preservation of EF despite these reduced strains, which is seen to be an immediate consequence of an incompressible LV myocardium along with the thicker walls in HTN. Thus, the preserved EF in hypertension is due to geometric effects of concentric remodeling, as previously hypothesized [85]; our work demonstrates how the geometric changes contribute to the EF.

The lower E_{cc} and LS seen in HTN occur even in the setting of similar maximum shortening (E_{min}) and increased torsion and twist. Indeed, our linear regression fitting suggested that twist is not a direct significant contributor to the ejection fraction, beyond the direct effect of twist which results in simultaneous longitudinal and circumferential shortening.

Several models and experimental studies [86-88] showed that the ratio of LV torsion to endocardial circumferential shortening was found to be a fixed constant value, with small inter-individual variance. In light of the experimental studies on aging in humans via torsion-to-shortening ratio (TSR) comparison [89], our findings indicate that the hypertensive group has a significantly higher TSR (normal volunteers vs. HTN: 0.30±0.00 vs. 0.44±0.00 with P<.0001) as shown in Figure 5.5 and TSR has a good correlation with LV mass-to-EDV ratio (correlation coefficient = .61 with P<.001) and wall thickness (correlation coefficient = .64 with P<.001). The significant increase of mean LV mass-to-EDV (normal volunteers vs. HTN: 0.74±0.00 vs. 0.98±0.00 with P<.0001) in hypertension implies that concentric hypertrophy significantly affected TSR. As discussed in [89], in all known TSR measurements, TSR has never been found to decrease below normal so that subepicardial contractile function never decreases below subendocardial function. The higher TSR implies a reduction of contractile function in the subendocardium relative to that in the subepicardium. This reduction of myocardial contractility may be a result of geometric changes such as wall thickness, LV mass and EDV.

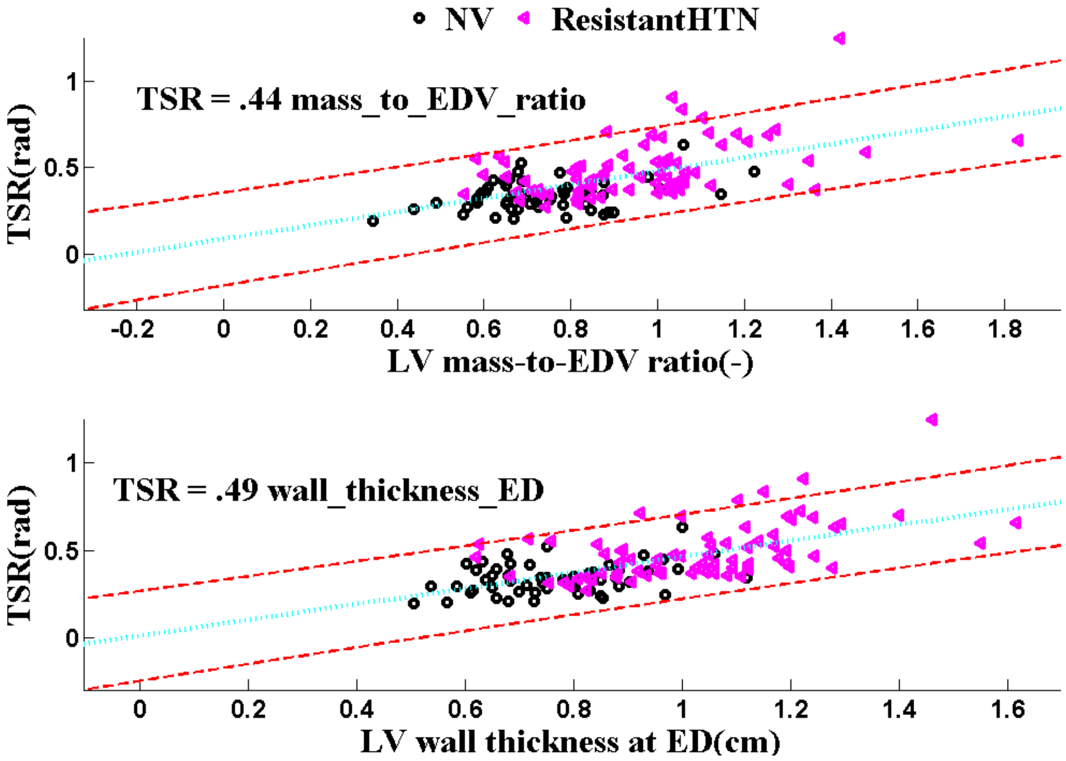

Figure 5.4 TSR comparison between normal (NRM) and hypertension (ResistantHTN)

There are several limitations of this study. First of all, the displacements due to the contraction occur more than just along the radial direction. This assumption was applied to simplify the derivation. Secondly, the study was based on theoretical mathematical modeling with volume calculations based on an idealized left ventricular shape. Even though the model is an idealization, the prolate spheroidal shape is a reasonably realistic approximation of the LV and much closer to the shape of the left ventricle than that of a cylinder and sphere, two other shapes often used to model LV volumes and function.

A final limitation is that torsional deformation is not directly considered in the formula. Torsion depends on relative contractility of the subendocardial and subepicardial myocardium [90, 91] and is influenced by many factors, including pathologic conditions such as a decrease in torsion due to reductions in subendocardial coronary flow reserve [92] and an increase in torsion in patients with aortic valve stenosis and preserved EF [93]. A recent study done via conventional and tissue Doppler echocardiography concluded that torsion and circumferential shortening may be major determinants for maintaining LV pump function, and the latter acts as an independent, most important predictor [72]. Any such attempt to separate strains (circumferential, longitudinal, and radial) and torsion – including that of our model – are obviously artificial since the twisting motion directly leads to shortening in both circumferential and longitudinal directions.

Despite our deliberate neglect of the link between torsion and the strains, our study provides a worthwhile analysis of the direct geometric effects of wall thickening on ejection fraction and demonstrates the mechanism by which the preservation of EF occurs. The reduced strains seen in HTN are sufficient to support contractile function and cardiac output. Thus, the often-held presumption that the reduced strains seen in HTN represent subclinical contractile dysfunction may not be completely accurate. This is further illustrated by the analytic model, since it demonstrates that "normal" values of circumferential and longitudinal strains in the presence of the greater wall thickness in HTN would lead to very high ejection fractions and stroke volumes, higher than that required to support circulatory requirements and cardiac output.

The analytic model we developed provides a direct mechanistic explanation for how the altered geometry seen in HTN, with greater wall thickness, leads to preserved EF even in the presence of reduced LV strain. We validated our model for predicting EF in large groups of patients and a control population. Our relatively simple heart modeling method, making use of only a few assumptions, can predict EF with good accuracy over a wide range of heart conditions and allows immediate estimation and analysis of the effects of various physiologic parameters on the ejection fraction – a parameter that continues to have widespread and everyday use in describing global LV contractile function in both the clinical and research realms. Importantly, our work suggests that preserved ejection fraction in hypertension despite the presence of reduced circumferential shortening is primarily due to the geometric effects of concentric remodeling and may imply that this observed reduction in strains does not necessarily represent subclinical contractile dysfunction.

5.6 Conclusion

The analytic model we developed provides a direct mechanistic explanation for how the altered geometry seen in HTN, with greater wall thickness, leads to preserved EF even in the presence of reduced LV strain. We have validated our model for predicting EF in large groups of patients and a normal volunteer population. Our relatively simple heart modeling method, making use of only a few assumptions, can predict EF with good accuracy over a wide range of heart conditions and allows immediate estimation and analysis of the effects of various physiologic parameters on the ejection fraction—a parameter that continues to have widespread and everyday use in describing global LV contractile function in both the clinical and research realms. Importantly, our work suggests that preserved ejection fraction in hypertension despite the presence of reduced circumferential shortening is primarily due to the geometric effects of concentric remodeling, and may imply that this observed reduction in strains does not necessarily represent subclinical contractile dysfunction.

Chapter 6 Accelerated Dynamic Cardiac MRI

An image sequence is called dynamic if it contains a time series of images at the same slice or volume monitoring a continuously changing process such as periodic cardiac motion, contrast agent uptake, phase contrast flow measurements, etc. The acquisition of such dynamic image sequences is referred to as dynamic imaging.

To capture the dynamic details, both high temporal resolution and good spatial resolution are desired. However, high-resolution scans often demand long imaging time which may not be endurable due to aging or acute sickness. This is particularly the case in clinical cardiac MRI, where most scans require multiple breath-holds. The ability for patients to hold their breath and the breath hold duration they can sustain are critical to the temporal spatial resolution. Therefore, a fast imaging method is of great importance.

The dynamic imaging may be accelerated by utilizing the inherent data redundancy of dynamic images. In dynamic imaging, the motion often occurs only in a small portion of the FOV from time to time; the rest large portion of the FOV mostly remains unchanged and serves as a contrast for motion tracking. It is sufficient to preserve a good temporal, spatial resolution inside the region of interest (ROI) where the motion occurs. The alternative way to explore the data redundancy is that the high-resolution anatomic features do not change from one image to the next; it may be adequate to acquire this stationary anatomic information only once to achieve the desired spatial resolution.

Many methods have been proposed to accelerate dynamic imaging. These include keyhole imaging [94], reduced-encoding with generalized-series reconstruction (RIGR) [95], parallel imaging [96, 97] and reduced FOV techniques [98, 99].

In keyhole imaging, a full *k*-space acquisition for a reference image is collected, followed by repeated acquisition of the central, low-frequency phase encodings at each timeframe. These collected central phase encodings replace the corresponding data from the reference acquisition at every timeframe for reconstruction. In such a way, the reconstructed dynamic images share the same raw data at the large phase encoding amplitudes. The principle behind keyhole imaging is that the low spatial-frequency components of the image control the image contrast; the repeated sampling at low frequencies is sufficient to capture the dynamic behavior, whereas the inserted high-frequency components from the reference scan enhance the spatial resolution.

Unlike keyhole, RIGR modulates the high-frequency data from the reference image to make it consistent with the acquired data, thereby reducing the reconstruction artifacts [95]. RIGR refers to the imaging protocol that uses generalized-series (GS) reconstruction. The GS model, which utilizes the priori constraints for reconstruction, is a three-step approach: first, a proper constraint function is chosen and optimized to describe the boundary information that matches the edges in the dynamic sequence; next, the GS Fourier coefficients are estimated; finally the images are reconstructed by applying a fast Fourier transform to the GS coefficients, zero-padding to the image size, and then multiplying the result by the reference image.

Parallel imaging uses multiple receiver coils to reduce acquisition time significantly. There are two general approaches. One is image based methods that reconstruct images from each coil with reduced FOV and then merge the images using knowledge of individual coil sensitivities such as SENSE [100]. The other is known as *k*-space methods that explicitly calculate missing *k*-space lines before reconstruction such as SiMultaneous Acquisition of Spatial Harmonics (SMASH) [101] and GeneRalized Autocalibrating Partially Parallel Acquisitions (GRAPPA) [102].

When the region of interest is smaller than the object, the image acquisition time can be shortened by reducing the data acquisition in the *k*-*t* space. However, when such a reduced FOV is used, the outside features will alias into the reduced FOV image along the phase encoding direction. In reduced FOV techniques, only a portion of the desired *k*-*t* space data is required, the rest of the data needed for image reconstruction is obtained through various models and approximations. The purpose is to reduce the amount of data needed for a given spatial and temporal resolution. Most existing reduced FOV techniques shorten the acquisition time by undersampling the raw *k*-*t* space data along the phase encoding direction.

The rationale of skipping phase encoding lines is as follows. In the phase encoding direction, each line is separated by the pulse repetition interval, T_R. The total acquisition time is a product of T_R. Taking isolated samples along the phase encoding direction does not speed up the acquisition notably. Frequency encoding acquires a series of time points during a single echo, T_E. Although the encoding methods in each direction are mathematically equivalent, frequency encoding takes much less time than phase encoding. Consequently, the goal of undersampling *k*-space for an N-by-N image is to choose M ($M<N$) phase encoding lines out of N phase encodings.

In 1999, Unaliasing by Fourier-encoding the Overlaps using the temporal Dimension (UNFOLD) was proposed as a flexible way of encoding spatiotemporal information. The aliasing is caused by smaller amounts of acquired spatial information along phase encoding axis. In a dynamic image sequence, several images of an object are acquired; the shift in the sampling function could be varied from image to image. This time-varying shift is used to label and then resolve the various components that are overlapped by modulating their phase as a function of time in a controlled way [98].

Another technique called Noquist [99] was proposed in 2004. With no data substitution and interpolation, it leads to a better reconstructed edge detail than UNFOLD. It defines the static and dynamic regions from the scout image, reduces the number of acquired phase encodings, and reconstructs the whole image sequence columnwise by a direct one-dimensional (1D) Fourier inversion. This reduced *k*-space sampling is feasible because the pixels in the static region are solved only once with the assumption that they are identical throughout the entire image sequence. The sample selection is done by a heuristic sampling scheme. The need of an optimized sampling scheme has also been addressed.

Although the Shannon sampling theorem has been the principle behind sampling for many years, the idea of random sampling proposed by compressed sensing [103] has become a prevalent option for undersampling. It suggested that a signal can be perfectly recovered under certain conditions from severely undersampled measurements. These conditions include a sparse representation of the signal, random sampling, and incoherence. The sparsity constraint requires that a small number of elements in the signal are nonzero or the signal can have this kind of sparse representation after certain transformations such as total variation and wavelet transform, etc. In other words, the sparsity is known to be the characteristic for the signal, but the location of the sparsity is unknown. The random sampling and incoherence are the prerequisites on the implementation side for a perfect reconstruction.

For the need of undersampling in the techniques like Noquist, although cardiac images are sparse, the positions of the majority of the nonzero elements are known by separating dynamic region from the static. Consequently, random sampling may not be the optimal choice for sample selection. In fact, randomly selecting phase encoding lines in *k*-space has been claimed to be an ineffective sampling scheme in Noquist [99]. It was reported in Noquist that the heuristic sampling pattern yields better performance, even if it is combined with parallel imaging [104].

In the light of Noquist, we propose a rapid dynamic imaging technique named Noquist with arbitrary dynamic region (NADR). It makes three modifications to Noquist. First, sequential backward selection (SBS) is used to perform the sample selection instead of the heuristic sample selection schemes used in Noquist. Second, the dynamic region is allowed to be an arbitrary shape that encompasses the region of interest closely. This reduced dynamic region classifies more pixels into the static region which would be reconstructed only once for the entire image sequence. Therefore, ideally, it requires fewer phase encodings for reconstruction compared to the rectangular dynamic region across FOV used in Noquist. On the other hand, such an arbitrarily shaped dynamic region demands a two-dimensional (2D) undersampling in *k*-space and 2D Fourier inversion for the reconstruction of an image sequence. Third, the phase encoding direction is proposed to alternate horizontally and vertically at even and odd timeframes during a scan in order to provide more *k*-space coverage relative to keeping it constant for all timeframes.

This chapter is organized as follows. First, the framework of Noquist and the principle of SBS are overviewed. Second, the details of NADR are presented in Section 6.2. Third, the implementation issues including the image reconstruction, computation cost analysis, performance evaluation, and the stopping constraint of SBS elimination are discussed. Fourth, four experimental simulations are carried out to evaluate NADR: 1) comparing SBS and the heuristic sampling pattern within the framework of Noquist, 2) validating the developed stopping constraint of SBS elimination, 3) comparing NADR and Noquist with SBS, 4) comparing NADR with interleaved and non-interleaved sampling. The discussion and conclusion are presented at last.

6.1 Background

In this section, we review the basics of two existing techniques: Noquist for a faster dynamic cardiac MRI and sequential backward selection for sample selection.

6.1.1 Noquist Method

In a cardiac scout image of size *N*-by-*N*, the FOV is partitioned into a static region with *NS* lines that is assumed unchanged throughout the dynamic image sequence and a dynamic region with *ND* = *N*-*NS* lines that contain all pixels whose intensity values may change during the scan. With a vertical phase encoding direction, the dynamic region is typically *ND* rows across the central FOV that contains the heart. The profile of every vertical line in the image is the same, containing the same number of the static and dynamic pixels as illustrated in Figure 6.1. Therefore, the 2D image reconstruction problem can be decoupled into two 1D Fourier transforms. The raw *k*-space data is reconstructed along the frequency encoding direction by 1D fast Fourier transform (FFT). These halfway-reconstructed *k*-space data undergo the sampling selection: a subset of *N* phase encodings is selected at each timeframe for the reconstruction along the phase encoding direction. This sample selection is a 1D selection problem because choosing a measurement in *k*-space is equivalent to selecting the entire phase encoding line. And this selection is done by a heuristic sampling scheme.

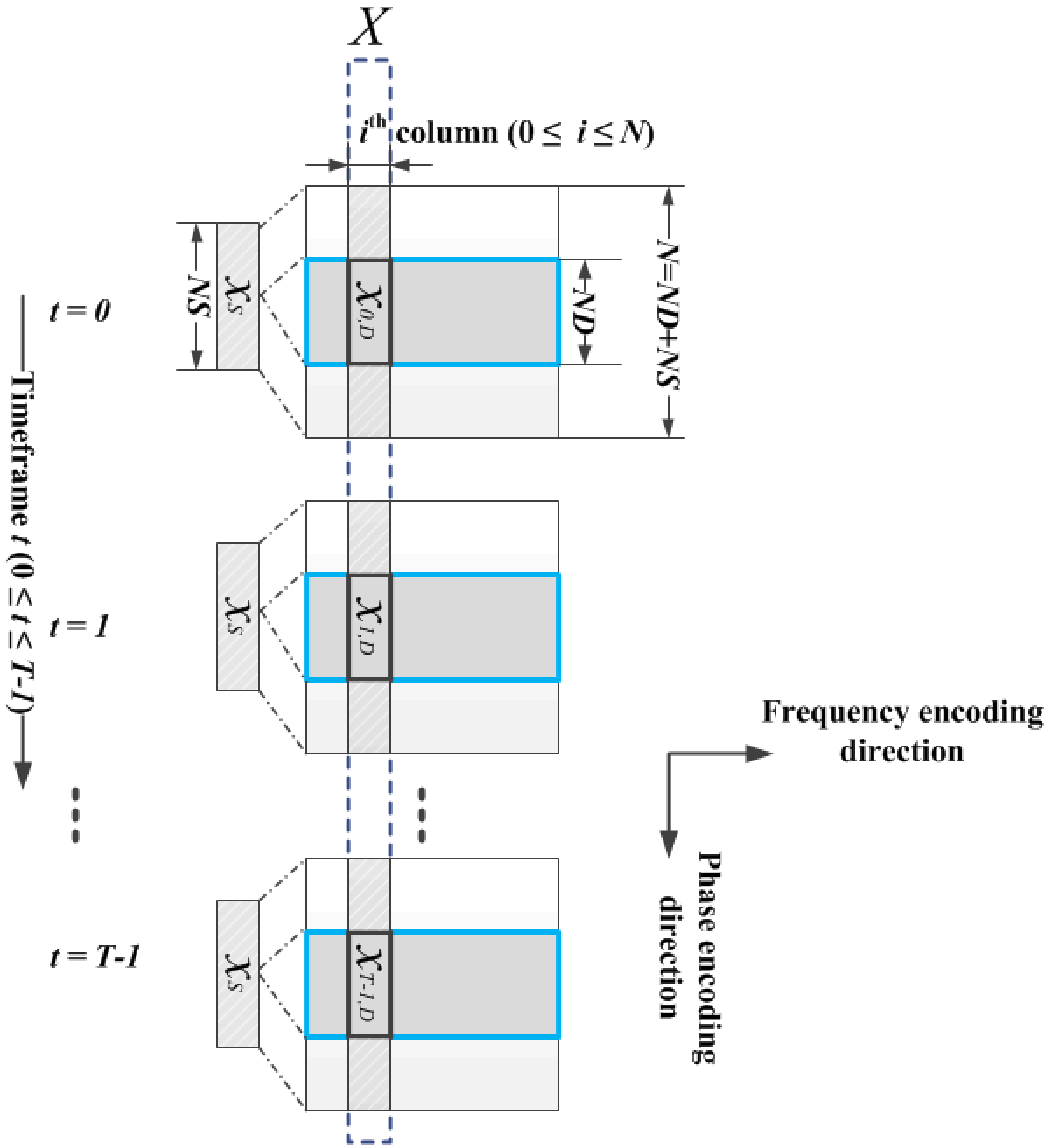

Figure 6.1 The diagram of the problem formulation in Noquist
(Assuming the phase and frequency encoding directions are along the image column and row directions respectively. *ND* rows of an image are defined as the dynamic region bounded in a blue rectangle. An i^{th} ($0 \leq i \leq T\text{-}1$) column of the image at timeframe t ($0 \leq t \leq T\text{-}1$) always contains *NS* static pixels X_S that are shared between all timeframes and *ND* dynamic pixels $X_{t,D}$. The dashed rectangle X contains the i^{th} column of the entire image sequence.)

Let F and Y denote the 1D DFT coefficients and the above-mentioned half-way reconstructed k-space measurements respectively. Let x_t denote the pixels at the i^{th} column of the image at a timeframe t $(0 \leq t \leq T-1)$, then the system can be represented as

$$y_t = Fx_t \tag{6.1}$$

In the conventional acquisition, the k-space data are acquired in the same fashion for all frames. If the i^{th} column of all T timeframes are concatenated into a vector X, the system equation $Y = AX$ has a structure as follows. The transformation matrix A is of size NT-by-NT.

$$\begin{bmatrix} y_0 \\ y_1 \\ \vdots \\ y_{T-1} \end{bmatrix} = \begin{bmatrix} F & 0 & \cdots & 0 \\ 0 & F & \cdots & 0 \\ \vdots & \vdots & \ddots & 0 \\ 0 & 0 & 0 & F \end{bmatrix} \begin{bmatrix} x_0 \\ x_1 \\ \vdots \\ x_{T-1} \end{bmatrix} \tag{6.2}$$

Let NS and ND denote the total number of static and dynamic lines across the FOV in the image domain respectively. Assuming the phase encoding is along the vertical direction, the $N\times N$ FOV becomes the sum of $NS\times N$ and $ND\times N$. For instance, for a 256-by-256 image, N is 256. If ND equals 100, then NS is 156.

Once the values of NS and ND are specified, the image at a time point can be sorted as

$$x_t = [x_{t,S}, x_{t,D}]^T \tag{6.3}$$

where superscript T stands for transposition. This partitioning can be applied on the 1D Fourier coefficients matrix F_t as

$$F_t = [F_{t,S}, F_{t,D}] \tag{6.4}$$

The size of $F_{t,S}$ amd $F_{t,D}$ is of N-by-NS and N-by-ND if all samples in k-space are taken. The static portion of each image is assumed to be identical and solved only once for the entire image sequence. The dynamic portion, however, has to be solved for each timeframe. Therefore, the system equation (6.2) is rewritten as

$$\begin{bmatrix} y_0 \\ y_1 \\ \vdots \\ y_{T-1} \end{bmatrix} = \underbrace{\begin{bmatrix} F_S & F_{0,D} & 0 & \cdots & 0 \\ F_S & 0 & F_{1,D} & \cdots & \vdots \\ \vdots & \vdots & \vdots & \ddots & 0 \\ F_S & 0 & \cdots & 0 & F_{T-1,D} \end{bmatrix}}_{A_{1D}} \begin{bmatrix} x_S \\ x_{0,D} \\ \vdots \\ x_{T-1,D} \end{bmatrix} \quad (6.5)$$

where y_t ($0 \le t \le T$-1) represents the above-mentioned half-way transformed *k*-space data. The total number of unknown phase encoding lines is calculated as

$$N_{unknown\_lines} = NS + ND \cdot T \quad (6.6)$$

To solve for these unknown lines, the number of lines to be acquired in *k*-space is calculated as

$$N_{linesToSample} = \frac{N_{unknown\_lines}}{T} = \frac{NS}{T} + ND \quad (6.7)$$

The size of $F_{t,S}$ and $F_{t,D}$ become $N_{linesToSample}$-by-NS and $N_{linesToSample}$-by-ND respectively. The 1D Fourier coefficient matrix A_{1D} is of size $N_{unknown\_lines}$-by-$N_{unknown\_lines}$. This linear system is solved in seconds by the conjugate gradient method.

To reduce the number of rows of $F_{t,S}$ and $F_{t,D}$ from N to $N_{linesToSample}$, the heuristic sampling pattern in Noquist is designed as follows. All even *k*-space lines are acquired in every frame, and odd *k*-space lines in the interlaced evenly spaced patterns [99]. With this heuristic sampling scheme, each phase encoding in *k*-space is sampled at least once, which is a necessary condition for a nonsingular modeling matrix A_{1D}.

6.1.2 Sequential Backward Selection

The motivation for reordering the linear system (6.2) to the form in (6.5) is to observe $N_{linesToSample} \le NT$ elements of Y that provide the best possible reconstruction of X. The challenge of this undersampling problem is to determine the best combination of observations before acquisition. The sequential backward selection algorithm [105] has been proposed for observation selection with the presence of noise. The selection is made by utilizing only the information of the transformation matrix A. This section presents a review of the SBS algorithm.

Let $Y = AX + u$ denote the linear system for reconstructing a good estimate of X given the observed signal Y in the presence of independent Gaussian noise u with mean of zero and unit variance, where

$A \epsilon \mathbb{C}^{m \times n}$ and $m \geq n$. If the reconstruction of *X* is solved as the least-squares problem, $min\|\widehat{X} - X\|^2$, the estimate $\hat{X}$ can be written as

$$\begin{aligned} \hat{X} &= (A^H A)^{-1} A^H Y \\ &= (A^H A)^{-1} A^H (AX + u) \\ &= X + (A^H A)^{-1} A^H u \end{aligned} \qquad (6.8)$$

The expectation of the least-squares error is

$$\begin{aligned} E\left[\left\|\hat{X} - X\right\|^2\right] &= E\left[\left\|(A^H A)^{-1} A^H u\right\|^2\right] \\ &= E\left[u^H A(A^H A)^{-1}(A^H A)^{-1} A^H u\right] \\ &= tr\{A(A^H A)^{-2} A^H\} \end{aligned} \qquad (6.9)$$

Based on the property that $tr\{BCD\} = tr\{DCB\}$, Equation (6.9) can be rewritten as

$$E\left[\left\|\hat{X} - X\right\|^2\right] = tr\{(A^H A)^{-1}\} \qquad (6.10)$$

The problem is to observe *k* from *m* elements of *y* that provide the best possible reconstruction of *X* using only the information from the *A* matrix to select samples. The SBS starts with this *A* matrix, and sequentially eliminates the least important row of *A* at each step until the desired number of rows remain. Let a_i ($i \leq m$) represent the i^{th} row of the matrix *A*. If a_i is eliminated from *A*, the modified inverse matrix $(\tilde{A}^H \tilde{A} + K)^{-1}$ is given by the Sherman-Morrison matrix inversion formula [106] as

$$(\tilde{A}^H \tilde{A} + K)^{-1} = (A^H A + K)^{-1} + \frac{(A^H A + K)^{-1} a_i^H a_i (A^H A + K)^{-1}}{1 - a_i (A^H A + K)^{-1} a_i^H} \qquad (6.11)$$

The superimposed *H* denotes Hermitian transpose. The Hermitian and non-negative definite matrix *K* may cover a pre-selected subset of observations or represent reconstruction with a Wiener filter [105]. It is set to zero for simplification. Taking the trace of Equation (6.11) yields

$$tr\left\{(\tilde{A}^H \tilde{A})^{-1}\right\} = tr\left\{(A^H A)^{-1}\right\} + \frac{a_i (A^H A)^{-1} (A^H A)^{-1} a_i^H}{1 - a_i (A^H A)^{-1} a_i^H} \qquad (6.12)$$

Therefore, the criterion for single row elimination at each step is to choose the i^{th} row that minimized

$$C_i = \frac{a_i (A^H A)^{-2} a_i^H}{1 - a_i (A^H A)^{-1} a_i^H} \qquad (6.13)$$

If the transformation matrix A is too large to be stored, a linear system has to be solved in order to compute $(A^H A)^{-1} a_i$ for each row of the transformation matrix without matrix storage. A recursive method has been proposed [105] to compute the quantities $a_j (A^H A)^{-1} a_j^H$ and $a_j (A^H A)^{-2} a_j^H$ where j denotes the remaining rows of A after an elimination. These two quantities are given as

$$a_j (\tilde{A}^H \tilde{A})^{-1} a_j^H = a_j (A^H A)^{-1} a_j^H + \sigma_i a_j (A^H A)^{-1} a_i^H a_i (A^H A)^{-1} a_j^H \qquad (6.14)$$

$$\begin{aligned} a_j (\tilde{A}^H \tilde{A})^{-2} a_j^H &= a_j (A^H A)^{-2} a_j^H + 2\sigma_i \operatorname{Re}\left\{ a_j (A^H A)^{-2} a_i^H a_i (A^H A)^{-1} a_j^H \right\} \\ &\quad + \sigma_i^2 a_j (A^H A)^{-1} a_i^H a_i (\tilde{A}^H \tilde{A})^{-2} a_i^H a_i (A^H A)^{-1} a_j^H \end{aligned} \qquad (6.15)$$

where $\sigma_i = 1 / (1 - a_i (A^H A)^{-1} a_i^H)$. The vectors $v_i = (A^H A)^{-1} a_i^H$ and $w_i = (A^H A)^{-2} a_i^H$ have to be available in order to compute those two quantities in (6.14) and (6.15). v_i is solved by minimizing

$$\phi(v_i) = \left\| e_i - A v_i \right\|^2 \qquad (6.16)$$

with e_i being the i^{th} column of an m-by-m identity matrix. w_i is updated by minimizing

$$\phi(w_i) = \left\| v_i - A^H A w_i \right\|^2 \qquad (6.17)$$

with respect to w_i. This no-matrix-storage strategy requires two conjugate gradient solutions per elimination step.

6.2 Noquist with Arbitrary Dynamic Region (NADR)

The idea behind Noquist is to sacrifice the accuracy in the predefined static region at all timeframes for a reduction in the image acquisition by reconstructing those static pixels once for the entire image sequence. Our work originates from the observation that the dynamic region could be redefined to achieve a further reduction in the acquisition by classifying more pixels into the static region.

In NADR, the dynamic region is designed to be an arbitrary shape that surrounds the ROI more compactly than it does in Noquist. Such an arbitrarily shaped dynamic region demands 2D undersampling and 2D reconstruction. 2D undersampling makes it possible to select individual measurements in *k*-space. With the restriction that a phase encoding line has to be sampled in a single group, SBS is customized to eliminate multiple rows of the transformation matrix at each iteration.

The rest of this section is organized as follows. In Section 6.2.1, the arbitrarily-shaped dynamic region is introduced. In Section 6.2.2, we develop a modified version of SBS to eliminate samples along an entire phase encoding line as a single group. The theoretical limit on the imaging time reduction is derived in Section 6.2.3. The idea of interleaved sampling is illustrated in Section 6.2.4.

6.2.1 An Arbitrarily Shaped Dynamic Region

In cardiac MRI, the heart is located around the center of the FOV, and typically occupies only ~10% of the FOV. Ideally, it is the only part of the image that moves. The surrounding tissues of the heart are imaged to avoid aliasing and wraparound artifacts. An arbitrary dynamic region is proposed to classify much fewer dynamic pixels than the dynamic stripe in Noquist. Recall that the static pixels are identical from one timeframe to another. Only the dynamic pixels need to be reconstructed at every timeframe. The image acquisition with a refined, smaller dynamic region is potentially faster than Noquist because fewer unknowns are needed for reconstruction.

A typical mid-ventricular short-axis cardiac image is used to visualize the differences of the dynamic region between Noquist and NADR. Figure 6.2 illustrates the dynamic region (the blue rectangular stripe across the FOV) that is just enough to cover the ROI in Noquist assuming vertical phase encoding direction. Their dynamic region could be a horizontal or vertical stripe across the FOV depending on the phase encoding direction. The proposed arbitrarily shaped dynamic region (the B-spline contour in red) in Figure 6.2 encompasses the ROI more closely. In Noquist, the pixels in the blue stripe would be reconstructed for each timeframe; whereas in NADR, only the pixels inside the red B-spline contour would be reconstructed at each timeframe. Obviously, NADR has fewer pixels to reconstruct than

Noquist does. In fact, the difference in the number of unknowns between NADR and Noquist gets bigger if the ROI takes a smaller portion of the FOV.

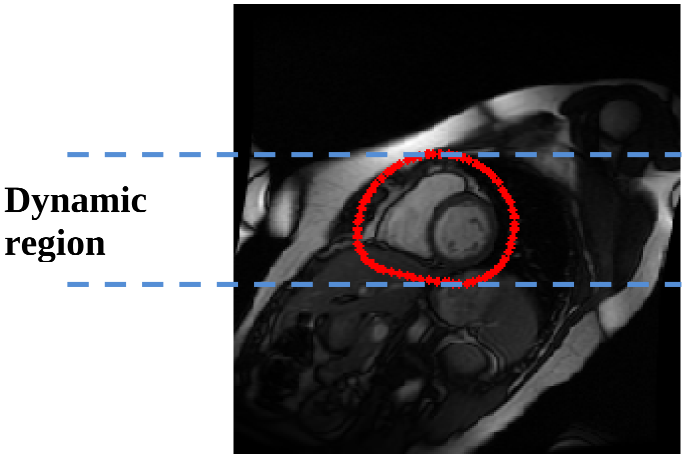

Figure 6.2 Comparison of the dynamic region between Noquist and NADR
(For a 256×256×20 image sequence, the dynamic region used in Noquist is a rectangular stripe across the FOV (in between two blue dashed lines); the proposed dynamic region has an arbitrary shape (red B-spline curve))

In general, there is no restriction on the shape of the proposed dynamic region. The arbitrary shape can be either convex or concave. Moreover, it can contain several isolated selected regions. In an extreme case, it can be a set of individually selected pixels.

With the proposed dynamic region, the 2D undersampling and 2D reconstruction must be performed to solve for individual pixels in the image domain, because the line profile along the phase encoding direction as shown in Figure 6.2 changes from line to line. In the example displayed in Figure 6.2, the vertical line profile is strictly the same: static, dynamic, and then static pixels when the dynamic region is selected as the blue stripe across the FOV. With an arbitrarily-shaped dynamic region, the vertical line profile contains two types: one includes purely static pixels; the other is a mixture of static and dynamic pixels. Consequently, the image sequence cannot be easily reconstructed by 1D Fourier inversion as in Noquist.

There is a tradeoff between the flexibility on shaping the dynamic region and the complexity of the consequent undersampling and reconstruction. With 2D undersampling and 2D reconstruction, each pixel can be selected independently from another. Theoretically, it is possible to select individual measurements from *k*-*t* space. However, selecting individual *k*-*t* space measurements does not decrease the acquisition time because the entire phase encoding lines would be acquired regardless. With the dynamic region in an arbitrary shape, the minimal number of phase encodings may be reduced; however, all the unknowns have to be reconstructed simultaneously by 2D Fourier inversion. The associated computational complexity increases dramatically. The details about computation analysis are presented in Section 6.3.2. The problem of 2D reconstruction is addressed in Section 6.3.1.

6.2.2 Modified Sequential Backward Selection

A critical factor in the 2D undersampling and reconstruction approach is how to select *k*-space samples. The heuristic sampling scheme proposed in Noquist is not applicable to the 2D sample selection. In this section, we modify SBS in two ways to support 2D sample selection with an arbitrarily-shaped dynamic region. First in Section 6.2.2.1, we modify SBS to eliminate all samples in a phase encoding line together in a group. Then in Section 6.2.2.2, we modify SBS to only consider the reconstruction error in the dynamic region.

6.2.2.1 Multi-row eliminations

Let A_{2D} denote the transformation matrix for the 2D undersampling and reconstruction system. The system equation becomes $Y = A_{2D}X$. In MRI, the acquisition time is proportional to the number of phase encoding lines that are acquired. Removing samples in the read direction does not reduce scan time. In NADR, the phase encoding lines are either rows or columns in *k*-space; while each row of the transformation matrix A_{2D} represents a single measurement in *k*-*t* space. Therefore, the SBS algorithm is customized to simultaneously eliminate multiple rows of the A_{2D} matrix that represents an entire phase encoding line in *k*-space.

For the 2D sample selection problem, the 2D DFT coefficient matrix for an image needs to be permuted, then partitioned and stored into the proper locations of the A_{2D} matrix. Let ND_p and NS_p denote the total number of pixels in the dynamic and static regions respectively. The permutation step is to arrange all the pixels into a sorted order such that all NS_p pixels from static region are followed by the

ND_p pixels in the dynamic region per timeframe. The permuted 2D DFT matrix F is then partitioned into F_S of size NS_p-by-$N^2$and F_D of size ND_p-by-N^2. The F_S and F_D are then filled in A_{2D} as shown in Equation (6.5).

Once the A_{2D} matrix is formulated, SBS is customized to eliminate N rows of A_{2D} at a time. These N rows match up with a length-N phase encoding line in k-t space. Let A_r denote a set of rows to be eliminated from A_{2D} at an iteration. We have

$$A_{2D}{}^H A_{2D} = \tilde{A}_{2D}{}^H \tilde{A}_{2D} + A_r{}^H A_r \tag{6.18}$$

By Sherman-Morrison formula, we get

$$(\tilde{A}_{2D}{}^H \tilde{A}_{2D})^{-1} = (A_{2D}{}^H A_{2D})^{-1} + \frac{(A_{2D}{}^H A_{2D})^{-1} A_r{}^H A_r (A_{2D}{}^H A_{2D})^{-1}}{1 - A_r (A_{2D}{}^H A_{2D})^{-1} A_r{}^H} \tag{6.19}$$

Taking the trace of both sides of (6.21) yields

$$tr\{(\tilde{A}_{2D}{}^H \tilde{A}_{2D})^{-1}\} = tr\{(A_{2D}{}^H A_{2D})^{-1}\} + tr\left\{\frac{A_r (A_{2D}{}^H A_{2D})^{-2} A_r{}^H}{1 - A_r (A_{2D}{}^H A_{2D})^{-1} A_r{}^H}\right\} \tag{6.20}$$

The cost function to be minimized is

$$C_i^{'} = tr\left\{\frac{A_{r_i}\left(A_{2D}^H A_{2D}\right)^{-2} A_{r_i}^H}{I - A_{r_i}\left(A_{2D}^H A_{2D}\right)^{-1} A_{r_i}^H}\right\} \tag{6.21}$$

where I is the identity matrix of size N-by-N.

To implement the multi-row elimination, a candidate matrix is constructed. Each row of the candidate matrix contains a list of row indices of A_{2D} that corresponds to all the measurements in a phase encoding line. Specifically for cardiac image sequence, a horizontal line in k-space corresponds to a set of measurement indices equally spaced by N; while a vertical line corresponds to a set of N consecutive measurement indices. The total number of rows in this candidate matrix equals to the number of possible elimination sets NT.

6.2.2.2 Minimizing errors within the dynamic region only

The original SBS was designed to select the optimal set of samples for the best possible image reconstruction of *X*, while our goal is to offer the best possible reconstruction inside the dynamic region. Consequently, the cost function for multi-row elimination given by the Equation (6.21) is revised to minimize only the errors in the dynamic region.

Let *SS* be a diagonal matrix with ones at the locations of the dynamic pixels and zeros otherwise. The size of the *SS* matrix is $N_{total\_unknowns}$-by-$N_{total\_unknowns}$. Let X_D denote the reconstruction vector *X* with nonzero values only at the dynamic pixels $X_D = SS \cdot X$. Similar to the Equation (6.8), the estimate $\hat{X}_D$ becomes $\hat{X}_D = X_D + (A_{2D}^H A_{2D})^{-1} A_{2D}^H \cdot SS \cdot u$.

Evaluating the least-squares error in the dynamic region yields

$$\begin{aligned} E\left[\left\|\hat{X}_D - X_D\right\|^2\right] &= E\left[\left\|(A_{2D}^H A_{2D})^{-1} A_{2D}^H \cdot SS \cdot u\right\|^2\right] \\ &= E\left[u^H A_{2D}(A_{2D}^H A_{2D})^{-1} \cdot SS(A_{2D}^H A_{2D})^{-1} A_{2D}^H \cdot u\right] \\ &= tr\left\{(A_{2D}^H A_{2D})^{-1}\right\} \cdot SS. \end{aligned} \tag{6.22}$$

Subsequently, the cost function C_i' is modified to select samples from *k*-*t* space for the best possible reconstruction inside the dynamic region as

$$C_i' = tr\left\{\frac{A_{r_i}\left(A_{2D}^H A_{2D}\right)^{-2} \cdot SS \cdot A_{r_i}^H}{I - A_{r_i}\left(A_{2D}^H A_{2D}\right)^{-1} A_{r_i}^H}\right\}. \tag{6.23}$$

Recall the no-matrix-storage strategy discussed in Section 6.1.2, the quantities $a_j(A^H A)^{-1} a_j^H$ and $a_j(A^H A)^{-2} a_j^H$ given in the equations (6.14) and (6.15) are recursively updated in order to evaluate the C_i' values. These two quantities are modified for the SBS multi-row elimination with errors minimized in the dynamic region. Let A_{r_j} denote one of the (N^2T-j) remaining candidates for elimination, we have

$$A_{r_j}(\tilde{A}_{2D}^H \tilde{A}_{2D})^{-1} A_{r_j}^H = AA_{r_j} \cdot (A_{2D}^H A_{2D})^{-1} AA_{r_j}^H + \sigma_i \left|A_{r_j} v_i v_i^H A_{2D} A_{r_j}^H\right| \tag{6.24}$$

$$\begin{aligned} A_{r_j}(\tilde{A}_{2D}^H \tilde{A}_{2D})^{-2} A_{r_j}^H &= AA_{r_j}(A_{2D}^H A_{2D})^{-2} A_{r_j}^H + 2\sigma_i \operatorname{Re}\left\{(A_{r_j} w_i)(v_i^H AA_{r_j}^H)\right\} \\ &\quad + \sigma_i^2 \left|A_{r_j} v_i v_i^H AA_{r_j}^H\right| \cdot (A_{r_i} w_i) \end{aligned} \tag{6.25}$$

where $AA_{r_j} = A_{r_j} \cdot SS$, and $\sigma_i = 1/(I - A_{r_i}(A_{2D}^H A_{2D})^{-1} A_{r_i}^H)$.

6.2.3 Theoretical Limit on Imaging Time Reduction

In this section, a theoretical limit is derived for the percentage of reduction in scan time resulting from an arbitrarily-shaped region of interest. In NADR, the linear system used to solve for the whole image sequence shares the same structure of the A matrix in Equation (6.5). We continue to use the notation from Section 6.1.1. The Fourier matrix F becomes 2D DFT coefficient matrix with permutation. AndThe permutation sorts the vectorized image vector in the way that all static pixels are located in the front and followed by dynamic pixels at different timeframes.

The total number of unknowns in the linear system $Y = A_{2D}X$ is calculated as

$$N_{total\_unknowns} = ND_p \cdot T + NS_p \tag{6.26}$$

where ND_p and NS_p denote the total number of dynamic and static pixels respectively in an N-by-N image.

For 2D reconstruction, each row of A_{2D} corresponds to a single point on a phase encoding line in k-t space. In other words, one phase encoding line maps to N rows of A_{2D}. Hence, the number of k-t space measurements we have to acquire is

$$N_{kt\_measurenents} = \frac{N_{total\_unknowns}}{T} = ND_p + NS_p/T \tag{6.27}$$

Assuming these $N_{kt\_measurements}$ k-t space measurements are taken as a multiple of k-t space lines, $N_{linesToSample}$, with a lower bound,

$$N_{linesToSample} \geq \frac{N_{kt\_measurements}}{N} = \frac{ND_p + NS_p/T}{N} \tag{6.28}$$

For an image sequence that contains 20 timeframes and each image is of size 256-by-256, if the dynamic region is bounded in the rectangle that contains 66 rows and 86 columns, where the total number of dynamic pixels is summed to 5676, the total number of k-space lines needed to sample is ideally 680 according to Equation (6.20), 86.72% data reduction; whereas Noquist requires 1520 lines to be sampled according to Equation (6.6), 70.3% data reduction. In theory, NADR can be at most 15% faster than the Noquist in this case.

6.2.4 Interleaved Sampling

The phase encoding direction can be defined as either the image row or image column direction. We propose to alternate the phase encoding direction at even and odd timeframes as illustrated in Figure 6.3. Consequently, the lines to be sampled will then contain pixels in a row or consecutive pixels in a column at even and odd timeframes respectively. In such a way, the sampled *k*-*t* space data preserve a greater variation in terms of the sampled locations in *k*-space at different timeframes and can potentially allow a greater number of phase encoding lines to be eliminated. This interleaved phase encoding strategy does not affect the theoretical limit on the imaging time reduction derived in the Section 6.2.3.

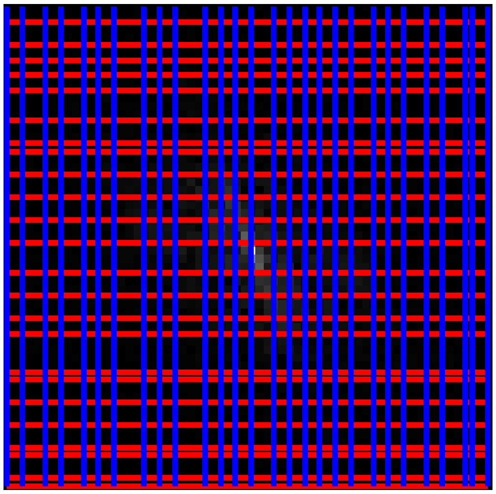

Figure 6.3 Illustration of the interleaved phase encoding sampling
(Horizontal in red at even timeframes; vertical in blue at odd timeframes**)**

In a nutshell, NADR refines the dynamic region as an arbitrary shape enclosing the heart compactly, customizes the SBS algorithm to perform the 2D undersampling in the *k*-*t* space, and reconstructs all unknown pixels of the entire image sequence together by a direct 2D Fourier inversion.

6.3 Implementation Issues

In this section, four aspects of the implementation issues are addressed: 1) image reconstruction after the sample selection is made, 2) the computational complexity for both 2D undersampling and 2D reconstruction, 3) the metric for evaluating the accuracy of reconstruction, and 4) the stopping criterion for SBS elimination.

6.3.1 Image Reconstruction

The system equation given by (6.5) illustrates the linear equation to reconstruct the image sequence for both Noquist and NADR. However, for NADR, the meaning of each term in (6.5) is different. In the following discussion, it is assumed that the phase encoding direction is the image column direction and the frequency encoding direction is the image row direction. The phase and frequency encoding directions can be swapped without loss of generality.

In Noquist, the Equation (6.5) represents the reconstruction of the unknowns in the i^{th} column of the image sequence (Figure 6.1). To reconstruct the image sequence, Equation (6.5) needs to be solved N times where N denotes the number of columns in an image. The vector, $[x_s, x_{0,D}, \ldots x_{T-1,D}]^T$, represents the unknown pixels of the i^{th} column of the image sequence. The reconstruction in the frequency encoding direction is performed by 1D FFT. This half-way reconstructed data in k-t space is then sampled to obtain the vector, y_t ($0 \le t \le T$-1), on the left hand side of Equation (6.5). The reconstruction along the phase encoding direction is then performed by solving Equation (6.5) to reconstruct the concatenated image sequence columnwise.

In NADR, Equation (6.5) is solved once for all the unknowns of the entire image sequence. The vector, $[x_s, x_{0,D}, \ldots x_{T-1,D}]^T$, denotes all the unknowns of the image sequence, and y_t ($0 \le t \le T$-1) represents the sampled k-space raw data. The A_{2D} matrix is the sampled transformation matrix that contains 2D DFT coefficients.

Note that the A_{2D} matrix depends only on the dynamic region and SBS sample selection process and can be constructed prior to data acquisition. Once data has been acquired, $Y=A_{2D}X$ is solved by conjugate gradient least squares (CGLS) method.

6.3.2 Computational Complexity

The computational complexity of NADR is much higher than Noquist. The detailed analysis is discussed as follows. First, 2D undersampling is more demanding in both memory and computational cost than 1D undersampling due to an increased size of the transformation matrix. Second, reconstructing the unknowns of the whole image sequence simultaneously takes longer than reconstructing each column of the image sequence independently.

The switch from 1D undersampling to 2D undersampling increases the computational complexity tremendously. For an image sequence of size N-by-N-by-T, the 1D DFT coefficient matrix is N-by-N and A_{1D} is of size NT-by-$N_{unknown\_lines}$; while the non-sparse 2D DFT coefficient matrix is N^2-by-N^2 and A_{2D} is of size N^2T-by-$N_{total\_unknowns}$. When N is small so that A_{2D} can be saved in the memory, the modified SBS with multi-row elimination will be carried out for the sample selection. When N is large and A_{2D} cannot be saved, the no-matrix-storage strategy discussed in Section 6.2.2.2 will be applied instead.

Recall that the no-matrix-storage SBS is a recursive method. It takes longer to perform the sample selection than the modified SBS with A_{2D} stored because the quantities (6.14) and (6.15) need to be computed by CGLS before the remaining rows of A_{2D} could be updated in order to evaluate the C_i' values at each iteration. Instead of calculating the matrix inverse, $(A_{2D}^H A_{2D})^{-1}$, we use 2D FFT to compute the quantity $(A_{2D}^H A_{2D})^{-1} A_{r_j}^H$ and $(A_{2D}^H A_{2D})^{-2} A_{r_j}^H$.

The change from 1D reconstruction to 2D reconstruction also demands more computation. 1D reconstruction from undersampled A_{1D} matrix requires $C_{nq} = N(ND \cdot T + NS)^2 + TNlog_2N$ complex operations; 2D reconstruction from undersampled A_{2D} matrix needs $C = (ND_p \cdot T + NS_p)^2$ complex operations for the reconstruction. For realistic dimensions such as N=256, T=20, with a rectangular dynamic region bounded by 66 rows and 86 columns, 1D reconstruction in Noquist requires 58 million complex floating-point operations. 2D reconstruction in NADR requires 3 billion operations, or a factor of 51 times more.

6.3.3 Performance Evaluation

The aim of NADR is to achieve the same level of reconstruction accuracy compared to Noquist by acquiring less phase encodings from *k-t* space. Noquist has demonstrated the consistency and reliability in image reconstruction from undersampled *k-t* space measurements. Thus, we target at a further reduction in the number of phase encodings for a comparable reconstruction quality.

To evaluate the reconstruction quality, the normalized root mean square error (NRMSE) is defined as

$$NRMSE = \frac{\left\|\hat{X} - X\right\|}{\|X\|} \times 100\% \tag{6.29}$$

where $\hat{X}$ is the vectorized reconstructed image and X is the vectorized original image. This NRMSE in percent is used to compare the reconstruction errors inside the smaller dynamic region defined in NADR compared to Noquist.

6.3.4 Stopping Criterion of SBS Elimination

In SBS algorithm, the selection criterion eliminates row(s) that yields the minimal C_i' values. There is no constraint on the row elimination until the desired number of rows is reached. However, the minimal C_i' value increases monotically as rows are removed from the transformation matrix [105]. Also, as rows are removed from the transformation matrix, the condition number of the transformation matrix increases. However, the exact relationship between minimal C_i' and the condition number is not known. Therefore, it is not reliable to predict the condition number of the transformation matrix by tracking the minimal C_i' values as the elimination progresses.

We propose to use a training set of image sequences to empirically determine the maximum number of rows to eliminate in the SBS algorithm. The derivation of the stopping criterion is illustrated by the experiment with following settings. A set consisted of 40 cardiac image sequences as the training set. For each image sequence, the original images of size 256-by-256 are resized down to 64-by-64 using bicubic interpolation. The first five odd-numbered timeframes of the original image sequences are used to generate the 64-by-64-by-5 image sequences. The interleaved sampling was applied. And the sample selection was performed by the SBS with no-matrix-storage implementation. In SBS elimination, the errors were minimized in the dynamic region as derived in Section 6.2.2.2.

The NRMSE in the dynamic region is plotted against the number of eliminations in Figure 6.4. The error bars represent the standard deviation of NRMSE. The average NRMSE stayed below 10% for the first 188 eliminations and suddenly jumped to 28% after189 rows are eliminated. From 175 to 188 eliminations, NRMSE was around 5% steadily. Therefore, we conclude the SBS elimination should stop after 180 rows were eliminated. The reconstructed and difference images corresponding to 2.7%, 6.4%, and 25.3% NRMSE are displayed in Figure 6.5. The colored difference images display the reconstruction error as the percentage of mean intensity value of the original image. Note that the color-coded difference images amplify the residuals for visualization. If the difference images are plotted together with the original and reconstructed images in grayscale, the differences are barely noticeable for 6.4% NRMSE. We consider a NRMSE less than 10% as subtle differences between the reconstruction and the original image and conclude that the SBS algorithm should terminate after 180 rows have been eliminated for this example.

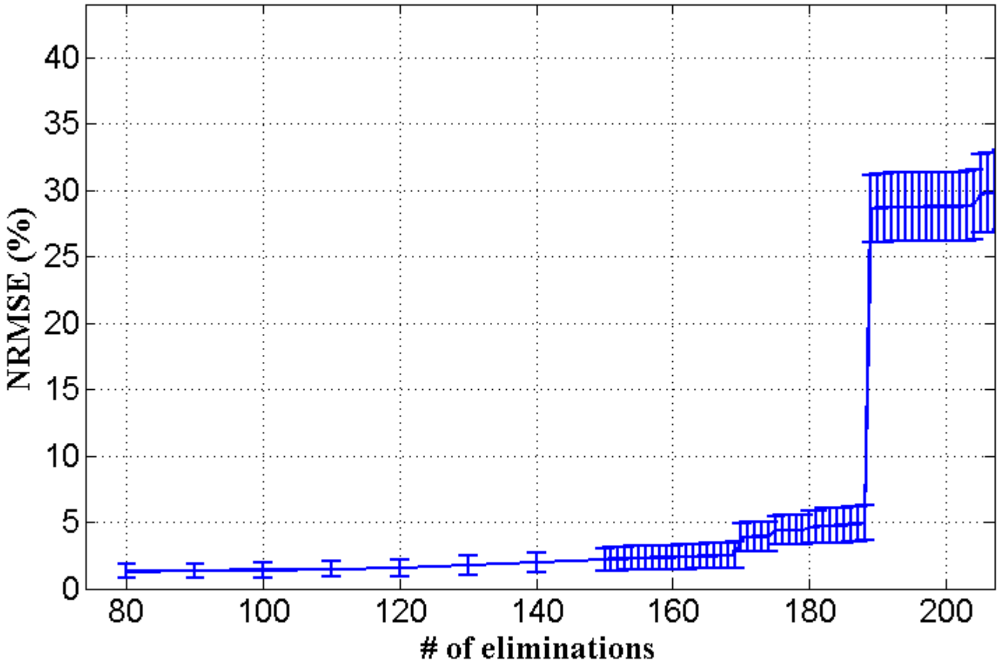

Figure 6.4 Measured NRMSE with error bars vs. the number of SBS eliminations for NADR with interleaved sampling
(The NRMSE inside the dynamic region is averaged over 40 64×64×5 resized cardiac image sequences with the error bars representing the standard deviation.)

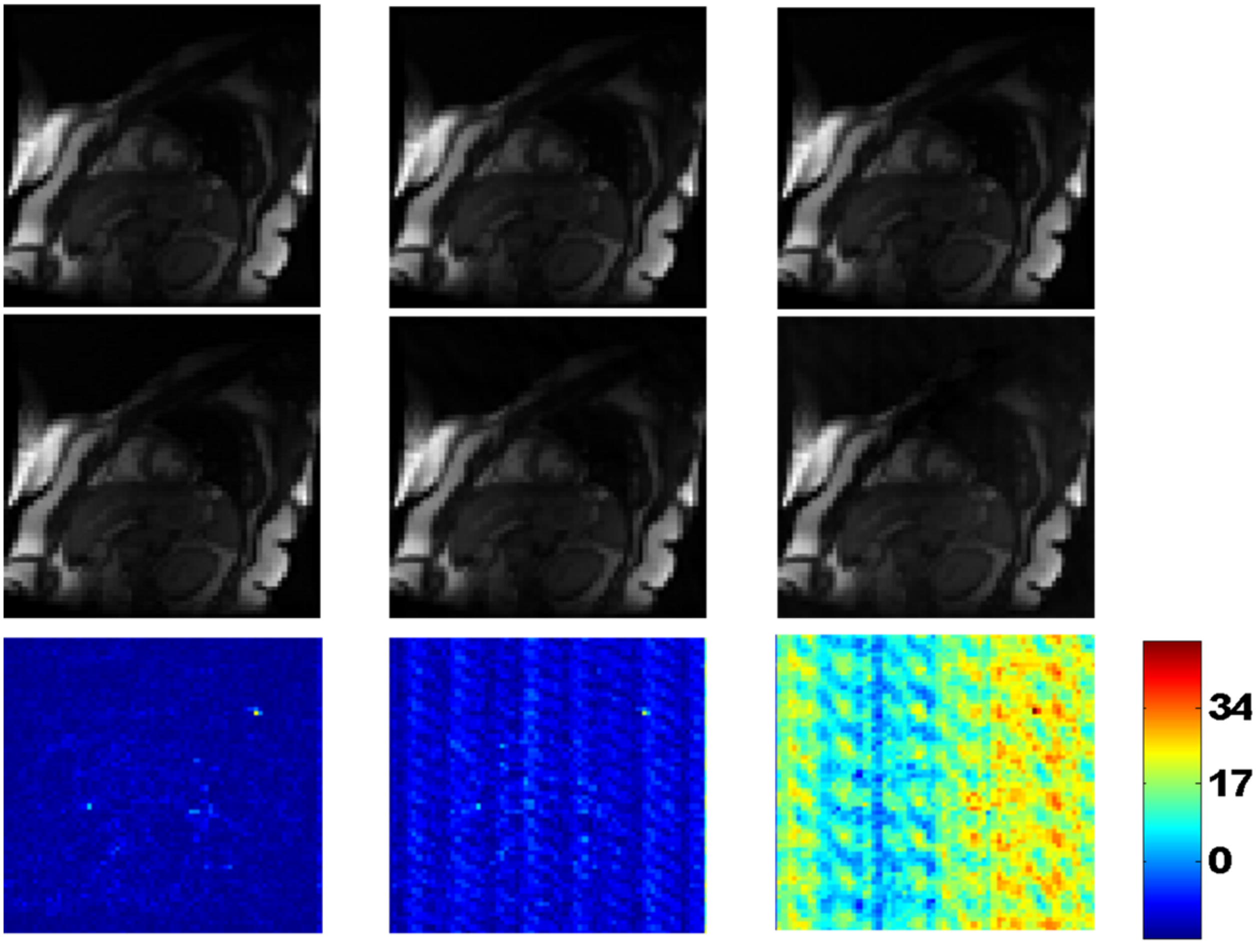

Figure 6.5 Randomly-selected reconstructed images by NADR for various NRMSE (Images for top to bottom: original, reconstructed, difference images in grayscale and colored difference image; image stack from left to right: 2.7%, 6.4%, 25.3% NRMSE.)

6.4 Simulation Results

We performed four experiments to demonstrate and evaluate the feasibility and performance of NADR. In the first experiment, the performance of Noquist with SBS sample selection was compared with Noquist with heuristic sample selection. Second, the proposed stopping criterion of SBS elimination was validated using a set of image data not used for training. Third, NADR is compared against the Noquist with SBS. The last experiment compared NADR with interleaved and non-interleaved phase encoding direction.

All experiments in this section used a data set consisting of 40 mid-ventricular short-axis cardiac MR image sequences not used for training set. These sequences consist of data from patients with 7 different heart conditions including myocardial infarction, mitral regurgitation, normal volunteer, marathon runner, volume overload, diabetes, and hypertension. These sequences were randomly selected from a large collection of MRI datasets acquired in another research project. And their phase encoding direction is along the image column direction.

6.4.1 Comparison of Heuristic Sampling Pattern and SBS

In this experiment, we compared the performance of Noquist with SBS sample selection with Noquist with heuristic sample selection. The goal of this experiment is to investigate the effectiveness of SBS relative to heuristic sample selection.

Experimental Setting

40 full-sized 256×256×20 mid-ventricular short-axis cardiac MR image sequences are used for testing. Each image sequence contains 20 timeframes over a cardiac cycle. Figure 6.6 displays an image sequence. The full *k*-space data were simulated as the Fourier transform of the magnitude image data.

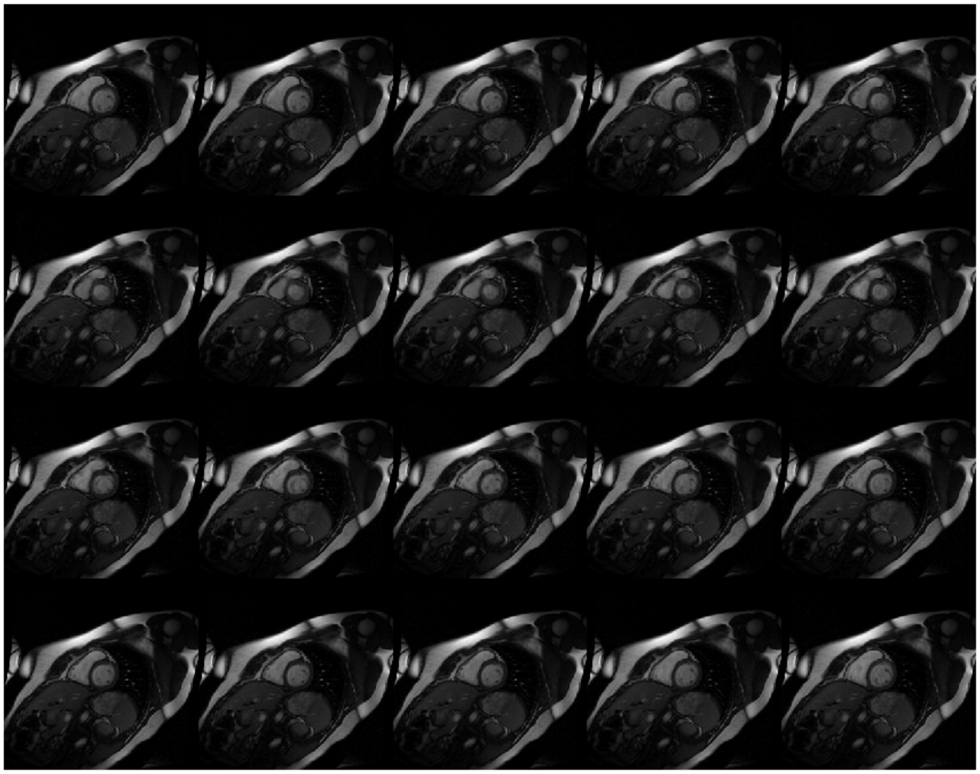

Figure 6.6 A full-sized cardiac image sequence
(An original 256×256×20 cardiac image sequence: timeframe indices increase from left to right and top to bottom)

To implement the heuristic sampling pattern described in Noquist [99], the dynamic region was designed to take 50% of the entire FOV so that each phase encoding in *k*-space could be sampled at least once. It was marked from the 64th to 191th row of an image such that *ND* = 128 for each timeframe as illustrated in Figure 6.7. According to Equation (6.7), the number of lines to be acquired per timeframe is $N_{linesTOSample} = ND + NS/T = 135$.

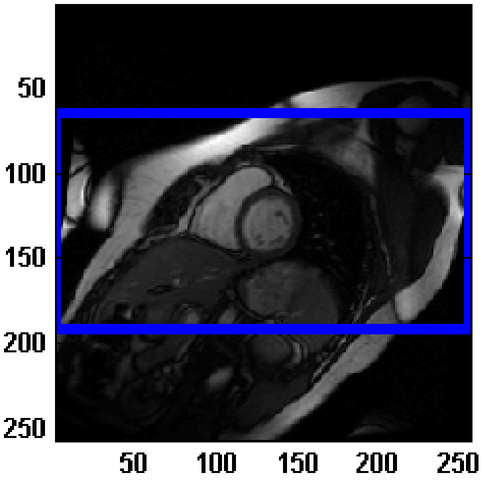

Figure 6.7 The dynamic region in Noquist

The Sampling Patterns

In this specific case, the heuristic sampling pattern is generated as follows. All even lines were taken. This took up to 128 *k*-space lines. In addition, 7 consecutive odd *k*-space lines were sampled. For instance, in timeframe 1, 128 even lines and the 1st, 3rd, 5th, 7th, 9th, 11th, and 13th lines were sampled. In timeframe 2, 128 even lines plus the 15th, 17th, 19th, 21st, 23rd, 25th and 27th lines were sampled. When the last odd line in *k*-space was reached, the count of odd lines restarted from the first line. Figure 6.8a depicts the sampled locations in *k*-space at each timeframe. A blue line indicates that the corresponding phase encoding has been sampled; while a blank line represents a skipped phase encoding. A block of blue lines indicates the consecutively sampled phase encodings.

Figure 6.8b shows the sampling pattern in *k-t* space by SBS. Similar to the heuristic sampling pattern, all even phase encodings were picked by SBS at each frame. Some odd phase encodings were sampled in a scattered pattern at different timeframes.

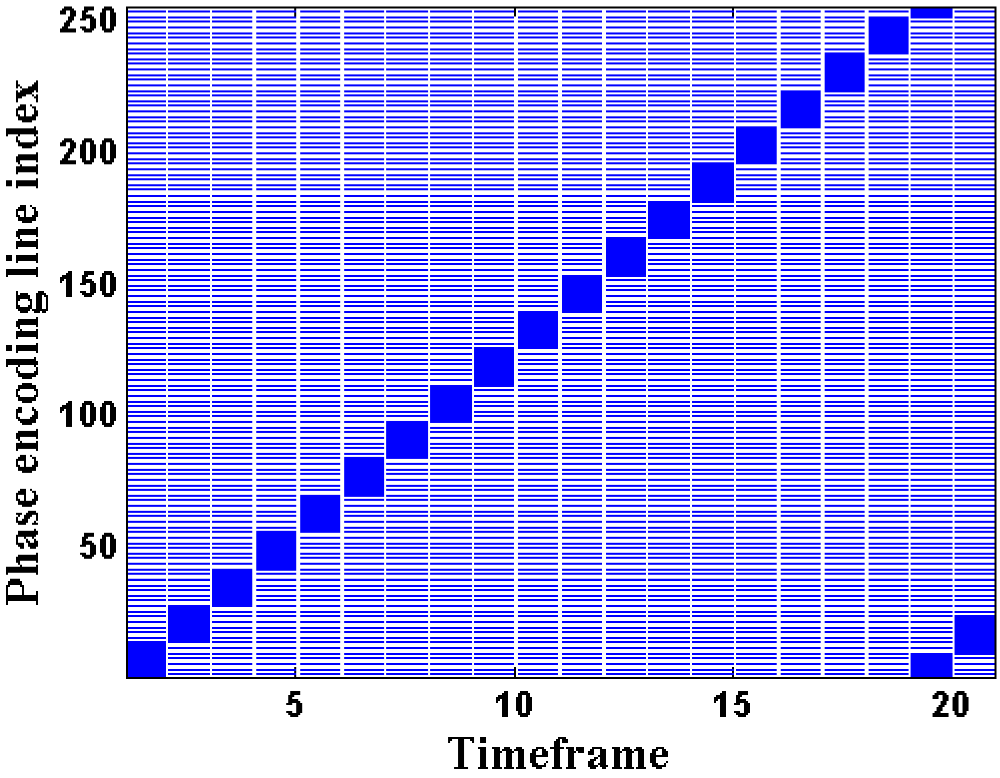

a.

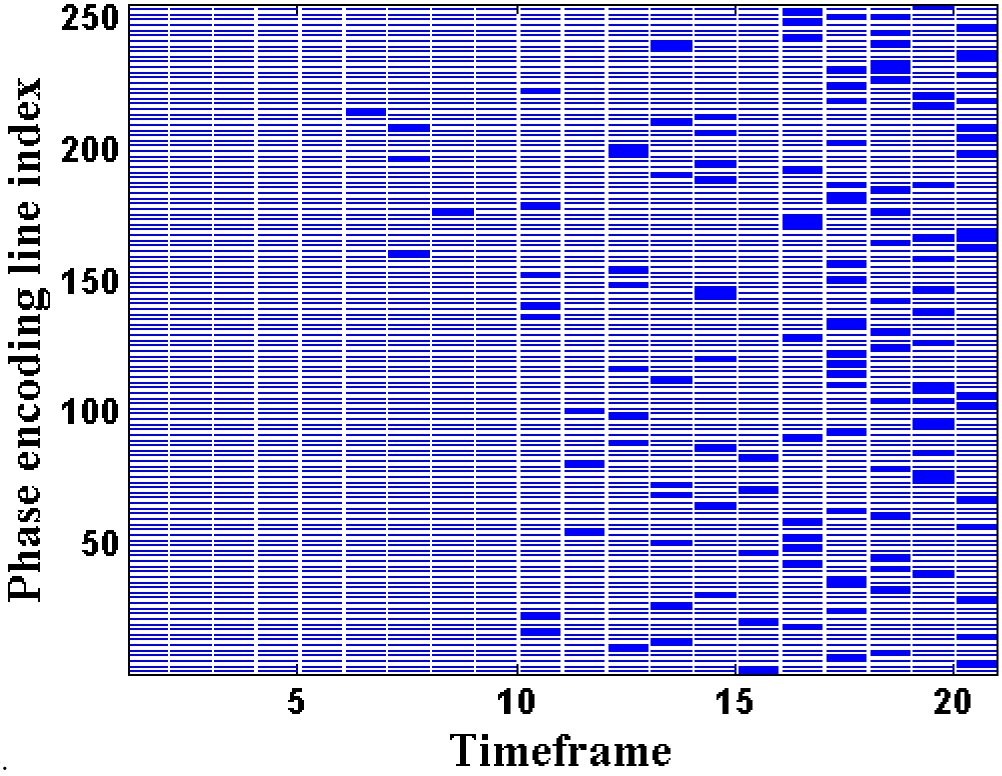

b.

Figure 6.8 The sampling pattern for 1D undersampling in Noquist
(The sampled phase encoding locations are shown in blue line segments at each timeframe: a. heuristic sampling pattern; b.SBS)

Image Sequence Reconstruction

The NRMSE in the dynamic region is plotted at each timeframe for reconstructed images by heuristic sampling pattern and SBS as shown in Figure 6.9. Two sampling patterns performed equally well. Although the NRMSE by the heuristic pattern fluctuates less, the error at this magnitude is negligible.

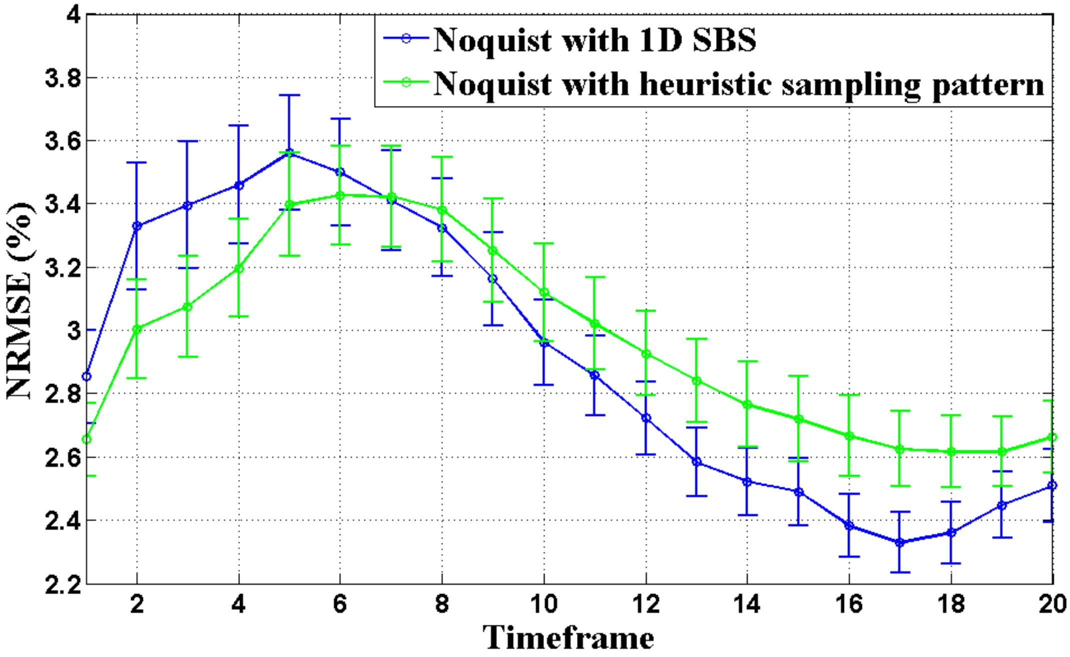

Figure 6.9 Comparison of measured NRMSE between two sampling schemes
(The mean NRMSE with error bars representing the standard deviation is measured in the dynamic region over 40 full-sized image sequences by Noquist with: 1D SBS (blue) and heuristic sampling pattern (green))

The reconstructed images at the 5th timeframes indicate the highest error rates. The corresponding reconstructed images from the two sampling patterns are compared against the original images in Figure 6.10. The difference images are color-coded as the percentage of mean intensity value of the original image. There are barely any residuals inside the dynamic region. The largest errors shown as green to red pixels occur at the immediate surroundings of the dynamic region. This is because the assumed static region is only reconstructed once throughout the image sequence, while small variations or blood flow motion may occur in reality. Overall, both sampling patterns achieve equally good results. From the similarity in the sampling pattern and the associated reconstruction quality, we conclude that the performance of the SBS and the heuristic sampling patterns are essentially the same in this type of data with 50% dynamic FOV ratio.

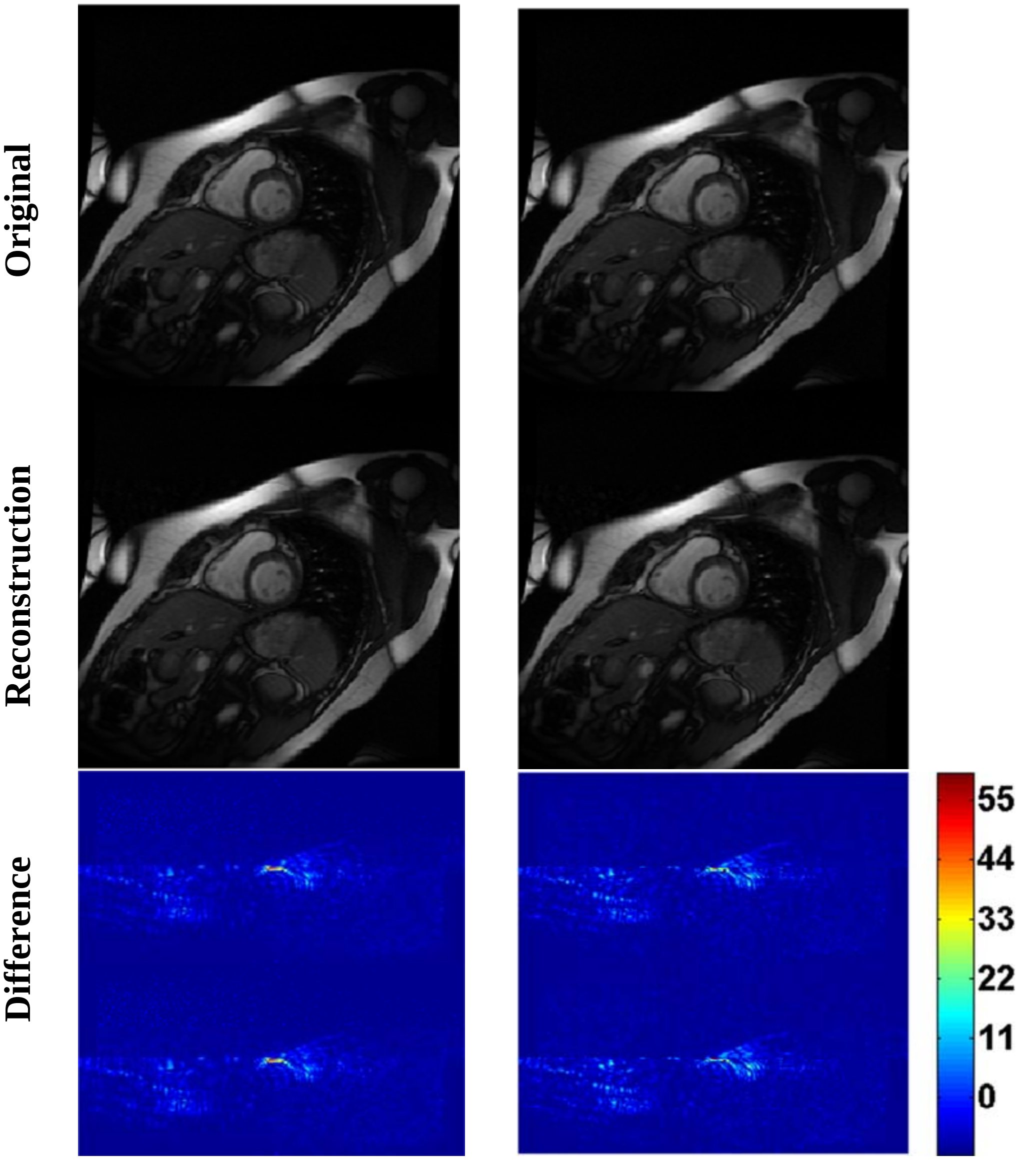

Figure 6.10 Randomly selected reconstructed images by Noquist with heuristic sampling pattern (left column) and Noquist with SBS (right column)

(Images for top to bottom: original image, reconstruction, and difference image is the absolute value of the difference between the original and reconstructed images as a percentage of the mean intensity of the original image)

Discussion

In this experiment, the matrix A_{1D} of size 5120-by-2688 has to be constructed for the SBS single-row elimination. Regardless of the selection schemes, the sample selection can be done prior to the image acquisition.

SBS is more flexible than the heuristic sample selection. It is not necessary to eliminate the same number of rows at each timeframe. That is, more *k*-space lines may be sampled in one timeframe than the others. And SBS applies regardless of the ration between the size of the dynamic region and the FOV.

Noquist claimed that the heuristic sampling pattern could be applied for a variety of image sizes and different dynamic region size with stable results. However, it will be troublesome to apply if the size of the dynamic region, *ND*, is reduced such that the resulted $N_{linesToSample}$ falls below 128. In such cases, not all the even lines can be sampled at a timeframe. For example, in the setup of this experiment, *ND* has to be above 122 by Equation (6.7) to ensure all even lines will be sampled at each timeframe. We can see from Figure 6.11 that *ND* could be further reduced below 122. The principle of sampling a phase encoding in *k-t* space at least once makes the heuristic sampling pattern difficult to implement for the cases that the ratio, *ND/N*, is less than 50%, whereas SBS would not have this issue.

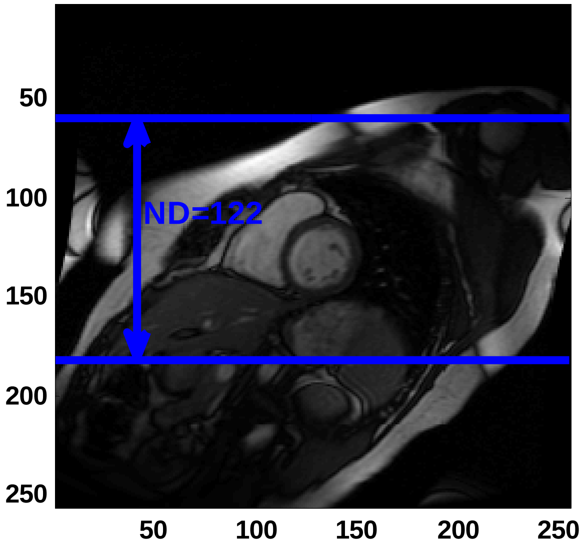

Figure 6.11 The rectangular dynamic region with *ND=122*

6.4.2 Validation on the Proposed Stopping Criterion of SBS Elimination

The purpose of this experiment is to validate the stopping criterion of SBS multi-row elimination on a set of data different from the one used to determine the stopping criterion in Section 6.3.4.

In this experiment, a data set consisting of 40 resized 64-by-64-by-5 cardiac image sequences as described in Section 6.4 was used. Figure 6.12 displays one of such reduced-size image sequence. These 40 image sequences were not used for the training set. All other parameter settings such as the image sequence size, the selected dynamic region, and SBS algorithm etc. were the same as used for the training set in Section 6.3.4. The dynamic region was bounded by the B-spline contour shown in Figure 6.13 with $ND_p = 366$, $NS_p = 3730$, and $N = 64$.

Figure 6.12 Illustration of a 64×64×5 resized cardiac image sequence

Figure 6.13 The dynamic region for a reduced-size cardiac image sequence

Figure 6.14 shows the NRMSE with error bars representing the standard deviation inside the dynamic region. Compared to Figure 6.4, the average NRMSE has similar behavior: it stayed under 10% before 189 rows were eliminated and then dramatically raised above 27%. The NRMSE is slightly higher on average and has larger variation from the 170th to 188th elimination than the training data set. Same as observed for the results on the training set, 180 would be the maximum number of eliminations. We conclude that the proposed stopping criterion of SBS in Section 6.3.4 is reliable to achieve the same level of accuracy on a set of image data not used in the training set.

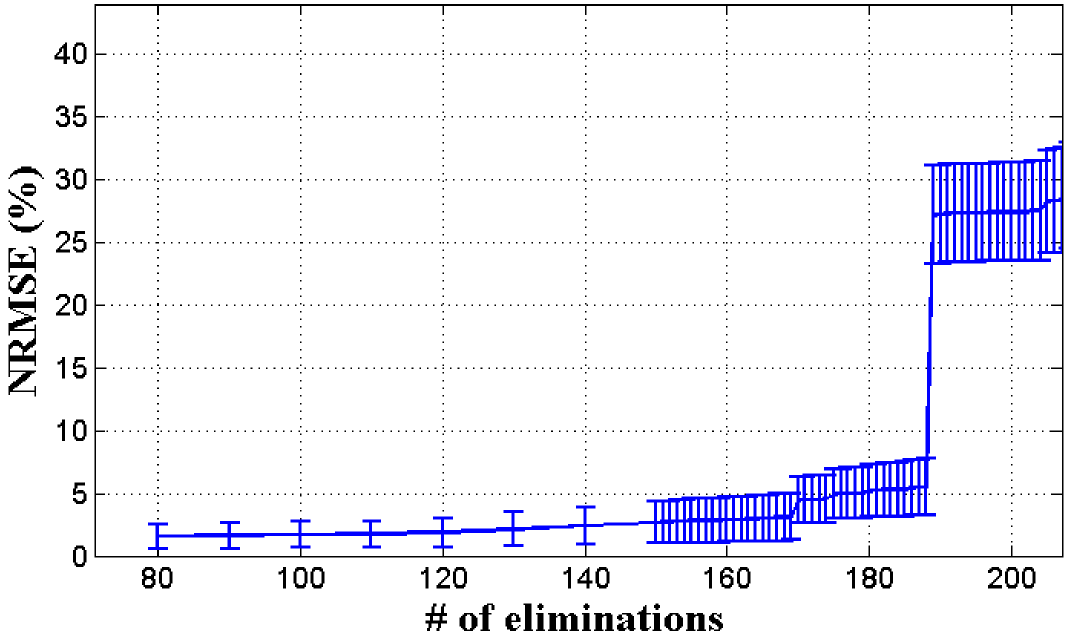

Figure 6.14 NRMSE with error bars vs. the number of SBS eliminations on 40 resized image sequences for validation

(The NRMSE inside the dynamic region is averaged over 40 64×64×5 resized cardiac image sequences with the error bars representing the standard deviation.)

6.4.3 Comparison of NADR and Noquist with SBS

This experiment compared the number of sampled phase encodings between NADR with interleaved sampling and Noquist with SBS while maintaining a comparable NRMSE inside NADR's arbitrarily-shaped dynamic region.

Experimental Setting

For this experiment, the reduced-size dataset described in Section 6.4.2 was used: $N = 64$ and $T = 5$. The corresponding k-space data were simulated as the Fourier transform of the reduced-size magnitude image data. The detailed experimental settings for NADR and Noquist with SBS were as follows.

In NADR, the dynamic region is the same as depicted in Figure 6.15. The interleaved sampling was applied on the simulated k-space data. The sample selection was performed by the SBS with no-matrix-storage implementation. The minimal C_i' values were calculated by minimizing the errors inside the dynamic region only.

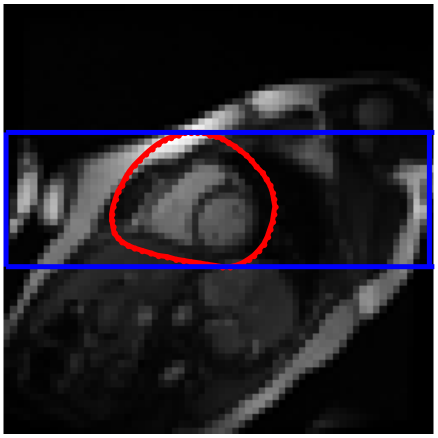

Figure 6.15 The corresponding dynamic region by Noquist
(NADR's arbitrarily shaped dynamic region (red); the rectangular dynamic region across the FOV for Noquist (blue))

In Noquist, the dynamic region for Noquist was defined as the smallest stripe across the FOV which encloses NADR's dynamic region for a fair comparison. Therefore, the number of rows in the dynamic region (*ND*) equals 22, and the number of rows in the static region (*NS*) is 42. Therefore, the number of lines to be sampled per timeframe was $N_{linesToSample} = 22 + 42/5 \approx 31$ by Equation (6.7). A total of 155 lines were sampled from *k-t* space which corresponds to 165 eliminations. The sampling selection was performed by SBS with single-row elimination.

Sampling Patterns

Figure 6.16a plots the sampled line indices at each timeframe by Noquist with SBS. Each of the 155 sampled lines is indicated by a line segment in blue.

For NADR with interleaved sampling, the SBS elimination stopped after 180 eliminations as discussed in Section 6.3.4 which means that 140 lines would be sampled. The sampling pattern shown in Figure 6.16b indicates the sampled *k*-space line indices not reflecting the sampling direction.

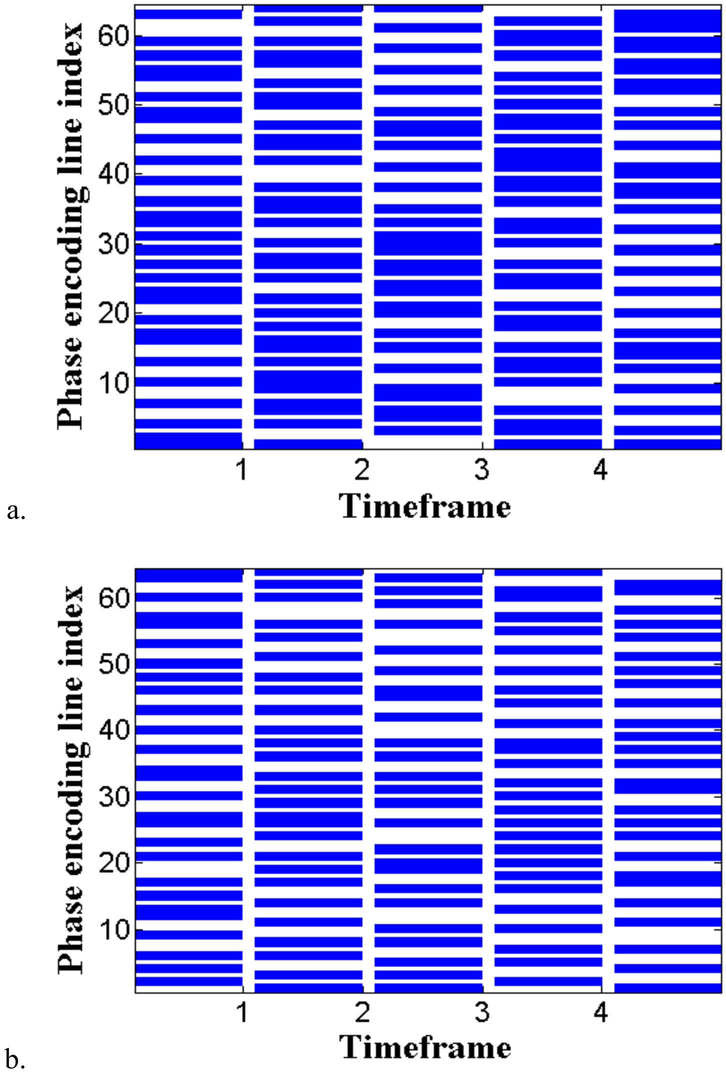

Figure 6.16 Comparison of the sampling patterns between NADR and Noquist with SBS (The sampled line indices are indicated in blue line segments for each timeframe of the 64×64×5 resized cardiac image sequence: a. Noquist with SBS (155 lines); b. NADR (140 lines))

Image Reconstruction

Figure 6.17 shows the mean NRMSE with error bars representing the standard deviation in the proposed dynamic region. The mean and standard deviation of the NRMSE over 40 image sequences were computed. The average NRMSE for Noquist is about 4%; while it is 4.6% on average for NADR. There are no visible differences in the reconstructed image sequences by both NADR and Noquist with SBS compared to the original sequences.

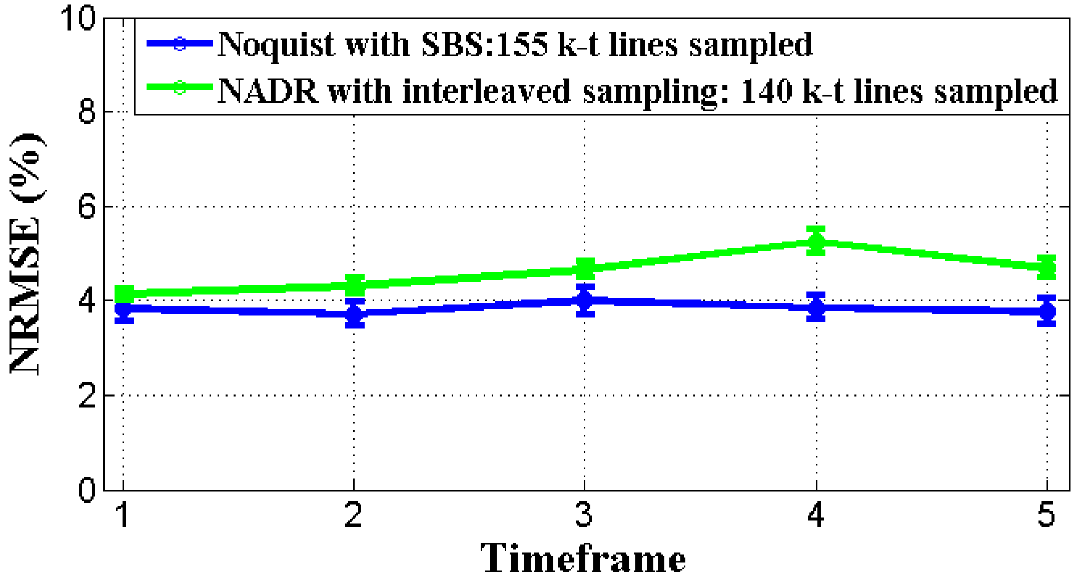

Figure 6.17 Comparison of measured NRMSE with error bars between NADR and Noquist with SBS (The mean NRMSE with error bars representing the standard deviation is measured in the dynamic region over 40 64×64×5 image sequences by: Noquist with SBS (blue) and NADR with interleaved sampling (green))

For illustration purpose, the original, reconstructed, and difference images for NADR and Noquist with SBS are displayed in Figure 6.18 and 6.19. NRMSE for the reconstructed images by NADR and Noquist with SBS are 4.3% and 4.6% respectively. The difference images are color-coded as the percentage of mean intensity value of the original image. Comparing the errors inside the proposed dynamic region, the reconstruction by NADR is favorable because the pixels in the region of interest have relatively even, random noise like errors. Note that both difference images would be completely black if they are displayed together with the reconstructed and original images in grayscale. The colored difference images amplify the residuals between the reconstructed and original images.

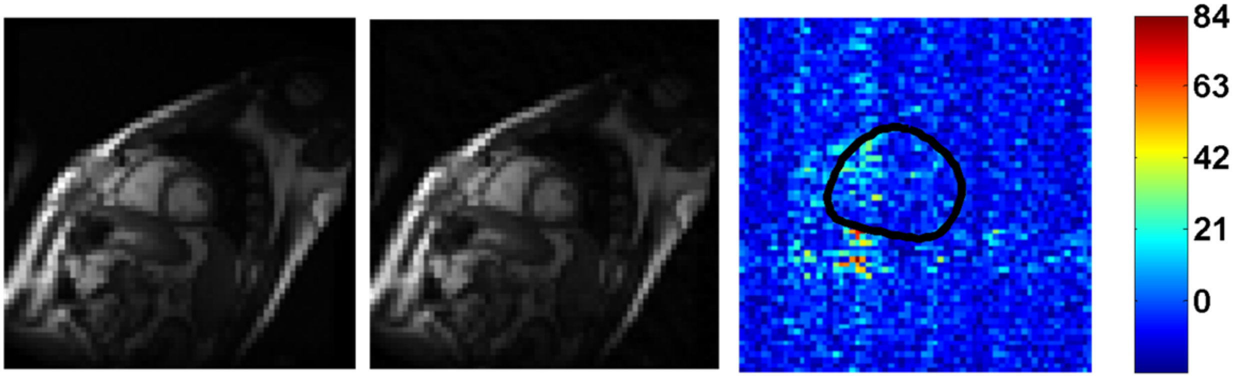

Figure 6.18 Randomly selected reconstructed images by NADR
(Images from left to right: original image, reconstruction, and difference image with colorbar indicating the percetange of the mean intensity of the original image. The black region in the difference image indicates NADR's dynamic region)

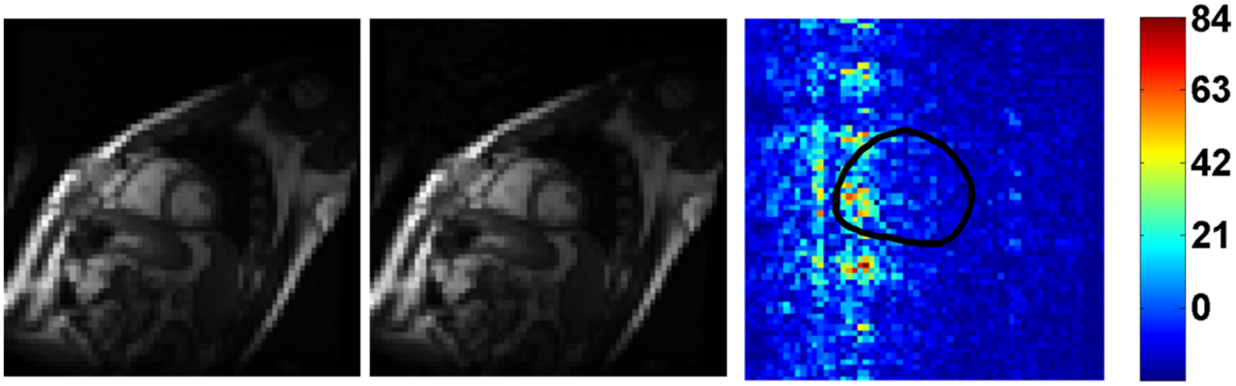

Figure 6.19 Randomly selected reconstructed images by Noquist with SBS
(Images from left to right: original image, reconstruction, and difference image with colorbar indicating the percetange of the mean intensity of the original image. The black region in the difference image indicates NADR's dynamic region)

6.4.4 Comparison of NADR with Interleaved and Non-interleaved Sampling

This experiment compared NADR with interleaved sampling to NADR with non-interleaved sampling. Therefore, all other parameter settings in this experiment stayed the same as the NADR described in Section 6.4.3.

The theoretical limit on the number of *k*-*t* lines to sample is not affected by the sampling direction. As calculated in Section 6.4.2, at least 90 *k*-*t* space lines needed to be sampled. The non-matrix-storage implementation was also applied for NADR with non-interleaved sampling.

In SBS algorithm, the elimination candidates for non-interleaved sampling are different from the candidates for interleaved sampling. Therefore, the stopping criterion for NADR with non-interleaved sampling was evaluated on the training set discussed in Section 6.3.4 in order to determine the maximum number of rows to eliminate. Figure 6.20 shows the NRMSE in the dynamic region vs. the number of eliminations using the training set. The error bars represent the standard deviation of NRMSE. The average NRMSE stayed below 10% until 182 rows has been eliminated and increased beyond 40% after 190 eliminations. We conclude that the elimination for NADR with non-interleaved sampling should stop after 175 eliminations. That is, 320-175 = 145 phase encodings in total should be sampled.

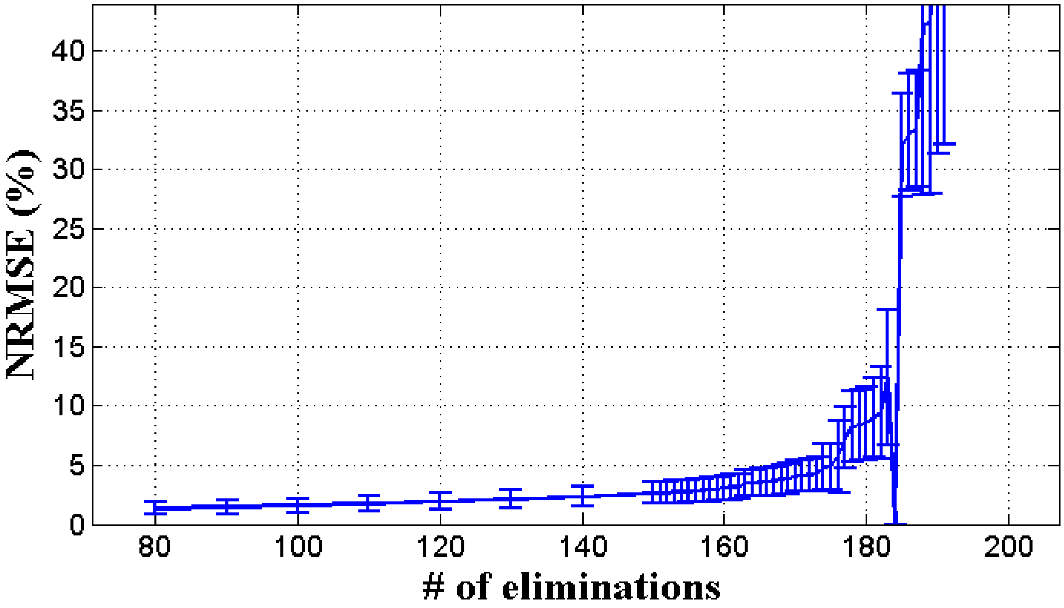

Figure 6.20 Measured NRMSE with error bars vs. the number of SBS eliminations for NADR with non-interleaved sampling
(The NRMSE inside the dynamic region is averaged over 40 64×64×5 resized cardiac image sequences with the error bars representing the standard deviation for NADR with non-interleaved.)

Figure 6.21 compares the NRMSE in the dynamic region at each timeframe for NADR with interleaved sampling against NADR with non-interleaved sampling. For a comparable NRMSE, 140 *k-t* lines were sampled for NADR with interleaved sampling; whereas the non-interleaved sampling direction required 145 lines. Obviously, the interleaved sampling used fewer samples to achieve a comparable NRMSE.

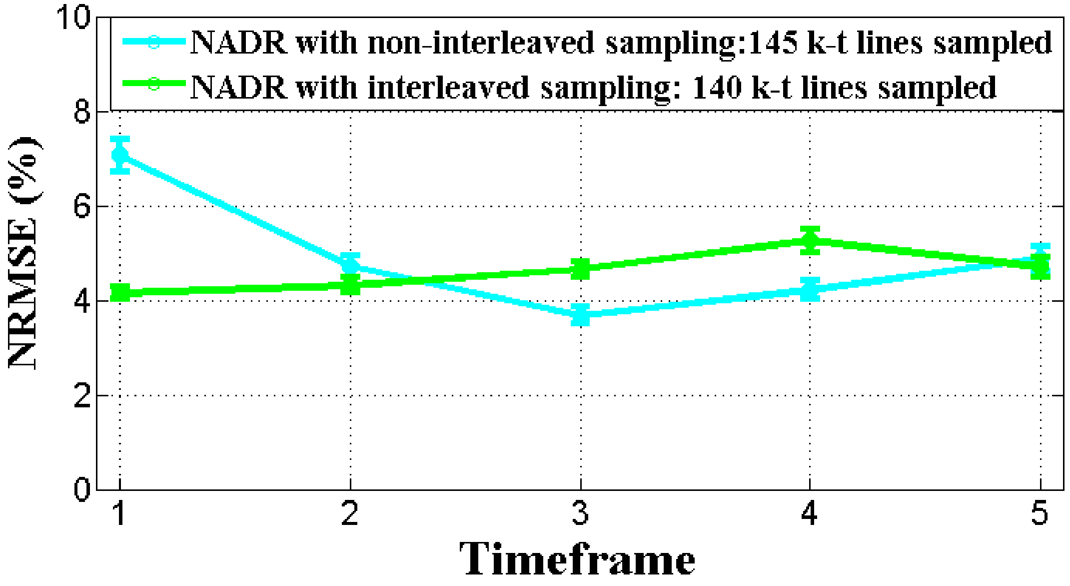

Figure 6.21 Comparison of measured NRMSE with error bars by NADR with interleaved and non-interleaved sampling
(The mean NRMSE with error bars representing the standard deviation is measured in the dynamic region over 40 full-sized image sequences by NADR: with interleaved sampling (green) and non-interleaved sampling (cyan))

6.5 Discussion

Overall, NADR yields stable results with a larger reduction factor in the image acquisition compared to Noquist. The experimental results provide some interesting insights for a further investigation.

The first experiment suggests that SBS performs equally well, if not better, compared to the heuristic sample selection in the case heuristic selection can be easily applied. Noquist [99] has presented the results with the dynamic to FOV ratio, *ND*/*N*, varying from 80% to 20%. It would be interesting to learn the heuristic sampling scheme corresponding to the 20% dynamic FOV ratio and compare its performance against SBS where there would be some artifacts in the reconstructed images.

Compared to the SBS algorithm, the heuristic sampling pattern from Noquist is not only hard to streamline for different dynamic FOV ratios (*ND*/*N*), but it is also inapplicable for the 2D sample selection in NADR. Therefore, SBS is a critical component of NADR.

The specific number of eliminations in the SBS algorithm needs to be verified for every combination of the image sequence size and the dynamic region. Fortunately, the sample selection can be isolated from the scan routine by pre-computing a set of different combinations.

To further investigate the performance of NADR on full-sized cardiac image sequences, the SBS with no-matrix-storage strategy has to be optimized. With the current implementation, the sample selection takes over a month for a 64-by-64-by-20 image sequence using a computer cluster with a total of 64 cores at 2.8GHz, 384GB RAM and 5.1TB raw internal storage.

We would also like to investigate the feasibility of NADR on phase contrast (PC) quantitative flow image sequences. In PC image sequences, the dynamic FOV ratio (ND_p/N^2) would be smaller than in cine MRI image sequences; the full *k*-*t* space measurements would always have to be acquired. Conceptually, a greater reduction in the imaging acquisition time is expected in such an application.

6.6 Conclusion

Our simulation results demonstrate that NADR requires 44% of *k*-*t* space lines, which is 10% less compared to Noquist with SBS, to reconstruct the resized image sequences with no visual differences. Moreover, NADR offers greater flexibility to shape the dynamic region. This makes it more suitable for accelerating the flow imaging.

Chapter 7 Summary and Future Work

A comprehensive assessment of the human heart requires measures of both RV and LV function. Cardiac MRI is routinely used clinically to measure EF in both ventricles, but more parameters are needed to characterize the complex and sometimes subtle changes in cardiac shape and function in disease states. These parameters must be accurate, validated, and practical in a clinical setting. Also, changes in these parameters in response to disease must be explained mechanistically in terms of cardiac anatomy and physiology.

In this dissertation, three issues relevant to the development of new cardiac parameters were studied. First, a new method for propagating RV contours was validated. This technique leverages the RV contours that are routinely drawn clinically to measure RV volumes and EF to produce RV volume-time curves, which better characterize how the RV fills and ejects blood during its cycle. The validation study demonstrated that the new parameters of RV function based on these volume-time curves were accurate. In addition, the propagation is fully automatic, which is important for clinical use of the technique.

The second issue was a mechanistic explanation of why a relative new parameter developed in previous research, circumferential strain, is depressed in hypertensive patients even though the EF is preserved or elevated relative to normal volunteers. A combination of theoretical analysis and experiments was presented that suggests this seemingly paradoxical relationship is largely due to the geometric effects of concentric remodeling.

The final issue was a technique to accelerate the acquisition of cardiac MRI data. Fast cardiac image acquisition is important to all parameters of cardiac shape and function since these parameters are all measured from these images. Fast acquisition could be used to improve the temporal resolution of cardiac cine data, which could increase contour propagation accuracy. Increased temporal resolution and accuracy in the resulting volume-time curves could also reveal subtle changes in cardiac ejection and filling dynamics in response to disease.

The advances in all three of the issues addressed in this dissertation have the potential to expand the clinical use of cardiac MRI and improve the ability of physicians to diagnose and treat patients with cardiac disease.

The key contributions of this dissertation are:

- An experimental validation to the previously proposed dual-propagation method. The validation indicates that the dual-propagation provides a fast, accurate and practical means of measuring RV volume-based indices such as RVEDV, RVESV, RVSV, and RVEF.
- The derivation and validation of an analytic model for predicting LVEF in large groups of patients and a control population. This relatively simple LV modeling method can predict EF with good accuracy over a wide range of heart conditions and allow immediate estimation and analysis of the effects of various physiologic parameters on LVEF.
- A possible explanation to the preserved LVEF with reduced circumferential shortening in hypertension. Our work suggests that this apparent paradox is primarily due to the geometric effects of concentric remodeling, and may imply that this observed reduction in strains does not necessarily represent subclinical contractile dysfunction.
- Modification of the original SBS to enable multi-row elimination at a time and minimize errors in a certain region of the image.
- A new imaging method, NADR, for fast acquisition while preserving the reconstruction quality. NADR offers great flexibility to shape the dynamic region and a further reduction in

image acquisition time compared to the existing technique while maintaining comparable NRMSE.

Other directions for future work include:

- Investigating other types of heart conditions, such as marathon runners and mitral regurgitation etc., with our LV geometric remodeling. Although hypertension is of primary interest for our LV geometric remodeling, the results suggest the accurate prediction for LVEF over various volume and pressure loading conditions.
- Seeking ways to accelerate the SBS non-matrix-storage implementation.
- Testing on the full-sized cardiac image sequences.
- Applying NADR on phase contrast quantitative flow image sequences.

Bibliography

1. Lima, J.A. and M.Y. Desai, *Cardiovascular magnetic resonance imaging: current and emerging applications.* J Am Coll Cardiol, 2004. **44**(6): p. 1164-71.

2. Alfakih, K., et al., *Assessment of ventricular function and mass by cardiac magnetic resonance imaging.* Eur Radiol, 2004. **14**: p. 1813 - 1822.

3. Schalla, S., et al., *Comparison of magnetic resonance real-time imaging of left ventricular function with conventional magnetic resonance imaging and echocardiography.* Am J Cardiol, 2001. **87**(1): p. 95-9.

4. Zha, W., et al., *Assessment of Right Ventricular Function by Cine MRI Based on a Semi-automated Dual Contour Propagation Technique.* J Cardiovasc Magn Reson, In preparation.

5. Zha, W., et al., *Preserved Ejection Fraction in the Presence of Reduced LV Wall Strain in Hypertension: A Geometric Explanation Validated by MRI.* Proc. Intl. Soc. Mag. Reson. Med, 2011.

6. Zha, W., et al., *Geometric Remodeling Effect: Implication of Preserved Ejection Fraction despite Depressed Circumferential Strain in Hypertension.* Circ Cardiovasc Imaging, In preparation.

7. Zha, W., et al., *Accelerated cardiac MRI by 2D Fourier Inversion of the Entire Image Sequence.* Proc. Intl. Soc. Mag. Reson. Med, 2012.

8. Lilly, L.S., *Pathophysiology of heart disease*2003: Lippincott, Williams & Wilkins.

9. Purves, W.K., D. Sadava, and G.H. Orians, *Life: The Science of Biology: Volume III: Plants and Animals*. Vol. 3. 2004: WH Freeman & Co.

10. Walt, G., *WHO's World health report 2003.* BMJ, 2004. **328**(7430): p. 6.

11. McMurray, J.J.V. and M.A. Pfeffer, *Heart failure.* The Lancet, 2005. **365**(9474): p. 1877-1889.

12. Yusuf, S., T. Thom, and R.D. Abbott, *Changes in hypertension treatment and in congestive heart failure mortality in the United States.* Hypertension, 1989. **13**(5 Suppl): p. I74.

13. Levy, D., et al., *The progression from hypertension to congestive heart failure.* JAMA, 1996. **275**(20): p. 1557-62.

14. Volpe, M., R. McKelvie, and H. Drexler, *Hypertension as an underlying factor in heart failure with preserved ejection fraction.* J Clin Hypertens (Greenwich), 2010. **12**(4): p. 277-83.

15. Carretero, O.A. and S. Oparil, *Essential Hypertension : Part I: Definition and Etiology.* Circulation, 2000. **101**(3): p. 329-335.

16. Konstam, M.A., et al., *Left Ventricular Remodeling in Heart Failure: Current Concepts in Clinical Significance and Assessment.* JACC: Cardiovascular Imaging. **4**(1): p. 98-108.

17. Drazner, M.H., *The Progression of Hypertensive Heart Disease.* Circulation, 2011. **123**(3): p. 327.

18. Alfakih, K., et al., *Assessment of ventricular function and mass by cardiac magnetic resonance imaging.* Eur Radiol, 2004. **14**(10): p. 1813-22.

19. Greyson, C.R., *Evaluation of right ventricular function.* Curr Cardiol Rep, 2011. **13**(3): p. 194-202.

20. Prince, J.L. and J.M. Links, *Medical imaging signals and systems*2006: Pearson Prentice Hall.

21. Gaasch, W.H., *Left ventricular radius to wall thickness ratio.* Am J Cardiol, 1979. **43**(6): p. 1189-94.

22. Abraham, T.P. and R.A. Nishimura, *Myocardial strain: can we finally measure contractility?* J Am Coll Cardiol, 2001. **37**(3): p. 731-734.

23. Grothues, F., et al., *Interstudy reproducibility of right ventricular volumes, function, and mass with cardiovascular magnetic resonance.* Am Heart J, 2004. **147**(2): p. 218-23.

24. Crean, A., et al., *3D Echo systematically underestimates right ventricular volumes compared to cardiovascular magnetic resonance in adult congenital heart disease patients with moderate or severe RV dilatation.* J Cardiovasc Magn Reson, 2011. **13**(1): p. 78.

25. Lynch, M., O. Ghita, and P.F. Whelan, *Automatic segmentation of the left ventricle cavity and myocardium in MRI data.* Comput Biol Med, 2006. **36**(4): p. 389-407.

26. Codella, N.C., et al., *Left ventricle: automated segmentation by using myocardial effusion threshold reduction and intravoxel computation at MR imaging.* Radiology, 2008. **248**(3): p. 1004-12.

27. Lee, H.Y., et al., *Automatic left ventricle segmentation using iterative thresholding and an active contour model with adaptation on short-axis cardiac MRI.* IEEE Trans Biomed Eng. **57**(4): p. 905-13.

28. Peters, J., et al., *Accurate segmentation of the left ventricle in computed tomography images for local wall thickness assessment.* Med Image Comput Comput Assist Interv. **13**(Pt 1): p. 400-8.

29. Bradlow, W.M., et al., *Measuring the heart in pulmonary arterial hypertension (PAH): implications for trial study size.* J Magn Reson Imaging, 2010. **31**(1): p. 117-24.

30. Feng, W., et al., *A dual propagation contours technique for semi-automated assessment of systolic and diastolic cardiac function by CMR.* J Cardiovasc Magn Reson, 2009. **11**: p. 30.

31. Falcão, A.X., et al., *User-Steered Image Segmentation Paradigms: Live Wire and Live Lane.* Graphical Models and Image Process, 1998. **60**(4): p. 233-260.

32. Xu, C. and J.L. Prince, *Snakes, shapes, and gradient vector flow.* IEEE Trans Image Process, 1998. **7**(3): p. 359-69.

33. Xu, C. and J.L. Prince, *Generalized gradient vector flow external forces for active contours.* Signal Processing, 1998. **71**(2): p. 131-139.

34. Li, B. and S.T. Acton, *Automatic active model initialization via Poisson inverse gradient.* IEEE Trans Image Process, 2008. **17**(8): p. 1406-20.

35. Melonakos, J., et al., *Finsler active contours.* IEEE Trans Pattern Anal Mach Intell, 2008. **30**(3): p. 412-23.

36. Cootes, T.F., G.J. Edwards, and C.J. Taylor, *Active appearance models.* IEEE Trans Pattern Anal Mach Intell, 2001. **23**(6): p. 681-685.

37. Seghers, D., et al., *Minimal shape and intensity cost path segmentation.* IEEE Trans Med Imaging, 2007. **26**(8): p. 1115-29.

38. Greig, D., B. Porteous, and A. Seheult, *Exact maximum a posteriori estimation for binary images.* JRSS, 1989. **51**(2): p. 271-279.

39. Boykov, Y. and V. Kolmogorov, *An experimental comparison of min-cut/max- flow algorithms for energy minimization in vision.* IEEE Trans Pattern Anal Mach Intell, 2004. **26**(9): p. 1124-1137.

40. Grady, L. and L. Grady, *Random Walks for Image Segmentation.* IEEE Trans Pattern Anal Mach Intell. , 2006. **28**(11): p. 1768-1783.

41. Udupa, J.K. and S. Samarasekera, *Fuzzy Connectedness and Object Definition: Theory, Algorithms, and Applications in Image Segmentation.* Graphical Models and Image Process, 1996. **58**(3): p. 246-261.

42. Falcao, A.X., J.K. Udupa, and F.K. Miyazawa, *An ultra-fast user-steered image segmentation paradigm: live wire on the fly.* IEEE Trans Med Imaging, 2000. **19**(1): p. 55-62.

43. Pluempitiwiriyawej, C., et al., *STACS: new active contour scheme for cardiac MR image segmentation.* IEEE Trans Med Imaging, 2005. **24**(5): p. 593-603.

44. Franz, P., *Bayesian Network Classifiers Versus Selective Formula Not Shown-NN Classifier [J].* Pattern Recognition, 2005. **38**(1): p. 1-10.

45. Wong, M.L., S.Y. Lee, and K.S. Leung, *Data mining of Bayesian networks using cooperative coevolution.* Decision Support Systems, 2004. **38**(3): p. 451-472.

46. Yu, S.X. and J. Shi. *Segmentation with pairwise attraction and repulsion*. 2001.

47. Stein, A. and M. Hebert. *Combining Local Appearance and Motion Cues for Occlusion Boundary Detection*. 2007.

48. van Geuns, R.J., et al., *Automatic quantitative left ventricular analysis of cine MR images by using three-dimensional information for contour detection.* Radiology, 2006. **240**(1): p. 215-21.

49. Strugnell, W.E., et al., *Modified RV short axis series--a new method for cardiac MRI measurement of right ventricular volumes.* J Cardiovasc Magn Reson, 2005. **7**(5): p. 769-74.

50. Schnabel, J., et al. *A generic framework for non-rigid registration based on non-uniform multi-level free-form deformations*. 2010. Springer.

51. Noble, N.M., et al., *Myocardial delineation via registration in a polar coordinate system.* Academic radiology, 2003. **10**(12): p. 1349.

52. Niemann, P.S., et al., *Anatomically oriented right ventricular volume measurements with dynamic three-dimensional echocardiography validated by 3-Tesla magnetic resonance imaging.* J Am Coll Cardiol, 2007. **50**(17): p. 1668-76.

53. Feng, W., *Global and Local Cardiac Functional Analysis with Cine MR Imaging: A Non-Rigid Image Registration Approach.* 2009.

54. Neter, J., et al., *Applied linear statistical models*. 4th ed1996: McGraw-Hill/Irwin.

55. Dell'Italia, L.J., et al., *Right and left ventricular volumes and function after acute pulmonary hypertension in intact dogs.* J Appl Physiol, 1995. **78**(6): p. 2320-7.

56. Young, A.A., et al., *Three-dimensional changes in left and right ventricular geometry in chronic mitral regurgitation.* Am J Physiol, 1996. **271**(6 Pt 2): p. H2689-700.

57. Hacker, M., et al., *Clinical validation of the gated blood pool SPECT QBS processing software in congestive heart failure patients: correlation with MUGA, first-pass RNV and 2D-echocardiography.* Int J Cardiovasc Imaging, 2006. **22**(3-4): p. 407-16.

58. Jenkins, C., et al., *Reproducibility of right ventricular volumes and ejection fraction using real-time three-dimensional echocardiography: comparison with cardiac MRI.* Chest, 2007. **131**(6): p. 1844-51.

59. Shimada, Y.J. and T. Shiota, *A meta-analysis and investigation for the source of bias of left ventricular volumes and function by three-dimensional echocardiography in comparison with magnetic resonance imaging.* Am J Cardiol, 2011. **107**(1): p. 126-38.

60. Maheshwari, M. and S.R. Mittal, *"Simpson's right ventricle ejection fraction versus tricuspid annular plane systolic excursion in patients with isolated left ventricle anterior myocardial infarction".* Indian Heart J, 2010. **62**(4): p. 316-9.

61. Miller, D., et al., *The relation between quantitative right ventricular ejection fraction and indices of tricuspid annular motion and myocardial performance.* J Am Soc Echocardiogr, 2004. **17**(5): p. 443-7.

62. Lee, C.Y., et al., *Right heart function and scleroderma: insights from tricuspid annular plane systolic excursion.* Echocardiography, 2007. **24**(2): p. 118-25.

63. Zhuang, X., et al., *A registration-based propagation framework for automatic whole heart segmentation of cardiac MRI.* IEEE Trans Med Imaging. **29**(9): p. 1612-25.

64. Grosgeorge, D., et al., *Automatic cardiac ventricle segmentation in MR images: a validation study.* Int J Comput Assist Radiol Surg. **6**(5): p. 573-81.

65. Lotjonen, J., et al., *Statistical shape model of atria, ventricles and epicardium from short- and long-axis MR images.* Med Image Anal, 2004. **8**(3): p. 371-86.

66. Lorenzo-Valdes, M., et al., *Segmentation of 4D cardiac MR images using a probabilistic atlas and the EM algorithm.* Med Image Anal, 2004. **8**(3): p. 255-65.

67. Grothues, F. and R. Braun-Dullaeus, *Serial assessment of ventricular morphology and function.* Heart Fail Clin, 2009. **5**(3): p. 301-14, v.

68. Rosamond, W., et al., *Heart disease and stroke statistics--2008 update: a report from the American Heart Association Statistics Committee and Stroke Statistics Subcommittee.* Circulation, 2008. **117**(4): p. e25.

69. Bhatia, R.S., et al., *Outcome of heart failure with preserved ejection fraction in a population-based study.* N Engl J Med, 2006. **355**(3): p. 260-9.

70. Fonarow, G.C., et al., *Characteristics, treatments, and outcomes of patients with preserved systolic function hospitalized for heart failure: a report from the OPTIMIZE-HF Registry.* J Am Coll Cardiol, 2007. **50**(8): p. 768-77.

71. Lam, C.S., et al., *Pulmonary hypertension in heart failure with preserved ejection fraction: a community-based study.* J Am Coll Cardiol, 2009. **53**(13): p. 1119-26.

72. Mizuguchi, Y., et al., *Concentric left ventricular hypertrophy brings deterioration of systolic longitudinal, circumferential, and radial myocardial deformation in hypertensive patients with preserved left ventricular pump function.* J Cardiol. **55**(1): p. 23-33.

73. Paulus, W.J., et al., *How to diagnose diastolic heart failure: a consensus statement on the diagnosis of heart failure with normal left ventricular ejection fraction by the Heart Failure and Echocardiography Associations of the European Society of Cardiology.* Eur Heart J, 2007. **28**(20): p. 2539-50.

74. Desai, A. and J.C. Fang, *Heart failure with preserved ejection fraction: hypertension, diabetes, obesity/sleep apnea, and hypertrophic and infiltrative cardiomyopathy.* Heart Fail Clin, 2008. **4**(1): p. 87-97.

75. MacIver, D.H., *Current controversies in heart failure with a preserved ejection fraction.* Future Cardiol, 2010. **6**(1): p. 97-111.

76. Maciver, D.H., *Heart failure with normal left ventricular ejection fraction may be due to systolic dysfunction.* J Am Coll Cardiol, 2009. **54**(5): p. 488; author reply 488-9.

77. Sadler, D.B., et al., *Systolic Function in Hypertensive Men With Concentric Remodeling.* Hypertension, 1997. **30**(4): p. 777-781.

78. Rosen, B.D., et al., *Left Ventricular Concentric Remodeling Is Associated With Decreased Global and Regional Systolic Function: The Multi-Ethnic Study of Atherosclerosis.* Circulation, 2005. **112**(7): p. 984-991.

79. Shimizu, G., et al., *Left ventricular midwall mechanics in systemic arterial hypertension. Myocardial function is depressed in pressure-overload hypertrophy.* Circulation, 1991. **83**(5): p. 1676-84.

80. Cerqueira, M.D., et al., *Standardized Myocardial Segmentation and Nomenclature for Tomographic Imaging of the Heart: A Statement for Healthcare Professionals From the Cardiac Imaging Committee of the Council on Clinical Cardiology of the American Heart Association.* Circulation, 2002. **105**(4): p. 539-542.

81. Deng, X. and T.S. Denney, Jr., *Combined tag tracking and strain reconstruction from tagged cardiac MR images without user-defined myocardial contours.* J Magn Reson Imaging, 2005. **21**(1): p. 12-22.

82. Li, J. and T.S. Denney, Jr., *Left ventricular motion reconstruction with a prolate spheroidal B-spline model.* Phys Med Biol, 2006. **51**(3): p. 517-37.

83. Bower, A.F., *Applied mechanics of solids*2009: CRC Press.

84. Spencer, A.J.M., *Continuum mechanics*2004: Dover Pubns.

85. Aurigemma, G.P., et al., *Geometric changes allow normal ejection fraction despite depressed myocardial shortening in hypertensive left ventricular hypertrophy.* J Am Coll Cardiol, 1995. **26**(1): p. 195-202.

86. Arts, T., R.S. Reneman, and P.C. Veenstra, *A model of the mechanics of the left ventricle.* Ann Biomed Eng, 1979. **7**(3-4): p. 299-318.

87. Van Der Toorn, A., et al., *Transmural gradients of cardiac myofiber shortening in aortic valve stenosis patients using MRI tagging.* Am J Physiol Heart Circ Physiol, 2002. **283**(4): p. H1609-15.

88. Arts, T., P.C. Veenstra, and R.S. Reneman, *Epicardial deformation and left ventricular wall mechanisms during ejection in the dog.* Am J Physiol, 1982. **243**(3): p. H379-90.

89. Lumens, J., et al., *Impaired subendocardial contractile myofiber function in asymptomatic aged humans, as detected using MRI.* Am J Physiol Heart Circ Physiol, 2006. **291**(4): p. H1573-9.

90. Sengupta, P.P., et al., *Left ventricular structure and function: basic science for cardiac imaging.* J Am Coll Cardiol, 2006. **48**(10): p. 1988-2001.

91. Stanton, T. and T.H. Marwick, *Assessment of subendocardial structure and function.* JACC Cardiovasc Imaging. **3**(8): p. 867-75.

92. Hittinger, L., et al., *Hemodynamic mechanisms responsible for reduced subendocardial coronary reserve in dogs with severe left ventricular hypertrophy.* Circulation, 1995. **92**(4): p. 978-86.

93. Stuber, M., et al., *Alterations in the local myocardial motion pattern in patients suffering from pressure overload due to aortic stenosis.* Circulation, 1999. **100**(4): p. 361-8.

94. Van Vaals, J.J., et al., *"Keyhole" method for accelerating imaging of contrast agent uptake.* Journal of Magnetic Resonance Imaging, 1993. **3**(4): p. 671-675.

95. Chandra, S., et al., *Application of reduced-encoding imaging with generalized-series reconstruction (RIGR) in dynamic MR imaging.* J Magn Reson Imaging, 1996. **6**(5): p. 783-97.

96. Jung, H., et al., *k-t FOCUSS: a general compressed sensing framework for high resolution dynamic MRI.* Magn Reson Med, 2009. **61**(1): p. 103-16.

97. Tsao, J., et al., *Optimizing spatiotemporal sampling for k-t BLAST and k-t SENSE: application to high-resolution real-time cardiac steady-state free precession.* Magn Reson Med, 2005. **53**(6): p. 1372-82.

98. Madore, B., G.H. Glover, and N.J. Pelc, *Unaliasing by fourier-encoding the overlaps using the temporal dimension (UNFOLD), applied to cardiac imaging and fMRI.* Magn Reson Med, 1999. **42**(5): p. 813-28.

99. Brummer, M.E., et al., *Noquist: reduced field-of-view imaging by direct Fourier inversion.* Magn Reson Med, 2004. **51**(2): p. 331-42.

100. Pruessmann, K.P., et al., *SENSE: sensitivity encoding for fast MRI.* Magn Reson Med, 1999. **42**(5): p. 952-62.

101. Sodickson, D.K. and W.J. Manning, *Simultaneous acquisition of spatial harmonics (SMASH): fast imaging with radiofrequency coil arrays.* Magn Reson Med, 1997. **38**(4): p. 591-603.

102. Griswold, M.A., et al., *Generalized autocalibrating partially parallel acquisitions (GRAPPA).* Magn Reson Med, 2002. **47**(6): p. 1202-10.

103. Lustig, M., et al., *Compressed Sensing MRI.* Signal Processing Magazine, IEEE, 2008. **25**(2): p. 72-82.

104. Hamilton, L.H., et al., *"PINOT": time-resolved parallel magnetic resonance imaging with a reduced dynamic field of view.* Magn Reson Med, 2011. **65**(4): p. 1062-74.

105. Reeves, S.J. and Z. Zhe, *Sequential algorithms for observation selection.* IEEE Trans Signal Process, 1999. **47**(1): p. 123-132.

106. Golub, G.H. and C.F. Van Loan, *Matrix computations*. Third ed. Vol. 3. 1996: Johns Hopkins Univ Pr.